Diffuse Radio Emission in Merging Galaxy Clusters

Dissertation

zur Erlangung des Doktorgrades
an der Fakultät für Mathematik, Informatik und Naturwissenschaften
Fachereich Physik
der Universität Hamburg

vorgelegt von

Amanda Gloria Wilber

Hamburg, Wintersemester 2018/19

Gutachter/innen der Dissertation:	Prof. Dr. Marcus Brüggen Prof. Dr. Annalisa Bonafede
Zusammensetzung der Prüfungskommission:	Prof. Dr. Marcus Brüggen Prof. Dr. Annalisa Bonafede Prof. Dr. Jochen Liske Dr. Timothy Shimwell Prof. Dr. Günter Sigl
Vorsitzende/r der Prüfungskommission:	Prof. Dr. Jochen Liske
Datum der Disputtation:	18.12.2018
Vorsitzender Fach-Promotionsausschusses PHYSIK:	Prof. Dr. Wolfgang Hansen
Leiter des Fachbereichs PHYSIK:	Prof. Dr. Michael Potthoff
Dekan der Fakultät MIN:	Prof. Dr. Heinrich Graener

Zusammenfassung

Galaxienhaufen sind große Ansammlungen von Galaxien, zwischen denen sehr heißes Gas liegt. Das Intracluster-Medium (ICM), das den Raum zwischen den einzelnen Clustergalaxien füllt, ist ein heißes, verdünntes Plasma, das von komplexen μG-Magnetfeldern und einer Population von kosmischen Strahlungsteilchen durchzogen ist. Galaxiengruppen und Galaxienhaufen verschmelzen zu massiveren Clustern und Superclustern und bilden so die großräumige Struktur des Universums. Eine Verschmelzung von zwei Galaxienhaufen erfolgt über die Zeitskala von etwa 1 Gyr, und während dieser Zeit erzeugen die magnetohydrodynamischen Stöße des Intracluster-Mediums Turbulenz und Stoßwellen, die sich in dem gravitationsgebundenen System ausbreiten. Turbulenz und Stoßwellen agieren als Treiber für die Teilchenbeschleunigung im ICM. Die Beschleunigung der Elektronen der kosmischen Strahlung innerhalb des ICM-Magnetfelds erzeugt großflächige Quellen von Synchrotronstrahlung im Radiobereich. Der Ursprung dieser Radioquellen, die als Radiohalos und Radiorelikte bezeichnet werden, ist noch nicht geklärt.

Um ihre Herkunft zu verstehen, habe ich die Radioeigenschaften von Halos und Relikten in kollidierenden Galaxienhaufen untersucht. Ich habe die die Beobachtungsdaten des Two Metre Sky Survey mit dem LOw Frequency ARray (LOFAR) reduziert und kalibriert, um Bilder verschiedener diffuser Radioquellen in der Clusterumgebung in wissenschaftlicher Qualität zu erstellen. Ich habe die LOFAR Daten mit Daten bei anderen Frequenzen kombiniert, um Spektralanalysen durchzuführen und Szenarien für die Teilchenbeschleunigung zu bestimmen. In den letzten drei Jahren habe ich meine Ergebnisse in drei Erstautor-Artikeln in referierten Zeitschriften veröffentlicht. In diesen Artikeln beschreibe ich mehrere Entdeckungen: zwei neue Radio-Halos, eine nie zuvor gesehene, ausgedehnte Quelle in zwei riesigen Head-tail Galaxien, Radioemission im Zentrum eines massearmen Clusters und eine Nicht-Detektion einer bekannten Stoßwelle in einem massiven Galaxienhaufen. Im Rahmen meiner Forschung habe ich mich darauf konzentriert, durch Beobachtungen aktuelle Modelle zur Teilchenbeschleunigung zu überprüfen.

Das turbulente Wiederbeschleunigungsmodell sagt voraus, dass ultrasteile Radiohalos (ultra-steep spectrum halos - USSRHs) vermehrt in kollidierenden Systemen auftreten sollte. Wir

entdeckten eine solche USSRH im kollidierenden Cluster Abell 1132. Umgekehrt stellt unsere Nichterfassung von Radioquellen im Bereich einer bestätigten Stoßwelle in einem massiven, sich verschmelzenden Cluster die führende Theorie für die Bildung von Relikten in Frage. Wir haben auch Fälle gefunden, in denen Turbulenz aus dem kollidierenden ICM das Plasma in Radiogalaxien wieder beschleunigt. Die Entdeckung der ausgedehnten diffusen Emission, die mit diesen Radiogalaxien verbunden ist, stützt auch die Theorie, dass radiolaute, aktive Galaxienkerne dem ICM eine große Menge an Keimelektronen zuführen können. Schließlich habe ich auch untersucht, wie die Radio-Eigenschaften von Halos und Relikten direkt mit den Entwicklungsphasen einer Kollision verknüpft werden können.

Summary

Galaxy clusters are large assemblies of galaxies and an intervening hot gas which displays abundant physical processes and astrophysical sources of radiation. The intracluster medium (ICM), which makes up the space in between individual cluster galaxies, is a hot, dilute plasma that is laced with complex μG magnetic fields and a population of cosmic ray particles. As the large-scale structure of the Universe dictates, groups and clusters of galaxies merge to form more massive clusters and superclusters. A cluster-cluster merger occurs over the time scale of about 1 Gyr, and during this time the magnetohydrodynamical collisions of the intracluster media produce turbulence and shocks that propagate throughout the gravitationally bound system. Merger-induced turbulence and shocks act as drivers for particle acceleration in the ICM. The acceleration of cosmic ray electrons within the ICM magnetic field produces cluster-sized structures of synchrotron radio emission. The origins of these radio structures, called radio halos and radio relics, is still being investigated.

In order to understand their origins, I have searched for and studied the radio properties of halos and relics in merging galaxy clusters. I reduced and calibrated observational data from the LOw Frequency ARray (LOFAR) Two-meter Sky Survey to make science-quality images of several diffuse radio radio sources in the cluster environment. I combined these LOFAR images with images at other frequencies to carry out spectral analyses and determine scenarios for particle acceleration. In the last three years, I have gathered and published my findings in three first-author refereed journal articles. In these papers, we announced several discoveries: two new radio halos, never-before-seen extended emission in two giant head-tail radio galaxies, remnant radio emission at the center of a low-mass cluster, and a radio non-detection in the region of a known shock in a massive cluster. As part of my research, I have focused on how observational evidence either supports or challenges current models on particle acceleration.

The turbulent re-acceleration model predicts that ultra-steep spectrum radio halos (USSRHs) should be more common in merging systems; we discovered such a USSRH in the merging cluster Abell 1132. Conversely, our radio non-detection in the region of a confirmed shock in a massive, merging cluster challenges the leading theory for the formation of radio relics. We have also found cases where merger-driven mechanisms appear to be disturbing, re-accelerating, and re-energizing the emission of bent-tail radio galaxies. The discovery of extended diffuse emission associated with these radio galaxies also supports the theory that radio-loud active galactic nuclei and radio galaxy remnants can provide a large quantity of seed electrons to the ICM. Finally, I have also studied how the radio properties of halos and relics can be directly connected to the evolutionary phases of mergers.

Eidesstattliche Versicherung

Hiermit versichere ich an Eides statt, die vorliegende Dissertationsschrift selbst verfasst und keine anderen als die angegebenen Hilfsmittel und Quellen benutzt zu haben.

Die eingereichte schriftliche Fassung entspricht der auf dem elektronischen Speichermedium.

Die Dissertation wurde in der vorgelegten oder einer ähnlichen Form nicht schon einmal in einem früheren Promotionsverfahren angenommen oder als ungenügend beurteilt.

Amanda Gloria Wilber
Hamburg, den 07.11.2018

Contents

1 Introduction

In the last four centuries, we have greatly enhanced our ability to observe the Universe around us. As early as 1610, Galileo pointed a novel device, a simple small refracting telescope, at the heavens to reveal craters on the moon, the "ears of Saturn," and the orbiting moons of Jupiter. Ever-increasing improvements to the optical telescope have resulted in increased angular resolution and light gathering power. However, in the 1800s, scientists including Herschel, Faraday, and Röntgen discovered that there were other kinds of radiation beyond optical light, and that light itself was linked to electromagnetism. Only in the last century have we begun to engineer instruments able to detect astronomical sources emitting photons from the lower and higher ends of the electromagnetic spectrum. Telescopes have also been launched into orbit to surpass the limitations imposed by Earth's atmosphere, and are used to detect higher-energy radiation which does not reach the Earth's surface. In 1995 the Hubble Space Telescope observed a single, tiny, dark patch in Ursa Major, one 24-millionth of the whole sky, to reveal thousands of distant galaxies, an image known as the Hubble Deep Field. Since then, space telescopes, like the Chandra X-ray observatory and the Spitzer infrared satellite, have been used to investigate all kinds of Galactic and extragalactic sources of electromagnetic radiation.

Looking at objects in the Universe using these different types of telescopes reveals the physical processes of unfathomable environments, which are sometimes optically invisible. Supermassive black holes at the centers of galaxies accrete material and release energy through bipolar jets of hot relativistic plasma that glow in radio and X-rays. Supernovae burst so violently that they can accelerate particles close to the speed of light while spreading heavy nuclei over the interstellar medium. Probing the optically opaque dust of our Milky Way with infrared telescopes reveals the hidden depths of nebulae where stars and planets are being formed. All of the information we glean from the light of our Universe is invaluable to scientists who wish to investigate the origins of our cosmic habitat. Not only is extending our observing window beyond the optical regime advantageous on its own, but combining the observational results from several wavelengths is the best way to investigate the complex processes of astrophysical phenomena.

In the microwave regime, there is a detectable signal emanating from all directions in the sky. This radiation exists as a remnant of the very early Universe as it transitioned from opaque to transparent. The Cosmic Microwave Background (CMB) is one of the strongest pieces of evidence for the Big Bang. In the early 90s the Cosmic Background Explorer (COBE) mapped the first picture of the infant Universe, showing an incredibly homogeneous and isotropic matter distribution with very small variations in temperature. These variations point to tiny fluctuations in density and set the stage for how the large-scale structure of the Universe has developed in the last 14 billion years. Our Universe, as it exists today, is a network of dense string-like filaments separated by vast voids, sometimes referred to as the cosmic web. The filamentary regions of the cosmic web contain all the matter of the Universe, nonbaryonic and baryonic alike.

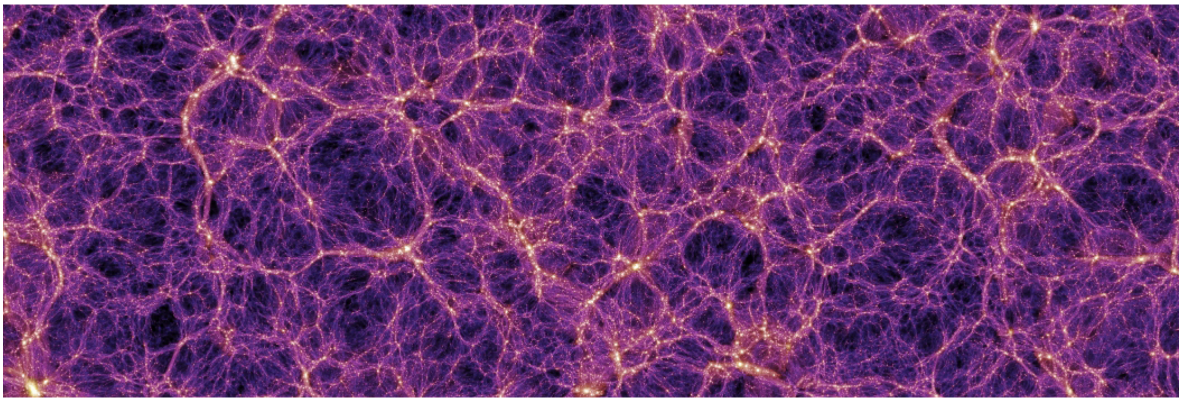

Figure 1.1: The cosmic web. "The Dark Matter distribution of the Universe on extremely large-scales. At the intersection of the filaments are the largest luminous structures in the Universe: galaxy clusters." Millennium Simulation from Springel et al. (2006).

The bulk of the mass in the Universe comes from nonbaryonic Dark Matter ($\sim$80%), which binds together luminous baryonic matter - diffuse gas ($\sim$15%) and galaxies ($\sim$5%) - into galactic groups, clusters of galaxies, and superclusters. These dense and luminous filaments represent an accumulation of gravitationally attracted matter where galactic groups and clusters of galaxies have merged over time. Galaxy clusters can be used as cosmological laboratories since they exist as the largest virialized (i.e. stable) systems and are the smallest structures to contain a full sample representation of the different types of matter found in our Universe (Sarazin, 1988). The mass function of galaxy clusters is a very sensitive probe for determining fundamental cosmological parameters, such as the fraction of matter and Dark Matter in the Universe, Ω_m, and the amplitude of initial density fluctuations, σ_8[1] (Vikhlinin et al., 2005). Clusters are also important targets of study to unlock the riddle of Dark Energy. The eROSITA X-ray telescope, scheduled to launch in April 2019, will be able to detect about

---

[1] This is a function that gives the fluctuations of mass, or effective variance of density, within a sphere of 8 Mpc (e.g. Rich, 2014).

100,000 clusters, allowing us to compile cluster mass functions that, in turn, will constrain the equation of state of Dark Energy.

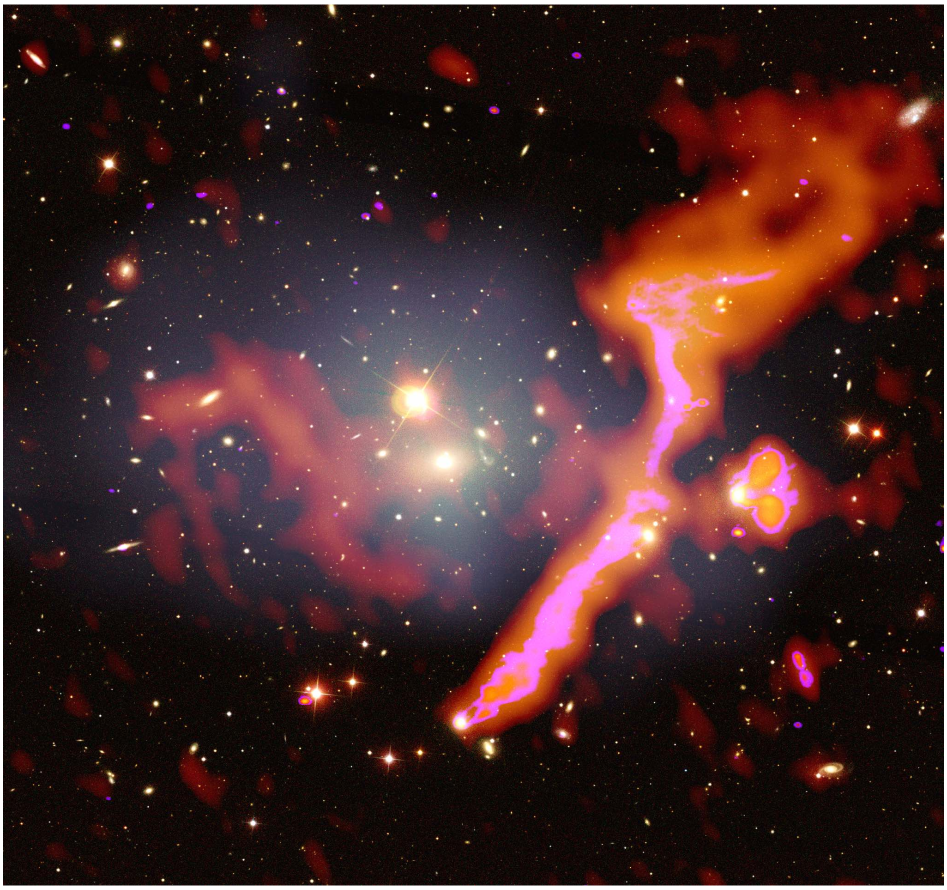

Figure 1.2: A composite image of the galaxy cluster Abell 1314. The gray haze represents the hot X-ray gas of the cluster. Pink and red emission show large-scale radio structures in the cluster. A preview of the results to follow in this thesis, from Wilber et al. (2019).

Radio observations of galaxy clusters have revealed Megaparsec-scale (Mpc) synchrotron emission hosted within the intracluster medium (ICM; e.g. Willson, 1970; Bridle & Fomalont, 1976; Harris & Miley, 1978). The presence of this diffuse radio emission indicates that there are ultra-relativistic[2] electrons and magnetic fields throughout the ICM; however, a mystery remains in identifying the seed source of these electrons and understanding the energetic processes necessary to produce radio structures with such vast sizes. Some clusters host a spherical halo of radio emission emanating from the central region, while other clusters show giant arc-shaped relics on their outer edges. Although characteristically distinct, both of these types of diffuse emission are found in actively merging galaxy cluster systems. About 30% of massive clusters host these diffuse sources (e.g. Giovannini et al., 1999a; Cuciti et al.,

---

[2] Ultra-relativistic particles are particles that have almost all their energy stored in the form of momentum, such that $pc \gg mc^2$.

2015), and occasionally these two emission types, *halos* and *relics*, are found together in the same cluster. Radio halos and radio relics are thought to exist as a result of the violent and turbulent collision of the ICM during a merging process. Understanding the origins of halos and relics, as well as the distinctions between them, may help us to decipher the physics of particle acceleration and identify the origin of cosmic magnetic fields. Observational studies of galaxy clusters and merging systems offer an opportunity to investigate and discern the physics at work within the ICM and how the large-scale structure of the Universe has evolved.

In this thesis radio observations are used to study the dynamics of merging clusters. The following sections in this chapter describe sources of radio emission, the physics of galaxy clusters, and the basics of radio astronomy. A layout of the motivation of this thesis – addressing some of the challenging questions still open in this field – and a summary of the following chapters are given in Sec. 1.5.

1.1 The Radio Sky

While working for Bell Laboratories in 1931, Karl G. Jansky was the first to discover an astronomical radio source: the constant static “hiss” that was received by his radio detector turned out to be the center of the Milky Way (Jansky, 1933). Radio astronomy flourished in the subsequent decades as advancements were made in electronics and computers, especially in digitizing radio antennas. Today, a collection of radio telescopes all over the world observe over a range of 10 MHz - 100 GHz, opening a new window on our Universe.

The Green Bank radio telescope is a single dish telescope that acts as a radio eye with a diameter of 100 meters. The Rayleigh Criterion states that angular resolution goes as the observing wavelength, λ, divided by the diameter, D, of the light-collecting area: $\theta_R \sim \frac{\lambda}{D}$. When observing at a frequency of 4 GHz, the Green Bank telescope can resolve radio sources on an angular scale of $\sim$ 2.5 arcminutes. In Fig. 1.3 the sky as it appears to the Green Bank radio dish is superimposed on an optical photograph of the National Radio Astronomy Observatory (NRAO) in Green Bank, West Virginia. Instead of just pinpoint starlight, we see oddly-shaped structures, some of which are very large and bright, residing out of the plane of the Galactic disk. When looking at the night sky in this unfamiliar light, one is compelled to question the nature of these large radio structures. Are they other galaxies, or are they objects in our Galaxy? What kinds of astrophysical phenomena are producing this radio emission? In the following subsection, the different types of radio sources and the complexities of their origins are addressed.

Figure 1.3: How the sky looks in radio light. Image courtesy of NRAO/AUI.

1.1.1 Types of Radio Sources

Radio astronomy explores astronomical sources that produce radio emission, either continuum emission or line emission. Continuum emission has an intensity that varies over a range of frequencies and can be thermal or non-thermal. Thermal radio sources emit radio waves as part of their black-body radiation which follows a Planck distribution, but given that radio energies are the lowest a photon can have, detectable thermal radio emission only comes from the coldest objects with $T \leq 10$ K. Examples of thermal radio sources are the surface of the Moon and the HII region of the Orion nebula. Radio line emission comes from quantum mechanical transitions such as the 21 cm Hydrogen line produced by a spin-flip transition of the hydrogen atom. This line emission is observed in neutral hydrogen clouds in the Milky Way and is important for studying the Epoch of Reionization (see e.g. Madau et al., 1997;

Zaroubi et al., 2012).

In the context of this thesis, I will focus on the observations and astrophysics of non-thermal synchrotron emission which involves high-energy electrons (or cosmic-ray electrons) accelerated by magnetic fields (see Sec. A.1.2). Synchrotron emission exhibits a power-law distribution such that the brightness, S, is proportional to the frequency, ν, raised to a spectral index, α: $S \propto \nu^{\alpha}$. Because electrons at higher energies lose energy faster by emitting photons at higher frequencies, the spectral index, α, is related to the energy distribution of the electrons. A *steep* spectral index ($\alpha < -1$) indicates a larger population of lower-energy cosmic-ray electrons and a smaller population of high-energy cosmic-ray electrons. Therefore, spectral studies[3] of non-thermal radio sources provide information on the age of the emission. Non-thermal radio astronomy is very important for studying mechanisms and timescales for particle acceleration and the properties of intergalactic and extragalactic magnetic fields. Astronomical sources of non-thermal radio continuum emission can be found all over the Universe, from our local Solar System all the way to the edge of the observable Universe where the first active galaxies exist.

1.1.1.1 Galactic Radio Sources

In our Solar System, the Sun and Jupiter are sources of non-thermal radio emission because they have strong magnetic fields which capture and accelerate cosmic-ray electrons. Some of the brightest non-thermal radio sources in the sky are from supernovae remnants (SNRs) in the Milky Way. Cassiopeia A is the brightest SNR, but there are 94 other radio-emitting SNRs detected in the Milky Way so far, including the Crab nebula, the Tycho and Kepler remnants, and a nebula filament in the direction of Cygnus (Dubner & Giacani, 2015).

Recently, an image of the Galactic center was produced using the MeerKAT radio array (see Fig. 1.4), which is the precursor to the Square Kilometer Array (SKA) in South Africa. The Milky Way appears to host a complex bulge of radio emission at the center (referred to as Sagittarius A), most likely attributed to star formation. Puffs of emission from SNRs can be seen further from the center. Perhaps the most striking features of this image are the thin and bright filaments of emission which extend perpendicular to the Galactic plane. These filaments, although previously detected (Yusef-Zadeh et al., 1984), appear in this MeerKAT image with exceptional quality. Their nature remains a mystery to this day, but they are likely associated with strong magnetic field lines in our Galaxy.

---

[3] To determine the spectral index of an emitting source, the surface brightness, or flux density, must be measured from at least two observing frequencies, but multiple frequencies can be used to better constrain this value: $\alpha = \frac{\log(S_1/S_2)}{\log(\nu_1/\nu_2)}$.

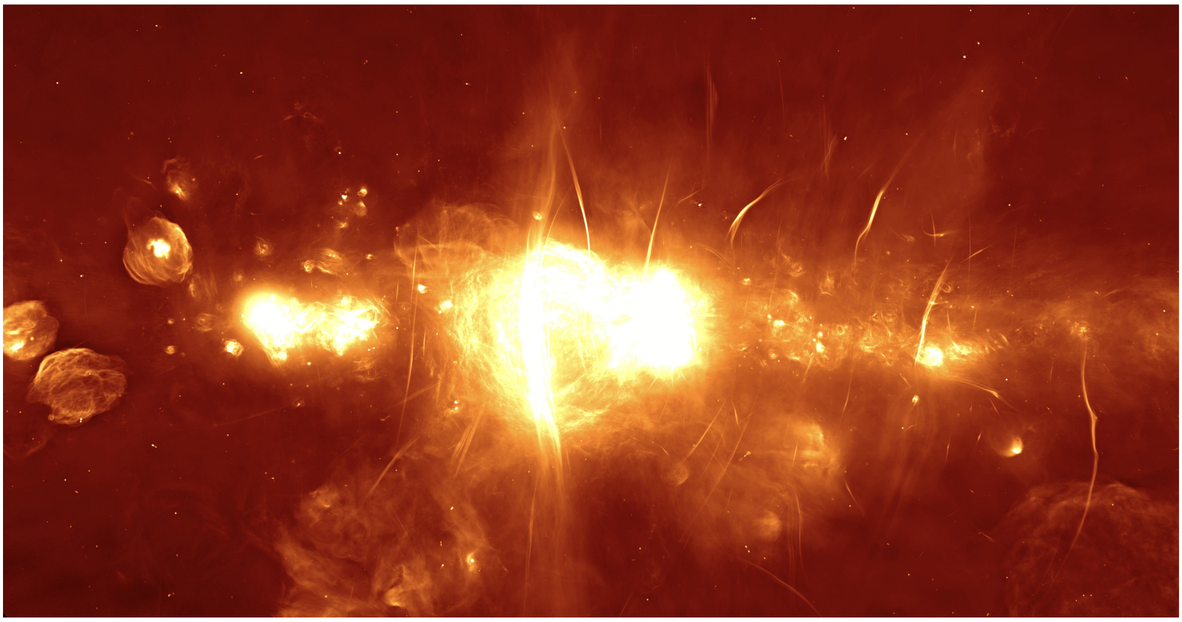

Figure 1.4: The Galactic Center as seen by MeerKAT, as part of the official press release https://www.ska.ac.za/media-releases/meerkat-radio-telescope-inaugurated-in-South-africa-reveals-clearest-view-yet-of-center-of-the-milky-way.

1.1.1.2 Extragalactic Radio Sources

Many other galaxies are sources of radio emission. The non-thermal radio emission of galaxies can come in two forms: galactic halos or active galactic nuclei (AGN). Cygnus A is one of the brightest radio galaxies in our sky due to its radio-emitting AGN which is in the form of two extended radio jets and radio lobes (see Fig. 1.5). The lobes also show so-called hotspots where emission appears much brighter. Historically, radio galaxies were very important for cosmology since they showed that our Universe is evolving. Measuring the luminosity distribution of radio galaxies proved that our Universe could not be static, as was suggested by the steady-state model (Longair, 1966).

There is evidence that all galaxies host a supermassive black hole (SMBH) at their centers, but only a small fraction[4] of galaxies have *active* SMBHs. Material in the Galactic disk is currently in a stable orbit around the SMBH at the center of the Milky Way, therefore our Galaxy does not have an active nucleus. When the nucleus of a galaxy is active, the SMBH at its center accretes nearby material whereby gravitational potential is converted to kinetic energy and thermal radiation (Blandford & Znajek, 1977). This energy release can produce two, bipolar and symmetric, relativistic jets that extend from the galactic center. The accretion disk, torus, and coronae of AGN can emit in infrared, ulraviolet, X-ray, and

---

[4] About 3% of all galaxies (Rosswog & Brüggen, 2011).

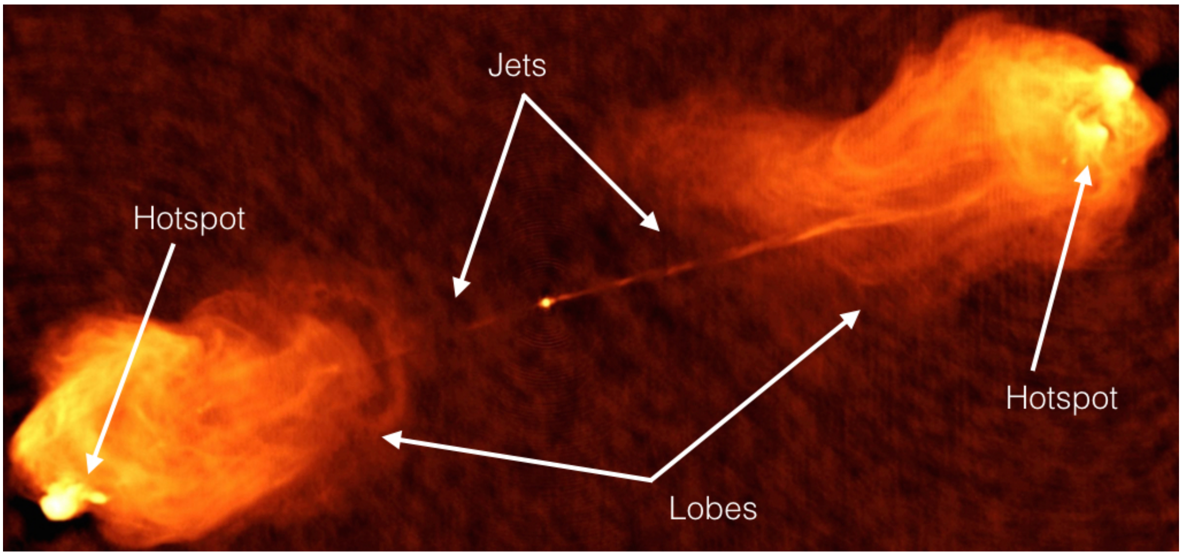

Figure 1.5: The active galactic nuclei of Cygnus A, one of the brightest radio sources in our sky. Image adapted, courtesy of NRAO/AUI.

optical wavelengths; however, the jets, which are made of a plasma of relativistic particles and propelled by magnetic fields, can emit via synchrotron radiation in the X-ray and radio regimes. The radio counterpart of an AGN can extend tens to hundreds of kiloparsecs (kpc) beyond the optical bulge of its host galaxy, into the intergalactic medium.

A prominent example of an AGN is the galaxy M87 and its corresponding radio source, referred to as Virgo A. The radio emission flowing from M87's active core was the first observed astrophysical source of synchrotron radiation (Burbidge, 1956). It is the fourth brightest radio source as seen from Earth and resides nearby within the Virgo galaxy cluster. Fig. 1.6 is one of the lowest frequency images of Virgo A, produced with the LOw Frequency ARray (LOFAR) radio telescope at 140 MHz. This image shows the scale of radio emission extending from the AGN of M87, where two opposing jets are actively supplying the surrounding medium with an injection of fresh radio-emitting plasma. Older plasma, emitting with less intensity, comprises the lobes on either side of the galaxy which span about 80 kpc (de Gasperin et al., 2012).

Active radio galaxies are transient sources with a duty cycle that can change the morphology of their emission (see Morganti, 2017, for a review). The spectral properties, sizes, and shapes of radio galaxies can vary on timescales of months to many years. Radio galaxies can be distinguished into several different categories:

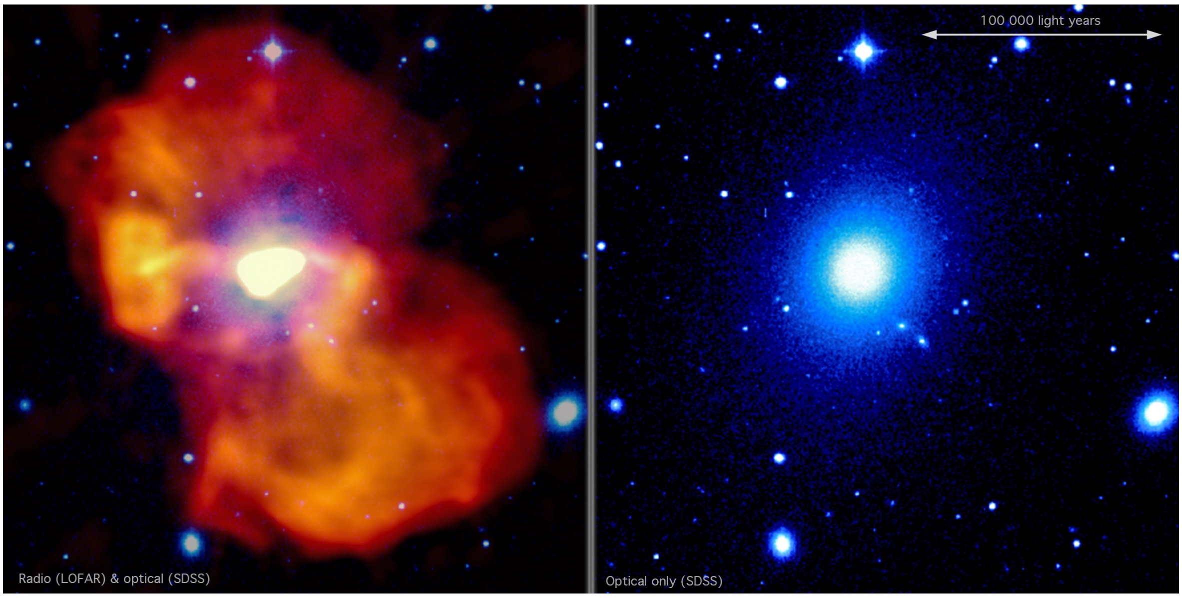

Figure 1.6: Image of Virgo A, the 4th brightest radio emitter in the sky, made with LOFAR (left). Image shows the scale of the radio emission and how it extends into the intergalactic medium beyond the optical emission of M87 (right). From de Gasperin et al. (2012)

- **Fanaroff-Riley:** there are two types of Fanaroff-Riley radio galaxies, type FRI and type FRII, which are distinguished by how their brightness changes over their morphology. FRI galaxies have a radio luminosity that decreases as the distance from the nucleus increases. Conversely, FRII galaxies are classified as radio galaxies that grow much brighter, with observable hotspots in their radio lobes. Hotspots are theorized to occur due to re-energization from turbulence and shocks where jet emission piles up; the emission in hotspots is younger with a flat[5] spectral index (Fanaroff & Riley, 1974).

- **Bent-tails:** active radio galaxies that travel through a medium can experience a strong drag force, or ram pressure, that can morph and bend their jets and lobes (Miley, 1980). Bent-tail (BT) radio galaxies can have jets or lobes that appear, in projection, to be in a wide-opening angle (WAT) or a narrow-opening angle (NAT). Sometimes the two jets are indistinguishable and the radio galaxy appears as a head-tail (HT). See Fig. 1.7 for a diagram of the bending sequence of tailed radio galaxies.

- **Giants:** as the name suggests, giant radio galaxies (GRGs) are a class of radio galaxies with jets or lobes that extend over a large area, with a linear projected size of $\gtrsim 0.7$ Mpc (e.g. Saripalli et al., 2005). GRGs are thought to form in media which are less dense than the media of typical radio galaxies, such that their emission can reach fur-

---

[5] A flat spectral index means that $\alpha \sim 0$, such that the brightness, S, is nearly constant.

ther without much disturbance or resistance from the surrounding medium (Kaiser & Alexander, 1999).

- **Remnants:** after nuclear activity in a radio galaxy has ceased, the remaining emission represents the remnant radio galaxy (Brienza et al., 2016). In a remnant radio galaxy, the compact core, jets, and hotspots are no longer visible. Since there is no longer a supply of fresh plasma from the core, the remaining emission is subject to energy loss, and becomes old, dying, and fading. Remnant radio emission usually exhibits a steep spectral index (e.g. $\alpha < -1$).

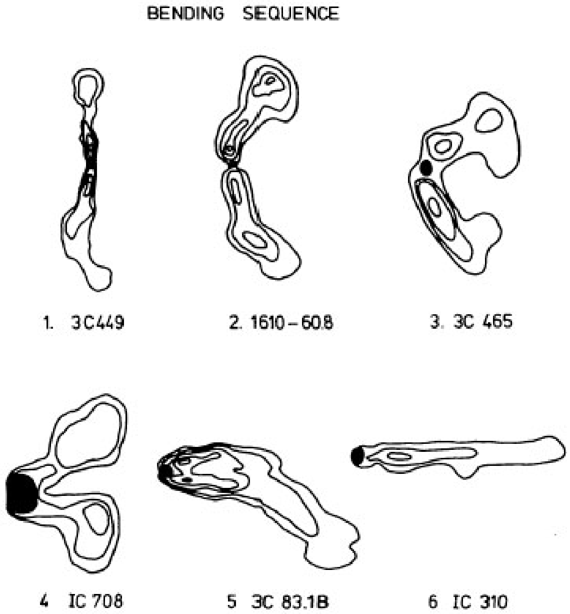

Figure 1.7: Examples of bent-tail radio galaxies. No. 3 is an example of a WAT, while no. 5 is more like a NAT. No. 6 is a HT. From Miley (1980).

1.2 Galaxy Clusters

Galaxy clusters are the largest bound structures in the Universe, gradually forming from the gravitational attraction of matter. Just as each galaxy is enveloped within its own Dark Matter halo, clusters of galaxies are surrounded by a shared Dark Matter halo that influences the interior galaxy group to be gravitationally bound. As a consequence of Cold Dark Matter (CDM), the hierarchical structure growth of the Universe can be described as a bottom-up process, whereby, over billions of years, matter collects to form individual galaxies, galaxies then group together, groups of galaxies attract each other to form clusters, and clusters merge to form superclusters. The merging process between clusters of galaxies reveals the evolution of the large-scale structure of the Universe, where the dense filaments of the cosmic web become separate from the voids.

Typical galaxy clusters can contain anywhere from hundreds to thousands of galaxies, and the largest galaxy clusters have masses $> 10^{15}$ $M_\odot$. In an attempt to set a scale on the size of a galaxy cluster, a virial radius is used, computed as the radius where the interior volume is 200 or 500 times more dense than the critical density[6] of the Universe (where $r_{200} > r_{500}$). This comes from an analytic model for the spherical collapse of an over-density, where the equation of motion of spherical shells is expressed in parametric form and matched to the results of linear structure formation. The solution yields that an over-density which is about 200 times the critical density will collapse. The virial radius can extend anywhere from 1 to 3 Mpc from the cluster center (Peterson & Fabian, 2006). The distribution of matter in a galaxy cluster can sometimes be seen with optical observations and with gravitational lensing maps. Another way to identify clusters and measure their mass is through the Sunyaev-Zel'dovich (SZ) effect (see Sec. A.1.3). The Planck Satellite has been used to measure the SZ effect and estimate the mass of over 1,000 clusters (Planck Collaboration et al., 2016).

Gravitational compression from the Dark Matter halo heats up the matter in the ICM to a very hot 10^8 K. At this temperature the atoms are mostly ionized, and the medium exists as a low-density plasma (10^{-3} particles per cm^3) made up of free electrons and ions. This plasma emits in X-ray wavelengths via thermal Bremsstrahlung radiation (see Sec. A.1.1) and is optically thin, so the radiation escapes freely and the cluster cools over time (Peterson & Fabian, 2006). The surface brightness distribution of the X-ray emission paints a picture of a cluster's morphology since it indicates the location of bulk baryonic matter within the cluster. With X-ray observations it is possible to identify potential cluster mergers which usually show a disturbed distribution of thermal gas. XMM-Newton, Chandra, and other X-ray telescopes have been used to conduct large surveys on hundreds of galaxy clusters. Surveys like ROSAT-ESO (REFLEX; Böhringer et al., 2004) and XMM-BCS (Šuhada et al., 2012) have discovered and identified cluster merger candidates.

When two galaxy clusters merge, a violent and powerful collision[7] of intracluster media takes place. The kinetic energy of a galaxy cluster merger is determined by the potential energy

---

[6] This is a term set by the geometry of our cosmology, where ρ_{crit} is approximately 10^{-29} g cm^{-3}.

[7] The ICM is actually collisionless in the sense that individual particles are not like to physically collide (since there exists only about one particle per 10 cubic meters!); however, Coulomb collisions do take place where particles interact via their electrical fields. In the ICM plasma, magnetically-mediated collisions occur that accelerate particles and lead to photon emission.

Figure 1.8: The Bullet cluster. The pink X-ray gas from each cluster is colliding in the middle after the member galaxies have already passed each other in a high velocity merger. The purple emission represents the location of Dark Matter inferred from weak-lensing maps. From the Chandra X-ray observatory website http://chandra.harvard.edu/photo/2006/1e0657.

of the colliding clusters' mutual gravitational attraction. The Virial Theorem states that the total kinetic energy of all particles within a bound system is half of the potential energy of that system. Since the potential energy, U, of a merger is a sum of gravitational forces, the kinetic energy can be determined by using the expression of potential energy derived from Newton's Universal law of gravity. The kinetic energy, T, of a cluster-cluster merger is then a function of the cluster masses, M_1 and M_2, and the distance between the clusters' centers of mass, R:

$$T = U/2 = \frac{GM_1M_2}{2R}. \tag{1.1}$$

Inserting some realistic values, $M_1 = 10^{15}M_\odot$, $M_2 = 10^{14}M_\odot$, and $R = 5$ Mpc, the kinetic energy of the merger is on the order of 10^{63} erg! This means that galaxy cluster mergers are the most energetic phenomena in the Universe. All of this kinetic energy is dissipated through cluster-wide turbulence and shocks that induce magnetohydrodynamic interactions of baryonic particles in the ICM. An exceptional example of the physical effects of mergers and evidence that Dark Matter is *collisionless* is offered by observations of a Southern cluster nicknamed the 'Bullet Cluster.' X-ray emission from the Bullet cluster, observed by the Chandra X-ray telescope, reveals that a high-velocity (4700 km/s; Springel & Farrar, 2007) merger is taking place, but upon examination it appears that the various components of the cluster are reacting differently to this collision (see Fig. 1.8). Optical observations show that a subcluster of galaxies is exiting after penetrating a main cluster core (as if the subcluster shot through the main cluster like a bullet), but the subcluster's thermal gas lags behind. A weak-lensing map shows that the Dark Matter subhalos, of both the larger and the smaller cluster, merged coincidentally with their own galaxy groups, while the gas from each cluster is stuck in the middle in midst of a collision (Markevitch et al., 2004). Here it is understood that the individual galaxies did not collide (since they are essentially collisionless), but the medium in between galaxies, the thermal gas, is affected by the pressure of the collisional fluid. These observational results of the Bullet cluster and of other similar mergers can be used to put limits on the self-interaction cross-section of Dark Matter (e.g. Randall et al., 2008).

1.2.1 Diffuse Radio Emission in the ICM

Galaxy clusters are not only luminous sources in X-ray wavelengths; they are also rich in radio emission. When observing a cluster at radio frequencies, the brightest sources of emission are typically AGN from active galaxies within the clusters. Most clusters host large, elliptical galaxies called the brightest cluster galaxies (BCGs) that reside at the cluster center, in the minimum of the cluster potential well (Lin & Mohr, 2004). BCGs are very likely to be radio loud, with compact or extended AGN radio emission (Best et al., 2007). A portion of galaxy clusters have also been observed to host peculiar cluster-scale sources of diffuse radio emission that originate from within the intracluster medium (ICM) and have no obvious connection to the individual galaxies within the cluster. These huge, diffuse radio sources indicate that galaxy clusters have a non-thermal component, consisting of cosmic-ray electrons and magnetic fields which permeate the diffuse plasma of the ICM. However, the energy output of this non-thermal component (i.e., the total power emitted by diffuse radio sources in the ICM) is approximately four orders of magnitude less than the energy output of the thermal component (i.e., the total power emitted by X-rays)[8].

Based on their observed radio properties, these cluster-scale sources have been split into two categories: radio halos and radio relics. Both halos and relics are characterized by steep synchrotron spectra ($\alpha \sim -1$) and low surface brightness (~ 1 μJy arcsec^{-2} at 1.4 GHz; see Feretti et al., 2012 for a review). Halos and relics are distinguished morphologically – by their shape and location within the cluster – but also by their origins, which is discussed further in Sec. 1.3. The descriptions of and distinctions between these two emission types are summarized in the following bullet points. Example observations of these sources are given for context.

---

[8] Assuming that a typical diffuse radio source in the ICM is on the order of 10^{24} W Hz^{-1} at 1.4 GHz, or $\sim 10^{40}$ erg s^{-1}, and that the X-ray luminosity of a typical cluster is $\sim 10^{44}$ erg s^{-1}.

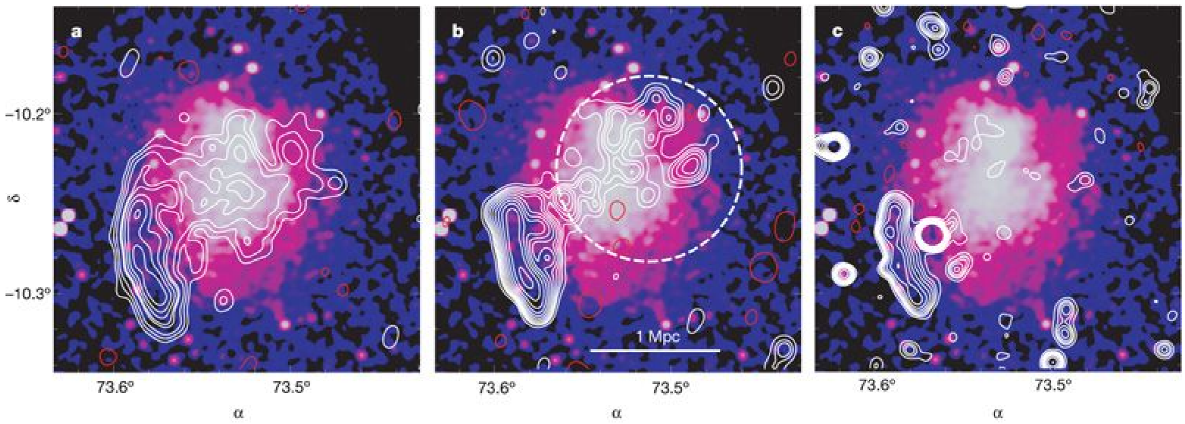

Figure 1.9: Radio contours of the radio halo in Abell 521 overlaid on a Chandra map of X-ray emission. Left: radio contours at 240 MHz. Center: radio contours at 610 MHz. Right: radio contours at 1.4 GHz. The halo is brighter and larger at lower frequencies, with an ultra-steep spectral index of $\alpha \approx -2.1$ (Brunetti et al., 2008).

- **Radio Halos:** Radio halos are classified as diffuse emission filling the central volume of a galaxy cluster. They are roughly 1 Mpc in diameter and are found to follow the distribution of thermal X-ray emitting gas of the ICM. Halos are more often observed in galaxy clusters that are dynamically disturbed (Cassano et al., 2010), and are thought to exist as a result of merger-induced turbulence. The first halo ever discovered was found in the Coma cluster, observed by the Jodrell Bank telescope at 480 MHz (Large et al., 1959). Since this first discovery in 1959, Feretti et al. (2012) have collected results from 42 additional radio halos, and the number is still growing, with 66 known radio halos in 2017 (Johnston-Hollitt & Pratley, 2017). Radio halos are more often found in X-ray luminous clusters ($L_x > 5 \times 10^{45}$ erg s^{-1}) and their radio power has been correlated[9] to their cluster X-ray luminosity (Giovannini et al., 1999b; Giovannini & Feretti, 2002; Cassano et al., 2011). Some halos are observed to exhibit very steep spectra, where $\alpha < -1.5$, and are referred to as ultra-steep-spectrum radio halos (USSRHs). Lower frequency observations have revealed that USSRHs may be more common in lower-mass clusters or clusters that have undergone minor-mergers (e.g. Cassano et al., 2006a; Brunetti et al., 2008). USSRHs may also be a transient phase of a radio halo: as turbulence in the ICM dissipates, the halo brightness fades and the spectrum steepens. In Fig. 1.9 one of the steepest radio halos known, in Abell 521, is shown over three frequencies, and it is apparent that the halo is brighter and larger at low frequencies (Brunetti et al., 2008).

---

[9] Known as the $P - L_X$ correlation. Since the X-ray luminosity of a cluster can be directly related to the cluster mass, there is also a radio halo power versus cluster mass correlation: the $P - M$ correlation.

- **Radio Relics:** Radio relics often appear as arc-shaped or elongated sources that are located in the cluster outskirts. Relics are distinguished from halos in that they are highly polarized sources, typically 30% (Brunetti & Jones, 2014) but in some cases up to 50-60% (e.g. Vazza et al., 2016). The degree of polarization, the steepness of the spectrum, and the surface brightness can change over the morphology of a single relic. The fact that many relics exhibit gradients of surface brightness and spectral index hints at the acceleration mechanisms of the emitting electrons. It is currently accepted that relics are the products of merger-induced shocks (van Weeren et al., 2018). A cluster-cluster merger can produce shock waves that travel outward from the system center, and radio relics are tracers of these shocks, indicating the presence of relativistic electrons and magnetic fields at a distance of > 1 Mpc from the cluster center. In some clusters, double relics have been observed, where two arcs of emission appear opposite each other on the cluster perimeter. A clear example of a relic pair is given in Fig. 1.10 where a composite image of the galaxy cluster PLCKG287.0+32.9 shows X-ray emission in red and two radio relics in blue, as observed by the Very Large Array (VLA) at 1.4 GHz (Bonafede et al., 2014b).

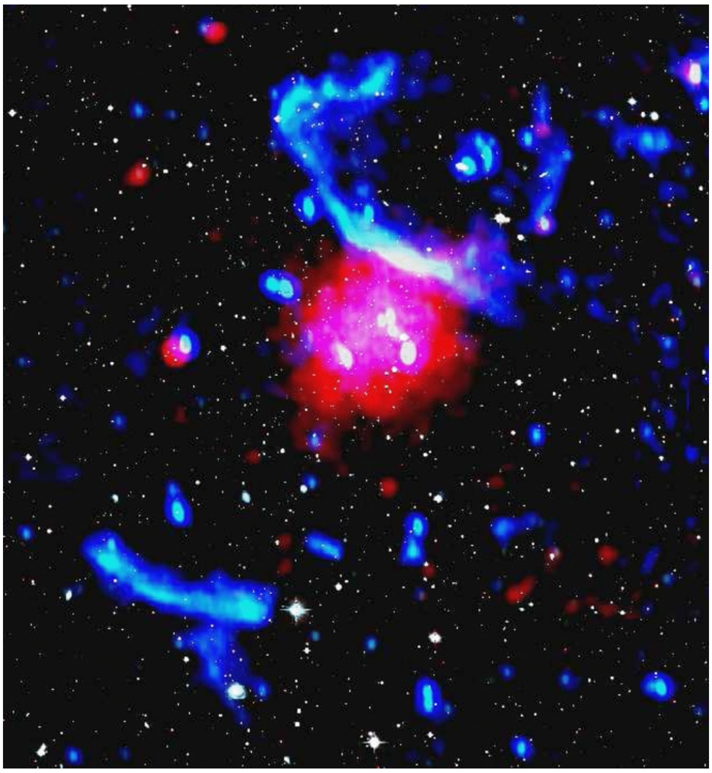

Figure 1.10: Composite image of PLCKG287.0+32.9. Radio emission is in blue (two radio relics) and X-ray emission is in red (the hot gas of the ICM). From Bonafede et al. (2014b).

1.2.2 Statistical Studies of Galaxy Clusters

To understand the physical mechanisms powering radio halos and relics, it is necessary to determine the distribution of these sources in relation to cluster properties such as mass or dynamical state. Comparing radio observations of galaxy clusters to X-ray observations has alluded to an interesting pattern: non-merging, cool-core[10] clusters do not host the same giant radio structures that are seen in disturbed, merging clusters. Not all disturbed, merging clusters show halos or relics, and a few cool-core clusters have been observed to host large-scale radio halos (e.g. Bonafede et al., 2014a), but of the clusters which do host halos and relics, the common trend is that they are usually merging systems.

During a merger, the distribution of the hot gas of the ICM changes its morphology, and this is represented in the X-ray surface brightness distribution of the cluster. X-ray observations are used to compute the dynamical status of a cluster, and clusters can be compared based on their dynamical properties. Two commonly used parameters for determining dynamical status include the concentration parameter, c, and the centroid-shift, w. The concentration parameter is the ratio of X-ray flux within a radius of 100 kpc (around the cluster center) over the X-ray flux within a radius of 500 kpc (Santos et al., 2008). Clusters that have a compact core, which has not been disrupted by merger activity, have higher concentration parameters. The emission centroid-shift is defined as the standard deviation of the shift between the peak and the X-ray centroid for n circles with increasing radius. High values of w indicate that the system is disturbed. The w and c parameters of several clusters have been compared, and it has become clear that radio halos are more commonly found in merging (i.e. dynamically disturbed) clusters (Cassano et al., 2007, 2013; Cuciti et al., 2015). In Fig. 1.11 a sample of clusters are plotted by their concentration versus centroid-shift parameters.

Because of their low surface brightness and large angular extent, radio telescopes need to be very sensitive with a large collecting area to be able to detect radio halos and relics. In the last two decades, radio surveys have been used to hunt for these rare sources. Surveys conducted with the VLA showed that diffuse emission is present in 27-44% of X-ray luminous galaxy clusters (where $L_X > 5 \times 10^{44}$ erg s^{-1}; Giovannini et al., 1999a). Gathering the results of all-sky surveys from the NRAO VLA Sky Survey (NVSS; Condon et al., 1998) and Westerbork Northern Sky Survey (WENSS; Rengelink et al., 1997), and combining these images with X-ray catalogues, revealed that dozens of galaxy clusters contained diffuse radio sources. The Giant Meterwave Radio Telescope (GMRT) Radio Halo Survey (Venturi et al., 2008) and a low-frequency follow up (Giacintucci, 2011) added to the list of known radio halos, mini

---

[10] A cool-core cluster shows a significant drop in temperature ($< 10^7 - 10^8$ K) within the inner 100 kpc.

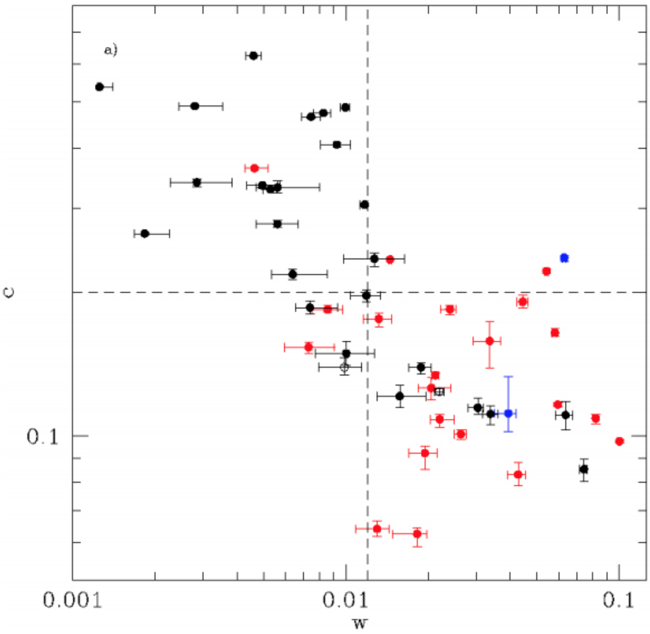

Figure 1.11: Sample of clusters with masses $> 6 \times 10^{14}$ $M_\odot$ plotted by their concentration parameter c vs. their emission centroid-shift w from Cuciti et al. (2015). Red dots indicate clusters hosting radio halos and black dots indicate clusters without radio halos. The dashed lines represent a non-merging / merging boundary as defined by Cassano et al. (2010).

halos[11], and radio relics. An online database for all known diffuse radio sources associated with galaxy clusters is now available at GalaxyClusters.com.

Most of the halos known today have radio fluxes measured at 1.4 GHz. Halos typically have a radio power between 10^{23} W Hz^{-1} and 10^{25} W Hz^{-1} at 1.4 GHz. The radio power and size of halos has been correlated with other properties of their hosting clusters. Correlations for halo power or halo radius versus cluster mass and cluster X-ray luminosity are presented in Cassano et al. (2007, 2010, 2013). These statistical studies have revealed that brighter, larger halos typically occur in more massive and more X-ray luminous clusters, with the $P - M$ correlation being a straight line with a slope of ~ 3.4 in a log-log plot of halo power versus cluster mass. Johnston-Hollitt & Pratley (2017) have gathered the statistics on 58 halos, known at the time, on a single $P - M$ plot, as shown in Fig. 1.12. Since the correlation has been derived mainly using observations at higher frequencies, it is expected that the correlation may change as more halos are discovered at lower frequencies. Sensitive, low-frequency radio arrays, such as LOFAR, the Murchison Widefield Array (MWA), and the upcoming SKA, may also reveal a large population of fainter, smaller, and steeper halos than those that were used to set the original correlation at 1.4 GHz.

---

[11] Mini halos have been observed in non-merging, cool-core clusters and are smaller and less bright than radio halos found in merging systems.

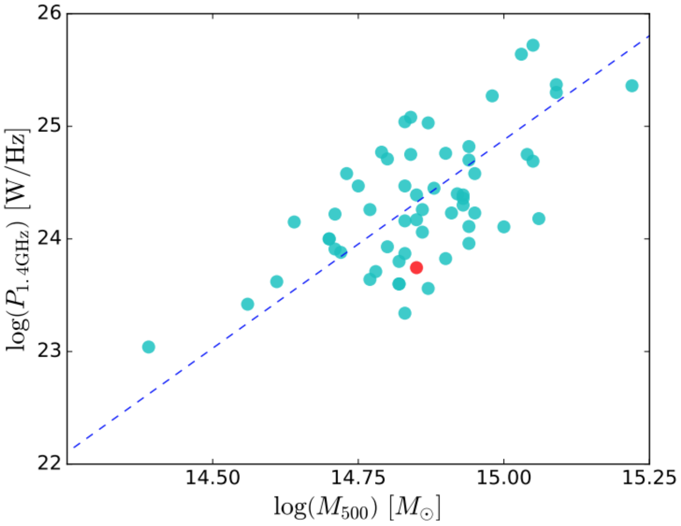

Figure 1.12: The $P - M$ correlation for a sample of radio halos. The aqua dots are the 57 known halos in the literature with SZ-derived mass. The correlation fit of Cassano et al. (2013), using a subset of 25 clusters, is shown by the dashed line, and Abell 3667 is marked by a red dot (Johnston-Hollitt & Pratley, 2017).

1.3 Physics in the Intracluster Medium

A challenge arises in determining how radio halos and relics can emit on such large scales. The magnetic field of the ICM has been measured to be on the order of a few μG (Carilli & Taylor, 2002; Bonafede et al., 2010a). The radiative lifetime of cosmic-ray electrons (CRe) emitting radio-frequency photons, in a B-field of such strength, is on the order of 10^7 yr, after accounting for energy loss via synchrotron emission and Inverse Compton scattering (see Sec. A.1.3). The diffusion of CRe (governed by the Alfvén speed) during this lifetime extends only on the order of ~ 100 kpc. Diffusion across Mpc-scales, assuming efficient CR drift at the Alfvén speed, would take several Gyrs. However, the synchrotron emission of the diffuse sources observed in galaxy clusters is typically on the order of ~ 1 Mpc. This is known as the *slow diffusion problem*, which is elaborated upon and quantified in Brunetti & Jones (2014). To address this problem, it is required that the emitting electrons must be re-accelerated, re-energized, or generated *in situ* (Jaffe & Perola, 1973) to explain the large physical extent of relics and halos. How these ICM electrons receive continuous injections of energy and where this population of electrons comes from are the big questions currently under investigation.

1.3.1 Acceleration Mechanisms

There are a few models that attempt to explain the origin of cluster-scale radio emission, and the models differ between radio halos and radio relics. Although the acceleration mechanisms that power radio halos and relics are distinct, they are attributed to the same driver: cluster mergers. Merger-induced turbulence and shocks are the catalysts for particle re-acceleration in the ICM.

1.3.1.1 Turbulent Re-acceleration in Halos

Turbulence arises during a merger event from the ICM sloshing in a changing potential well, shearing instabilities, and interactions between shocks. As the ICM is collisionless, turbulence is propagated via Alfvénic and magnetohydrodynamic (MHD) effects that occur on scales between $100-400$ kpc, while smaller scales of turbulence are introduced by plasma instabilities. The largest scale, at which turbulence is injected, is essentially the size of the system, and the smallest scale is the scale at which turbulence dissipates. Based on the theory of ionized gases (Spitzer, 1962), one can work out the viscosity of the ICM which then yields an effective Reynolds number of $Re \sim 10^3$. Most simulations of the ICM are inviscid, but the numerical viscosity reaches similar Reynolds numbers. Figure 6 in Brunetti & Jones (2014) shows a schematic of the turbulent properties of the ICM. The energetics of these turbulent motions can go into accelerating particles in the ICM (Melrose, 1980). In this case, second-order Fermi acceleration dominates, where charged particles interact with magnetized "clouds" that act as *magnetic mirrors*. In a head-on collision the particle and magnetic cloud are moving toward each other and the particle gains energy ($\Delta E \propto \frac{v^2}{c^2}$). If the magnetic cloud is moving away from the particle, it will lose energy. However, in an environment with highly random motions, more particles are accelerated on average (Fermi, 1949).

The *turbulent re-acceleration*, or leptonic, model suggests that turbulence produced from cluster mergers is responsible for re-accelerating electrons in situ, leading to diffuse radio emission throughout the inner volume of the merging system (Petrosian, 2001; Brunetti et al., 2001). A population of mildly-relativistic electrons is necessary, since MHD turbulence is not efficient enough to accelerate particles to relativistic energies from the thermal pool[12] (e.g. Chernyshov et al., 2012). The efficiency of turbulence in re-accelerating cosmic rays is more complex, but can be related to the overall energy budget of the system, which is related to the masses of the sub-structures that are merging. High-mass mergers are then expected to generate brighter diffuse radio emission that is detectable at higher radio frequencies. Lower-mass mergers, or

---

[12] This term refers to the energy state of the non-relativistic particles in the ICM, which are responsible for thermal Bremsstrahlung radiation.

minor-mergers, are expected to less efficiently re-accelerate cosmic rays, which may lead to diffuse radio emission that exhibits steeper spectra and hence can only be detected at lower radio frequencies (Cassano et al., 2006b; Cassano, 2009).

Simulations have improved over the last decades in modeling turbulent re-acceleration in a magnetized plasma (e.g. Porter et al., 2015; Vazza et al., 2017; Wittor et al., 2017). Uncertainties remain in resolution limitations and in our understanding of how energy is transferred between large and small scales in relation to the magnetic fields of the ICM. Energy injection starts on a large-scale, from the initial perturbations of the merger event, and large-scale eddies cascade down to create smaller-scale eddies, but it is still unknown how small-scale dynamo translates on a larger scale. A recent simulation reaches a resolution of $\sim$ 4 kpc, showing evidence of significant magnetic field amplification (Vazza et al., 2018). Magnetic fields are further discussed in Sec. 1.3.2.

A secondary model, called the *hadronic* model, suggests that the radio-emitting CRe that power radio halos come as secondary particles from an interaction occurring between thermal protons and cosmic-ray protons (CRp) via the production of pions. This interaction should also produce gamma-rays, making galaxy clusters detectable gamma-ray sources. However, observations by the Fermi-LAT satellite have not detected a single galaxy cluster (S. Zimmer for the Fermi-LAT Collaboration, 2015). Stacking the gamma-ray non-detections has constrained the average gamma-ray emission in galaxy clusters (e.g. Vazza et al., 2015). This constraint reveals that the secondary electrons produced by hadronic collisions alone are not enough to explain radio halos. Still, secondary electrons may play a role in providing *seed* electrons and in powering mini halos in cool-core clusters (e.g. Pfrommer & Enßlin, 2004).

1.3.1.2 Diffusive Shock Acceleration (DSA) in Relics

The ‘Sausage’ relic, located in the Northern outskirts of the merging cluster CIZA J2242.8+5301, is one of the most studied. At 1.4 GHz the relic appears to be $\sim$ 2 Mpc long and only 55 kpc wide at a distance of 1.5 Mpc from the cluster center. A multi-frequency spectral study of the radio emission has revealed a spectral gradient along the width of the relic that steepens in the direction toward the cluster center. The radio emission is also strongly polarized, indicating that the magnetic field is aligned with the relic (van Weeren et al., 2010). The ‘Toothbrush’ relic is another fascinating source; it is one of the brightest and largest relics known to date. It is hosted within the merging galaxy cluster 1RXS J0603.3+4214 which also contains fainter, smaller relics, and a radio halo. The Toothbrush relic has a spectral index gradient where the outer, Northern edge shows a flatter spectrum indicative of younger emission. It has been suggested that this relic is the result of a Northward-moving shock. The interior edge is a post-shock region and has a steeper index due to energy losses of the emitting electrons after the shock has moved through. The radio emission in the Southwest portion of the relic, representing the "bristles" of the Toothbrush, also appears to be possibly connected to centrally located diffuse emission (van Weeren et al., 2016c).

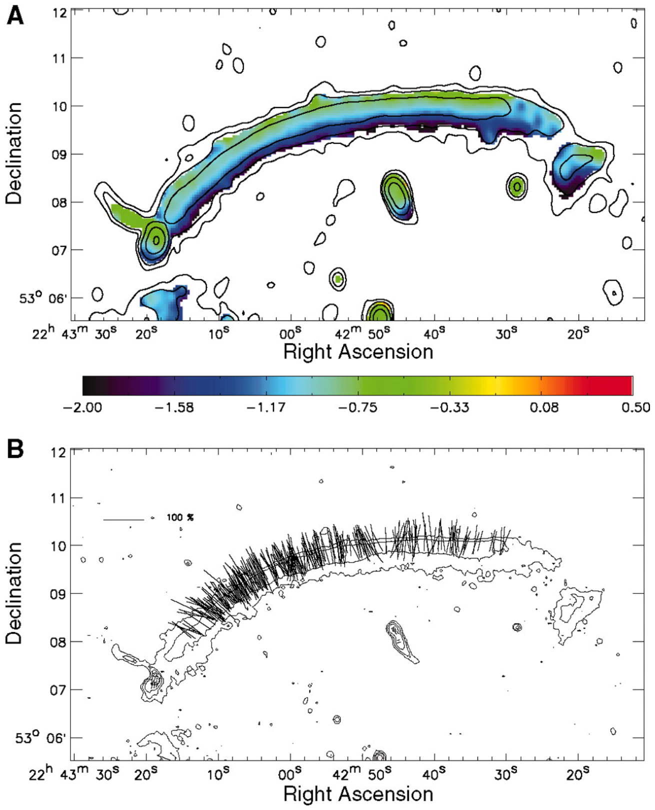

Figure 1.13: Panel A shows how the spectral index varies over the width of the Sausage relic. Panel B shows the radio polarization E vectors, obtained by VLA at 4.9 GHz, which indicate that the B vectors are aligned parallel to the shock (van Weeren et al., 2010).

As already mentioned in Sec. 1.2.1, the morphology and radio properties of radio relics reveal much about their origins. Since many radio relics appear as long, thin sources on the cluster periphery, and are sometimes seen in pairs on opposing sides of the cluster, they appear to be clear tracers of large-scale merger shocks. Merger-induced shocks typically have a Mach number between $\mathcal{M} \sim 1 - 4$ and they propagate outwards along the merger axis, existing for hundreds of millions of years. They are different from accretion shocks, which have higher Mach numbers but much lower energy fluxes. Accretion shocks have never been observed, but are predicted from cosmological simulations. The thin and elongated appearance of some radio relics, in an arc concave to the cluster center, is consistent with a shockwave seen

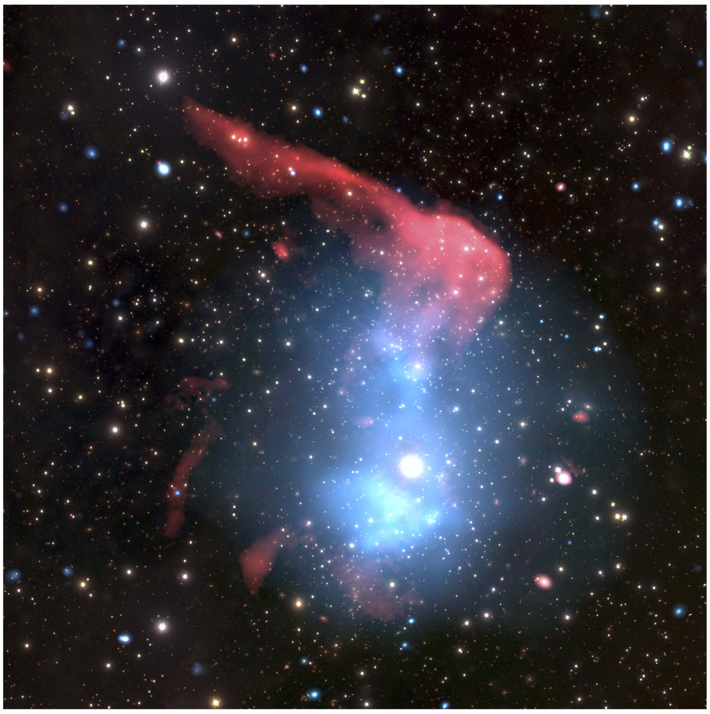

Figure 1.14: Composite image of the toothbrush relic. Red emission is radio, blue is X-ray, among the multitude of optical galaxies within the cluster. From van Weeren et al. (2016c).

edge-on which has traveled from the cluster center outward. Many radio relics are also confirmed to coincide with discontinuities in X-ray brightness and temperature, which indicate a shocked region (e.g. Giacintucci et al., 2008; Ogrean & Brüggen, 2013; Botteon et al., 2016).

At the location of the shock front magnetic fields are compressed and cosmic rays are accelerated, which leads to the observed synchrotron emission with a spectrum that steepens in the downstream direction, as the post-shock regions are then susceptible to energy loss. The process of acceleration over the shock front is the same as that which occurs in the shocks of SNe, except, in the case of clusters, the shocks have a lower Mach number since they propagate over such a large scale. First order Fermi acceleration is possible in collisionless mediums containing magnetic fields, where particles are accelerated to high energies. First theorized in 1978 by Bell (1978), it is possible for high-velocity particles to be confined to a region within a shock so that the particle continuously passes back and forth, upstream and downstream, through the shock front. These high-velocity particles are confined to pass through the front because of their Alfvén waves. With each pass, the particle gains energy and is accelerated. This is called *diffusive shock acceleration* (DSA), and has been theorized as the main acceleration mechanism in relics (Ensslin et al., 1998). According to DSA theory, the distribution of the electrons accelerated at the shock, as a function of their momentum, p, follows a power-law (e.g. Blandford & Eichler, 1987; Drury, 1983):

$$f\left(p\right) \propto p^{-\delta_{\text{inj}}}, \tag{1.2}$$

where the slope, δ_{inj}, or the *momentum injection index*, is related to the Mach number, $\mathcal{M}$, via (Brunetti & Jones, 2014)

$$\delta_{\text{inj}} = 2 + \frac{2\left(\mathcal{M}^2+1\right)}{\mathcal{M}^2-1}. \tag{1.3}$$

In the limit of a strong shock, $\mathcal{M} \gg 1$, $\delta_{\text{inj}} = 4$. In the presence of energy losses from synchrotron emission and Inverse Compton scattering, we can express the distribution as a function of the distance from the shock surface, x, as (Ensslin et al., 1998)

$$f\left(p,x\right) = Cp^{-\delta_{\text{inj}}}\exp\left(-p\left(F+Gx\right)\right), \tag{1.4}$$

where C, F, and G are constants that depend on the diffusion coefficients and the parameters of the cooling mechanism. Integrating over the full shock width gives the integrated momentum distribution of the electrons:

$$f(x) = Cp^{-\delta_{\text{inj}}}\ \mathrm{e}^{-pF}\int_0^D \mathrm{e}^{-pGx}dx \ = \ \frac{Cp^{-\delta_{\text{inj}}}\ \mathrm{e}^{-pF}}{pG}\left(1-\mathrm{e}^{-pGD}\right), \tag{1.5}$$

which implies that the integrated distribution is steeper by one:

$$\int_0^D f\left(p,x\right)dx \ \propto \ p^{-\left(\delta_{\text{inj}}+1\right)}, \tag{1.6}$$

i.e. $\delta = \delta_{\text{inj}} + 1$. Next we compute the synchrotron spectrum that ensues from such a population of electrons. The total power emitted by a single electron per frequency interval is (Rosswog & Brüggen, 2011)

$$\frac{dW_\nu}{dt}\left(\gamma\right) = \frac{4}{3}\sigma_T c\beta^2\gamma^2 u_B \Phi_\nu\left(\gamma\right), \tag{1.7}$$

where σ_T is the Thompson cross-section, u_B is the energy density in the magnetic field, and the function $\Phi_\nu\left(\gamma\right)$ contains the spectral shape of an electron with a Lorentz factor γ. Since the synchrotron spectrum peaks near the critical frequency, $\nu \approx \nu_c \approx \gamma^2\nu_L$ where the Larmor frequency is $\nu_L = \frac{eB}{2\pi m_e}$, we can use $\Phi_\nu\left(\gamma\right) \approx \delta\left(\nu-\nu_c\right)$, and since $E = \gamma m_e c^2$, then $\gamma \propto p$, and we can express the electron distribution f in terms of γ as $f\left(\gamma\right) \propto \gamma^{-\delta_{\text{inj}}}$. Now the integral over the electron distribution can be written as an integral over γ:

$$\frac{dW_\nu}{dt} = \int \frac{dW_\nu}{dt}(\gamma)\ df(\gamma) = \propto \int \gamma^{2-\delta}\delta(\nu - \nu_c)\, d\gamma, \tag{1.8}$$

where we have used $\beta^2 \approx 1$. Collecting the constants into C_0 and substituting $\nu' \equiv \gamma^2 \nu_L$, we have

$$\frac{dW_\nu}{dt} = \frac{C_0}{2\nu_L} \int \left(\frac{\nu'}{\nu_L}\right)^{-\frac{\delta-1}{2}} \delta(\nu - \nu')\, d\nu' = \frac{C_0}{2\nu_L}\left(\frac{\nu}{\nu_L}\right)^{-\frac{\delta-1}{2}}. \tag{1.9}$$

Thus, the synchrotron emissivity of the electrons also follows a power-law, with a spectral index α:

$$j_\nu \propto \nu^{-\alpha}, \tag{1.10}$$

where $\alpha = (\delta - 1)/2 = \alpha_{\text{inj}} + 1/2$. Contrary to the previous text, here it must be noted that α has a positive value. We can now infer the Mach number of the shock from the radio spectrum, where a spatially resolved measurement at the shock front yields the injection spectral index, α_{inj}, and an unresolved measurement over the downstream region yields the integrated spectral index, α.

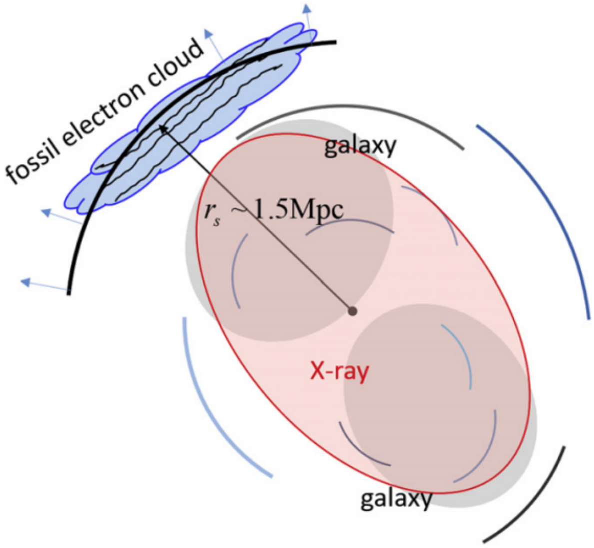

Figure 1.15: "Schematic diagram illustrating a scenario for the Sausage relic in a merging cluster, CIZA J2242.8+5301: a shock impinges on a fossil electron cloud with regular magnetic field in the cluster outskirt. Two gray disks represent the galaxy distribution, while the red ellipse shows the distribution of X-ray emitting gas. Arcs are meant to depict abundant shocks with different Mach numbers that are expected to form during a merger event" (Kang & Ryu, 2015).

In order for DSA to power radio relics with brightnesses comparable to those of the Sausage or Toothbrush relics, electrons can not be accelerated from the thermal pool. Instead, mildly-energetic "fossil" electrons must be re-accelerated (see e.g. Pinzke et al., 2013; Kang & Ryu, 2015; see also Fig. 1.15). The source of these seed electrons existing in the cluster periphery is still being investigated (see Sec. 1.3.3). There are also inconsistencies with the Mach numbers of the merger shocks as measured by X-ray observations compared to the Mach numbers inferred by the radio injection spectral indices of radio relics (e.g. van Weeren et al., 2012; Ogrean & Brüggen, 2013). Low-frequency observations may reveal fainter radio relics and cases where radio relics are clearly being fed by fossil plasma (e.g. Nuza et al., 2012).

1.3.2 Magnetic Fields

Magnetic fields are a ubiquitous feature in intracluster media, and mediate merger-driven turbulence and shocks. They are an important factor of the energy content of diffuse radio sources in galaxy clusters. The minimum value of total energy can be determined when assuming that the energy contribution from cosmic rays and the energy contribution from magnetic fields are equal. The magnetic field, or B-field, under the equipartition condition is stated as B_{eq}. Assuming equipartition conditions, the non-thermal properties of the ICM are derived as having an energy density of 10^{-15} erg cm^{-3} to 10^{-13} erg cm^{-3} and $B_{\mathrm{eq}} \sim 0.1$ to 1 μG.

The origin of cluster magnetic fields is not known, but it may be partially comprised of a primordial seed field that has been amplified on smaller scales due to plasma instabilities. Galaxy formation and galaxy outflows may also contribute to the cluster magnetic field (e.g. Donnert et al., 2009). The magnetic field strength has been measured in some galaxy clusters using Faraday Rotation[13] Measurements of polarized radio emission. Bonafede et al. (2010b) measured and simulated the magnetic field strength in clusters and found that it decreases as the distance from the cluster center increases. This contradicts the evidence of powerful radio relics in the cluster outskirts. But shocks may play a part in adiabatic compression, which can amplify the magnetic field locally, and in generating magnetic fields (e.g. Brüggen, 2013b; Guo et al., 2014). See Brüggen (2013a) for a brief review of magnetic fields in the ICM.

---

[13] Faraday Rotation, or the Faraday effect, can occur to light traveling through a magnetized medium. This effect induces a rotation of the plane of polarization and it is linearly proportional to the magnetic field vector.

1.3.3 Seed Electrons

The underlying ingredient of radio halos and relics is a population of mildly-relativistic electrons which are to be re-energized or re-accelerated. Turbulent re-acceleration (i.e. Fermi II acceleration) and DSA (i.e. Fermi I acceleration) are not efficient enough to accelerate thermal electrons to ultra-relativistic energies. Electrons are more difficult to accelerate than protons since their Larmor radii are much smaller. For example, in the case of DSA, the Larmor radius of thermal electron is much smaller than the typical thickness of a shock, but protons can re-cross the shock several times, thus increasing the chances of getting scattered by magnetic field fluctuation. Therefore, it is necessary that these particle acceleration mechanisms operate on a population of mildly-relativistic electrons in situ. This so-called *injection problem* for electrons is still largely unresolved (see pages 14-15 from Brunetti & Jones, 2014). A mystery remains in explaining where this population comes from and how these mildly-relativistic electrons fill the ICM so uniformly, even in the cluster outskirts. There have been attempts to explain this either from primordial conditions or from injections of seed electrons from cluster galaxies.

Simulations have shown that cosmological shock waves from the initial formation of the large-scale structure can supply the ICM with a significant population of high-energy cosmic rays (e.g. Ryu et al., 2003). Outflows from non-active galaxies have also been considered, but their contribution of CRp is likely to be less than 0.1% of the thermal energy budget in the ICM (Brunetti & Jones, 2014). Outflows from AGN are considered to be better contributors. It is predicted that about half of the output power of AGN goes into heating the ICM, which suppresses the radiative cooling in clusters (McNamara & Nulsen, 2007). The output of CRe has been measured in the radio lobes of some BCGs (Hydra A and Hercules A) to be up to 10% of the total energy output, but observations in hard X-rays would be necessary to determine the full electron content in radio lobes (Hardcastle & Croston, 2010).

A more difficult problem entails assessing the efficiency at which cosmic-ray electrons can then be transported and dispersed over the full volume of the ICM. However, radio-loud AGN are often seen distributed throughout clusters, and arguments have been made that, collectively, lower-luminosity AGN may dominate the AGN energy contribution to the ICM (Stocke et al., 2009). Even if transportation is efficient, is there enough energy in the transported CRe to account for the full population of necessary seed electrons? Low-frequency observations of radio galaxies may help us to answer this. For example, LOFAR observations have revealed the presence of faint fossil plasma from remnant radio galaxies in cluster environments (e.g. Brienza et al., 2017). Examples also exist where AGN are observed to directly contribute emission to radio relics (e.g. van Weeren et al., 2017). Re-brightening of AGN emission has

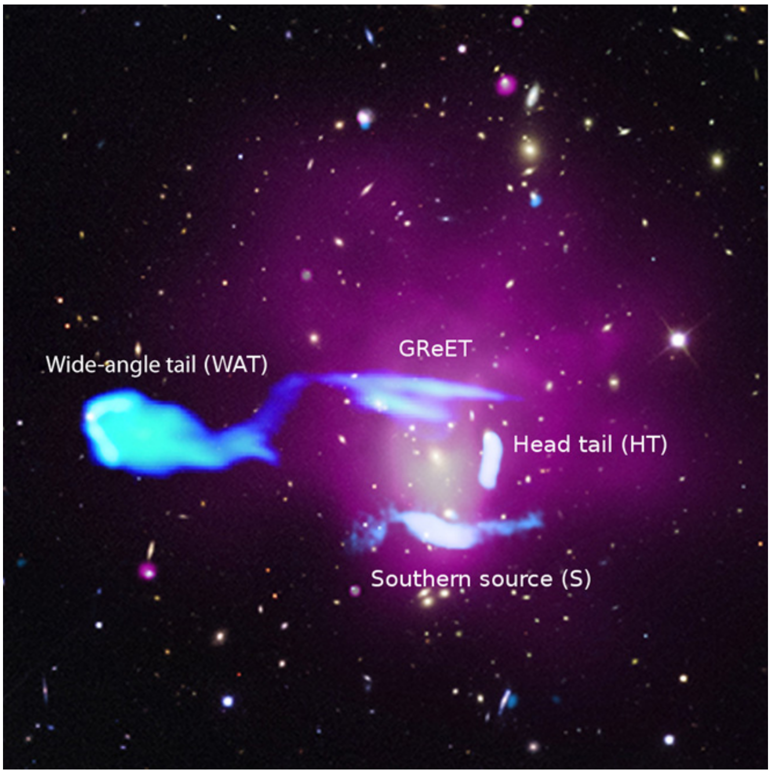

Figure 1.16: The background is an optical image of Abell 1033. The X-ray emission is shown in purple, tracing thermal gas of the ICM. The blue emission is the radio emission detected by LOFAR, tracing cosmic-ray electrons. From de Gasperin et al. (2017).

also been observed, so called radio *phoenixes* (e.g. Ogrean et al., 2011). Recently a new kind of radio sources was discovered, a GReET (gently re-energized tail), where the two tails of a WAT have re-brightened due to shocks and turbulence re-energizing the emission (de Gasperin et al., 2017; see Fig. 1.16).

1.4 Radio Astronomy in Practice

Now that the astrophysics of radio sources in galaxy clusters has been discussed, I will address the technical details of obtaining radio images. Very low frequencies, between 10 - 1000 MHz, are difficult for astronomical observations because they require meticulous means to achieve images in high resolution, and because the ionosphere has a distorting effect on the incoming radio waves. Much like the waves on the surface of water distort the image of an underwater object, the ionosphere distorts radio wavefronts, making a radio source appear to physically waver during the observation. Radio astronomers have developed special algorithms to model and account for these effects, further discussed in Sec. 1.4.3.

The efforts of many radio astronomers have been to increase the size of the radio dish because it allows for better resolution, but the hardware that goes into making very large radio dishes is expensive and the resulting dish is difficult to maneuver. Thus, radio astronomy has evolved from single-dish telescopes to digitized antenna arrays. The technique of using multiple antennas in synchronization is called radio interferometry. Array interferometers are a much more practicable alternative as they can observe with higher resolutions using more simplistic hardware. Among other arrays, the VLA in New Mexico, the GMRT in India, and LOFAR in Europe were built to surmount long wavelength complications and unveil a large window of the electromagnetic spectrum. The upcoming Square Kilometer Array[14], currently undergoing construction in South Africa, will be the largest radio array in the world.

1.4.1 Radio Interferometry

Radio interferometry can be simplified by the interaction of two antennas. The distance between the two antennas (or baseline) is the effective aperture of those two antennas. The resolution of an image of a source observed by the two antennas is equivalent to the resolution afforded by a single large dish with a diameter equal to the baseline between the two antennas. However, the intensity of the image is far less owing to the difference in area such a large dish would have over the two small antennas. This is compensated for by adding more antennas and creating an antenna array. For an array with N antennas, there are $(N^2 - N)/2$ independent baselines. By modifying the Rayleigh Criterion, the dish diameter now becomes the maximum baseline $\boldsymbol{b}_{\max}$ – the maximum distance between the antennas that are synchronized in the array. For a fixed observing frequency, ν, as $\boldsymbol{b}_{\max}$ increases, the resolution of the array is sharper and radio astronomers are therefore able to study more distant radio sources.

Illustrated in Fig. 1.17, two antennas are a distance $\boldsymbol{b}$ apart, and both receive a radio signal in the direction $\boldsymbol{s}$ from the source at which they are pointed (Thompson, 1999). The signal enters as a wavefront and meets one antenna before the other, as it is coming in at an angle θ. This causes a delay between the receivers which is accounted for by a correlator between the two antennas. The correlator combines the antenna voltages as an interference pattern. This pattern, in complex numbers, is what is recorded as *visibility data*, corresponding to the frequency domain. A Fourier transform on the visibility function, $\mathbf{V}_\nu$, is all that is needed to return this information to the spatial domain and produce an intensity, I_ν, image. However, the true radio signal from the sky has been perturbed by both direction-independent (DI)

---

[14] https://www.skatelescope.org

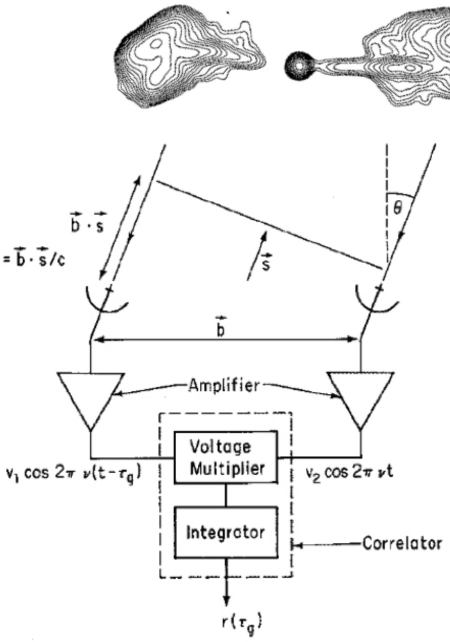

Figure 1.17: Aperture synthesis between two antennas adapted from Thompson (1999). Radio source is 3C438, image by Martin Hardcastle.

and direction-dependent (DD) effects. The electronics of the instrumentation (as the signal goes from the amplifier to the voltage multiplier, for example) and small discrepancies in station clocks account for the DI effects. More complex are the DD effects, which include station *beams*, the ionosphere, and Faraday rotation. The Radio Interferometry Measurement Equation (RIME; Hamaker et al., 1996) models these effects as linear transformations, also called Jones matrices (**F** for DI effects and **G** for DD effects, as expressed below), so that they can be solved for, and the visibility function, $\mathbf{V}_{(p,q),t\nu}$ between antennas p and q at time t and frequency ν, can be transformed into the true underlying source coherency matrix $\mathbf{X}_s$. From the *sky term*, $\mathbf{X}_s$, a spatial intensity image of the radio signal in the direction $\boldsymbol{s}$ $= \left[\mathrm{l}, \mathrm{m}, \mathrm{n} = \sqrt{1-l^2-m^2}\right]^T$ can be produced (e.g. Tasse et al., 2018):

$$\mathbf{V}_{(p,q),t\nu} = \mathbf{F}_{pt\nu}\left[\int_s (\mathbf{G}_{pst\nu}\mathbf{X}_s\mathbf{G}^H_{qst\nu})k^s_{(p,q),t\nu}d\boldsymbol{s}\right]\mathbf{F}^H_{qt\nu}, \tag{1.11}$$

where $k^s_{(p,q),t\nu}$ describes the effect of the array geometry and correlator on the observed phase shift of a coherent plane wave between antennas p and q:

$$k^s_{(p,q),t\nu} = \exp\left(-2i\pi\frac{\nu}{c}\left(\boldsymbol{b}^T_{(p,q)t}(\boldsymbol{s}-\boldsymbol{s_0})\right)\right), \tag{1.12}$$

$$\boldsymbol{b}_{(p,q)t} = \begin{bmatrix} u_{pq,t} \\ v_{pq,t} \\ w_{pq,t} \end{bmatrix} \tag{1.13}$$

Solving for the DI and DD effects (**F** and **G**, respectively) and correcting for those effects is called calibration. The direction-independent effects (outside of the integral in Eq. 1.11) can be directly applied to the visibility data to give corrected visibilities:

$$\mathbf{V}_{\mathrm{corr}} = \mathbf{F}_p^{-1}\mathbf{V}\mathbf{F}_q^{-H}. \tag{1.14}$$

However, the corrected visibility data still contains direction-dependent effects. The specific calibration techniques used in this thesis to solve and correct for those effects are described later in Sec. 1.4.3.

For arrays that are non-coplanar[15] (w is not zero) and have large field-of-view (l and m are not small), a Fourier transform only translates the visibility function $\mathbf{V}_\nu$ on two-dimensions (u, v), therefore w-projection or w-stacking methods are used to determine the full function of intensity, I_ν. The image as seen in the $u - v$ plane is called the “dirty” image, which is the true image of the sky convolved with a dirty beam (i.e. a point spread function). An algorithm called CLEAN has been developed to deconvolve the true image of the sky from the dirty beam (Högbom, 1974). CLEAN works by taking a fraction of flux from the brightest pixel in the image and convolving this with the dirty beam, then subtracting this flux. The remaining image is a residual image with all “true” sources of flux subtracted. The flux that was subtracted is then deconvolved in the final image. Two widely-used software packages that implement the CLEAN algorithm are called CASA Clean (Common Astronomy Software Applications; McMullin et al., 2007) and `WSClean` (Offringa et al., 2014). CASA Clean uses w-projection while `WSClean` uses w-stacking. For the results presented in this thesis in Chapters 2–4, CASA Clean is used to produce final images. The Clean task in CASA can be used with various input parameters. Weighting schemes can be used to bias the sampling of baselines. For example, Natural weighting samples the shorter baselines more than the longer baselines, while Uniform weighting samples all the baselines with the same weight.

---

[15] The Westerbork Synthesis Radio Telescope is an example of an East-West coplanar array.

1.4.2 The LOw Frequency ARray (LOFAR)

Radio interferometry was originally implemented through arrays of radio dishes, which work well for higher frequencies, but venturing further into the low-frequency domain demands more simplistic hardware: dipole antennas. This transition, from dish to dipole, has required the development of totally novel calibration strategies and imaging algorithms. The LOw Frequency ARray began as an international collaboration to build a cost-efficient Phased array, or Aperture array, with an extensive collecting array (van Haarlem et al., 2013). The LOFAR radio telescope is a system of dipole antennas correlated to capture radio emission in the lowest frequency regime (10-240 MHz). The array includes stations located in the Netherlands and in six other European countries. The main stations, in the Netherlands, consist of a compact group of 24 core stations and 14 remote stations. The compact core is made for dense $u - v$ coverage to provide sensitivity to extended emission, while the remote stations, located up to 100 km from the core, increase the array's resolution. Even longer baselines are formed when including the international stations, yielding a radio telescope essentially the size of Northwestern Europe.

A single station consists of 96 low band antennas (LBAs) and 48 high band antennas (HBAs). The LBAs are designed to receive signals ranging from 10-90 MHz while the HBAs receive signals between 110-240 MHz (De Vos et al., 2009). Unlike radio dish antennas, which are pointed toward their target of observation, dipole antennas are stationary and effectively have a full-sky view, so LOFAR stations are steered electronically and this can allow for multiple, simultaneous observations. The field-of-view for an observation is then limited by the station beam(s) or *primary beam*. Each LOFAR station has hardware for pre-processing, housed in a container, where data from the antennas are fed via fiber optic cables. Data is recorded and time-stamped and sent out through an internet connection to the main processing station located in Gröningen, in the Northern part of the Netherlands. Time delays are accounted for to correlate stations for specific observations. Further data processing for DI and DD calibration is carried out with software developed by and for LOFAR users. These software packages and calibration techniques are explained further in Sec. 1.4.3.

The LOFAR Two-meter Sky Survey

One of the main goals of the LOFAR collaboration is to produce full-sky surveys. This is carried out through the Surveys Key Science Project (SKSP). The Multifrequency Snapshot Sky Survey (MSSS; Heald et al., 2015) acted as the testbed for wide-field imaging. The LOFAR Two-metre Sky Survey (LoTSS) is the current ongoing survey to map the full Northern sky over a frequency bandwidth of 120-168 MHz with unprecedented resolution and sensitivity

(Shimwell et al., 2017). In Fig. 1.18, LoTSS is compared to other radio surveys in terms of depth and bandwidth.

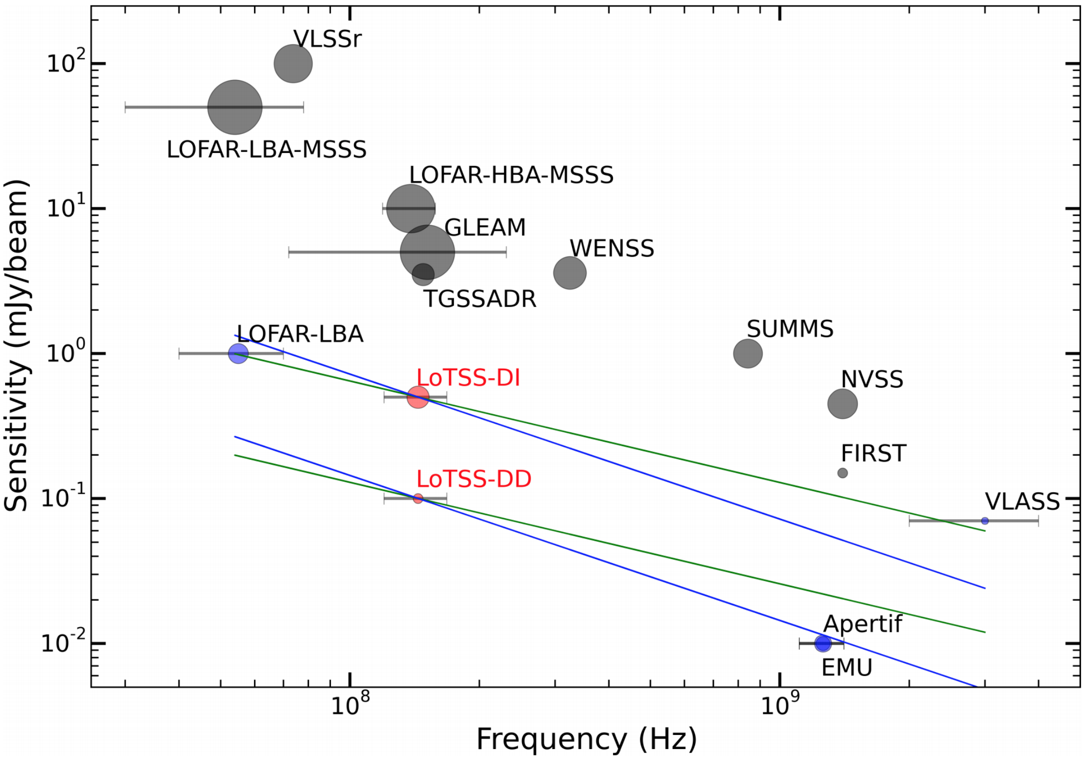

Figure 1.18: This plot shows the sensitivity vs frequency coverage for a sample of ongoing (grey circles) and planned (blue circles) surveys, compared to LoTSS (red circles). The size of the circle is proportional to the square root of the survey's resolution. The horizontal lines show the frequency coverage for surveys with large bandwidths. The green sloping lines show the sensitivity achieved in the LoTSS direction-dependent (DD) calibrated and direction-independent (DI) images for typical radio sources with a spectral index ~ -0.7. The blue sloping lines show the sensitivity to steep spectrum sources with a spectral index ~ -1.0. From Shimwell et al. (2017).

LoTSS utilizes the Dutch HBA antennas only. The survey is being conducted by scheduling 8 hr observations of 3170 separate 5 degree patches of sky called "pointings." The pointing observations are bookended by 10 minute observations of a flux calibrator (typically a 3C source). As of October 2018, about 800 pointings have already been observed. The final images of the survey are of high-fidelity, with a resolution of ~ 5 arcsec and a sensitivity of 100 μJy beam^{-1}.

The science possible with LoTSS is abundant. Survey images are already being used to study AGN up to the highest redshifts ($z \sim 6$), and AGN emission with steep spectra, such as dying, fading, or remnant radio galaxies, that are only detectable at the lowest frequencies. This survey is an excellent probe for studying the steep spectrum radio emission found in galaxy clusters. LoTSS survey images are also used to conduct science on Galactic, extragalactic, and intergalactic magnetic fields, as part of the Magnetism Key Science Project (MKSP; Beck et al., 2013).

The first data release from LoTSS (DR1) is described in Shimwell et al. (2019). The second data release (DR2) is ongoing and is an improvement on DR1. The second data release utilizes highly-tailored calibration and imaging algorithms implemented through software packages called killMS and DDFacet (Tasse et al., 2018). A standardized pipeline, called the DDF pipeline, is currently being used to process pointings and produce science-quality images from LoTSS. The LoTSS data used as part of this thesis was processed and imaged separately from DR1 and DR2, as explained in the next subsection.

1.4.3 Calibration

When observing a specific target, it is necessary to also observe a phase calibrator and a flux calibrator. A nearby phase calibrator is chosen (to correct for DD effects) and typically observed in parallel with the target source. The flux calibrator (used to correct for DI effects) is observed usually at the end and beginning of the observing run, and this calibrator need not be nearby to the target source. The resulting visibility data is stored in a measurement set. Before any data reduction is implemented, the measurement set solely contains a data column which is filled with the raw observational data. After the data scientist makes analyses of the data and “flags” bad or unnecessary data, a calibration will solve antenna *gains* and apply corrections to the raw data and create a new column called the corrected-data column. The calibration depends on a third column called the model-data column. This model column is usually filled with corrected data from a known source. Calibration uses the model data to solve for gains. When observing a source at low radio frequencies, the raw data is subject to distortions from the both the array instrumentation (modeled as $\mathbf{F}$ in Eq. 1.11) and from the ionosphere (modeled as $\mathbf{G}$ in Eq. 1.11). The Jones matrices, $\mathbf{F}$ and $\mathbf{G}$, can be calculated by comparing the true sky (the well known calibrator source) to the distorted sky (raw, uncalibrated, observational data of the same source). In this calibration step, for a fixed direction, $\boldsymbol{s}$, the RIME can be simplified as

$$\mathbf{V}_{\text{cal}} = \mathbf{F}_p \mathbf{G}_p \mathbf{M}_{\text{cal}} \mathbf{G}_q^H \mathbf{F}_q^H \tag{1.15}$$

where $\mathbf{V}_{\text{cal}}$ is the raw data of the calibrator, $\mathbf{M}_{\text{cal}}$ is the model data of the calibrator, and

$\mathbf{F}_p\mathbf{G}_p$ and $\mathbf{F}_q\mathbf{G}_q$ are the gains on antennas p and q, respectively. This equation represents the solution for baseline $p - q$. We do not have access to $\mathbf{F}$ or $\mathbf{G}$ separately, only the product of the two, so we must disentangle them.

Calibration techniques for LOFAR have been developed for a multitude of observation types. For wide-field imaging over several degrees (typically used in surveys), calibration needs to be executed in such a way to solve gains for specific portions of the sky. Survey data undergoes both direction-independent calibration and direction-dependent calibration separately. The survey observations used in this thesis were calibrated using data processing pipelines called Prefactor and FACTOR, corresponding to the Facet Calibration technique from van Weeren et al. (2016b).

1.4.3.1 Direction-Independent Calibration

Prefactor[16] is a package containing automated pipelines called Pre-Facet-Calibration and Initial-Subtract. Pre-Facet-Calibration compresses and averages the original data from 16 TB down to 3 TB and performs the initial direction-independent calibration (see de Gasperin et al., 2019 for details). In this step the bookend-observed flux calibrator, is used to compute amplitude gain solutions, station clock offsets, and station phase offsets. Given $\mathbf{V}$ and holding $\mathbf{G}$ and $\mathbf{X}$ constant, Prefactor solves for $\mathbf{F}$ in Eq. 1.11. Amplitude gain solutions and corrections for clock and phase offsets are then transferred to the target field data, giving $\mathbf{V}_{\text{corr}}$ as in Eq. 1.14. An initial phase calibration is also performed using a global sky model from the TIFR GMRT Sky Survey (TGSS) at 150 MHz (Intema et al., 2017).

1.4.3.2 Direction-Dependent Calibration

Direction-dependent calibration is carried out through the facet calibration technique (van Weeren et al., 2016a), executed via the FACTOR[17] software package. In Eq. 1.11, it is apparent that DD calibration must be computed over the directional integral. The facet calibration technique addresses this by solving gains for a specific direction, $\boldsymbol{s}$. FACTOR tessellates the full target field into several smaller portions of sky called facets, where each facet is automatically chosen to be centered on a bright compact source, or group of sources, to be used as a "facet calibrator." Total electron content (TEC), phase, and amplitude solutions are computed from the facet calibrator and applied to all the sources in that facet. For a single direction, FACTOR goes through several cycles of calibration and imaging. In this case,

---

[16] https://github.com/lofar-astron/prefactor

[17] http://www.astron.nl/citt/facet-doc

FACTOR fixes the direction $\boldsymbol{s}$, and for a fixed $\mathbf{G}$, images $\mathbf{X}$ given $\mathbf{V}_{\text{corr}}$ in Eq. 1.11. Then holding the new model, $\mathbf{X}$, constant, FACTOR solves for $\mathbf{G}$. This process is repeated until the solutions have converged for that facet. FACTOR then proceeds to the next direction. Facets are typically processed in order of brightness, and all facet sources are subtracted from the visibility data before processing the next facet direction. This method reduces the effective noise in the following calibration steps. The target facet, which contains the science target of interest, is usually appointed as the last facet in the processing list, such that all other nearby and bright sources are already calibrated and subtracted. After facets have been calibrated they are imaged with `WSClean`, and these images can be stitched together to create one large mosaic. The last step in FACTOR is to apply a primary beam correction to the mosaic image. For more details on facet calibration the reader is referred to van Weeren et al. (2016a), Shimwell et al. (2016), and Williams et al. (2016).

1.5 Aim and Outline of this Thesis

This thesis is a cumulative work composed of the research I have conducted in the last three years concerning the origins of diffuse radio emission in merging galaxy clusters. As part of my research, I determined whether observational evidence either supports or challenges current models on particle acceleration. I used specialized calibration and imaging techniques designed for LOFAR data to process several LoTSS pointings and make science-quality images of galaxy clusters at 140 MHz. I analyzed these images, and combined them with images from different frequencies/wavelengths, to study the properties of diffuse radio sources in merging galaxy clusters. I specifically focused on studying radio halos, radio relics, and the interaction between extended, bent-tail radio galaxies and the ICM. The following section summarizes the aims of my work and the structure of the results presented in this thesis.

Here are the questions this thesis aims to address:

- With sensitive, low-frequency observations do we find that radio halos and USSRHs are common in merging systems?
- Are radio relics the products of only the strongest merger shocks, or do minor-merger shocks also produce detectable radio relics?
- Is the emission from radio galaxies, BTs, and remnants susceptible to disturbance and re-acceleration by merger-induced turbulence and shocks in the ICM?

- Do extended radio galaxies provide a large quantity of seed electrons for radio halos and relics?
- Can we determine the evolutionary phases of merging clusters based on radio observations?

I have studied diffuse radio sources in five merging galaxy clusters of various masses and redshifts. I have gathered and published my findings in three scientific refereed journal articles, and those papers are inserted as Chapters 2, 3, and 4 in this thesis:

– A. Wilber, M. Brüggen, A. Bonafede, F. Savini, T. Shimwell, R. J. van Weeren, D. Rafferty, A. P. Mechev, H. Intema, F. Andrade-Santos, A. O. Clarke, E. K. Mahony, R. Morganti, I. Prandoni, G. Brunetti, H. Röttgering, S. Mandal, F. de Gasperin, and M. Hoeft. LOFAR discovery of an ultra-steep radio halo and giant head-tail radio galaxy in Abell 1132. MNRAS, 473:3536–3546, January 2018.

– A. Wilber, M. Brüggen, A. Bonafede, D. Rafferty, F. Savini, T. Shimwell, R. J. van Weeren, A. Botteon, R. Cassano, G. Brunetti, F. De Gasperin, D. Wittor, M. Hoeft, and L. Birzan. Search for low-frequency diffuse radio emission around a shock in the massive galaxy cluster MACS J0744.9+3927. MNRAS, 476:3415–3424, May 2018.

– A. Wilber, M. Brüggen, A. Bonafede, and et al. Evolutionary phases of merging clusters as seen by LOFAR. Manuscript to be published in A&A, 2019.

Chapter 2 represents work published in MNRAS by Wilber et al. (2018a). This paper announces the discovery of an ultra-steep spectrum radio halo and a giant radio galaxy in the cluster Abell 1132. Chapter 3 represents work published in MNRAS by Wilber et al. (2018b). This paper describes the search for diffuse radio emission associated with a cluster shock detected by the Sunyaev-Zel'dovich effect. Chapter 4 represents work to be published in A&A by Wilber et al. (2019). This paper hypothesizes the merging status of three separate clusters using radio observations. In Chapter 5 other works for which I am a co-author are summarized and discussed in the context of the results of my first-author papers. Chapter 6 discusses the findings of the works in Chapters 2–5 as a whole, specifically addressing the above motivational questions. The concluding chapter also includes information on unanswered questions in the field and how upcoming radio surveys will help us to answer those questions.

References

Beck R., et al., 2013, Astronomische Nachrichten, 334, 548

Bell A., 1978, Monthly Notices of the Royal Astronomical Society, 182, 147

Best P. N., von der Linden A., Kauffmann G., Heckman T. M., Kaiser C. R., 2007, MNRAS, 379, 894

Blandford R., Eichler D., 1987, Phys. Rep., 154, 1

Blandford R. D., Znajek R. L., 1977, MNRAS, 179, 433

Böhringer H., et al., 2004, A&A, 425, 367

Bonafede A., Feretti L., Murgia M., Govoni F., Giovannini G., Dallacasa D., Dolag K., Taylor G. B., 2010a, A&A, 513, A30

Bonafede A., Feretti L., Murgia M., Govoni F., Giovannini G., Dallacasa D., Dolag K., Taylor G. B., 2010b, A&A, 513, A30

Bonafede A., et al., 2014a, MNRAS, 444, L44

Bonafede A., Intema H., Brüggen M., Girardi M., Nonino M., Kantharia N., Van Weeren R., Röttgering H., 2014b, The Astrophysical Journal, 785, 1

Botteon A., Gastaldello F., Brunetti G., Kale R., 2016, MNRAS, 463, 1534

Bridle A. H., Fomalont E. B., 1976, A&A, 52, 107

Brienza M., et al., 2016, A&A, 585, A29

Brienza M., et al., 2017, A&A, 606, A98

Brüggen M., 2013a, Astronomische Nachrichten, 334, 543

Brüggen M., 2013b, MNRAS, 436, 294

Brunetti G., Jones T. W., 2014, International Journal of Modern Physics D, 23, 1430007

Brunetti G., Setti G., Feretti L., Giovannini G., 2001, MNRAS, 320, 365

Brunetti G., et al., 2008, Nature, 455, 944

Burbidge G., 1956, The Astrophysical Journal, 124, 416

Carilli C. L., Taylor G. B., 2002, ARA&A, 40, 319

Cassano R., 2009, in Saikia D. J., Green D. A., Gupta Y., Venturi T., eds, Astronomical Society of the Pacific Conference Series Vol. 407, The Low-Frequency Radio Universe. p. 223 (`arXiv:0902.2971`)

Cassano R., Brunetti G., Setti G., 2006a, MNRAS, 369, 1577

Cassano R., Brunetti G., Setti G., 2006b, MNRAS, 369, 1577

Cassano R., Brunetti G., Setti G., Govoni F., Dolag K., 2007, MNRAS, 378, 1565

Cassano R., Ettori S., Giacintucci S., Brunetti G., Markevitch M., Venturi T., Gitti M., 2010, ApJ, 721, L82

Cassano R., Brunetti G., Venturi T., 2011, Journal of Astrophysics and Astronomy, 32, 519

Cassano R., et al., 2013, ApJ, 777, 141

Chernyshov D. O., Dogiel V. A., Ko C. M., 2012, ApJ, 759, 113

Condon J. J., Cotton W. D., Greisen E. W., Yin Q. F., Perley R. A., Taylor G. B., Broderick J. J., 1998, AJ, 115, 1693

Cuciti V., Cassano R., Brunetti G., Dallacasa D., Kale R., Ettori S., Venturi T., 2015, A&A, 580, A97

De Vos M., Gunst A. W., Nijboer R., 2009, Proceedings of the IEEE, 97, 1431

Donnert J., Dolag K., Lesch H., Müller E., 2009, MNRAS, 392, 1008

Drury L. O., 1983, Reports on Progress in Physics, 46, 973

Dubner G., Giacani E., 2015, A&ARv, 23, 3

Ensslin T. A., Biermann P. L., Klein U., Kohle S., 1998, A&A, 332, 395

Fanaroff B. L., Riley J. M., 1974, MNRAS, 167, 31P

Feretti L., Giovannini G., Govoni F., Murgia M., 2012, The Astronomy and Astrophysics Review, 20, 1

Fermi E., 1949, Physical Review, 75, 1169

Giacintucci S., 2011, Mem. Soc. Astron. Italiana, 82, 541

Giacintucci S., et al., 2008, A&A, 486, 347

Giovannini G., Feretti L., 2002, in Feretti L., Gioia I. M., Giovannini G., eds, Astrophysics and Space Science Library Vol. 272, Merging Processes in Galaxy Clusters. pp 197–227, doi:10.1007/0-306-48096-4_7

Giovannini G., Tordi M., Feretti L., 1999a, New Astron., 4, 141

Giovannini G., Tordi M., Feretti L., 1999b, New Astronomy, 4, 141

Guo X., Sironi L., Narayan R., 2014, The Astrophysical Journal, 794, 153

Hamaker J. P., Bregman J. D., Sault R. J., 1996, A&AS, 117, 137

Hardcastle M. J., Croston J. H., 2010, MNRAS, 404, 2018

Harris D. E., Miley G. K., 1978, A&AS, 34, 117

Heald G. H., et al., 2015, A&A, 582, A123

Högbom J. A., 1974, A&AS, 15, 417

Intema H. T., Jagannathan P., Mooley K. P., Frail D. A., 2017, A&A, 598, A78

Jaffe W. J., Perola G. C., 1973, A&A, 26, 423

Jansky K. G., 1933, Nature, 132, 66

Johnston-Hollitt M., Pratley L., 2017, preprint, (`arXiv:1706.04930`)

Kaiser C. R., Alexander P., 1999, MNRAS, 302, 515

Kang H., Ryu D., 2015, ApJ, 809, 186

Large M., Mathewson D., Haslam C., 1959

Lin Y.-T., Mohr J. J., 2004, ApJ, 617, 879

Longair M. S., 1966, MNRAS, 133, 421

Madau P., Meiksin A., Rees M. J., 1997, ApJ, 475, 429

Markevitch M., Gonzalez A., Clowe D., Vikhlinin A., Forman W., Jones C., Murray S., Tucker W., 2004, The Astrophysical Journal, 606, 819

McMullin J. P., Waters B., Schiebel D., Young W., Golap K., 2007, in Shaw R. A., Hill F., Bell D. J., eds, Astronomical Society of the Pacific Conference Series Vol. 376, Astronomical Data Analysis Software and Systems XVI. p. 127

McNamara B. R., Nulsen P. E. J., 2007, ARA&A, 45, 117

Melrose D. B., 1980, Plasma astrohysics. Nonthermal processes in diffuse magnetized plasmas - Vol.1: The emission, absorption and transfer of waves in plasmas; Vol.2: Astrophysical applications

Miley G., 1980, ARA&A, 18, 165

Morganti R., 2017, Nature Astronomy, 1, 596

Nuza S. E., Hoeft M., van Weeren R. J., Gottlöber S., Yepes G., 2012, MNRAS, 420, 2006

Offringa A. R., et al., 2014, MNRAS, 444, 606

Ogrean G. A., Brüggen M., 2013, MNRAS, 433, 1701

Ogrean G. A., Brüggen M., van Weeren R., Simionescu A., Röttgering H., Croston J. H., 2011, MNRAS, 414, 1175

Peterson J. R., Fabian A. C., 2006, Physics reports, 427, 1

Petrosian V., 2001, ApJ, 557, 560

Pfrommer C., Enßlin T. A., 2004, A&A, 413, 17

Pinzke A., Oh S. P., Pfrommer C., 2013, MNRAS, 435, 1061

Planck Collaboration et al., 2016, A&A, 594, A13

Porter D. H., Jones T. W., Ryu D., 2015, ApJ, 810, 93

Randall S. W., Markevitch M., Clowe D., Gonzalez A. H., Bradač M., 2008, ApJ, 679, 1173

Rengelink R. B., Tang Y., de Bruyn A. G., Miley G. K., Bremer M. N., Roettgering H. J. A., Bremer M. A. R., 1997, A&AS, 124

Rich J., 2014, Fundamentals of Cosmology. Springer Berlin Heidelberg

Rosswog S., Brüggen M., 2011, Introduction to High-Energy Astrophysics

Ryu D., Kang H., Hallman E., Jones T. W., 2003, ApJ, 593, 599

S. Zimmer for the Fermi-LAT Collaboration 2015, preprint, (`arXiv:1502.02653`)

Santos J. S., Rosati P., Tozzi P., Böhringer H., Ettori S., Bignamini A., 2008, A&A, 483, 35

Sarazin C., 1988, X-Ray Emission from Clusters of Galaxies. Cambridge Astrophysics, Cambridge University Press

Saripalli L., Hunstead R. W., Subrahmanyan R., Boyce E., 2005, AJ, 130, 896

Shimwell T. W., et al., 2016, MNRAS, 459, 277

Shimwell T. W., et al., 2017, A&A, 598, A104

Shimwell T. W., Tasse C., Hardcastle M. J., et al. 2019, A LOFAR study of non-merging massive galaxy clusters, Manuscript accepted for publication in A&A

Spitzer L., 1962, Physics of Fully Ionized Gases

Springel V., Farrar G. R., 2007, Monthly Notices of the Royal Astronomical Society, 380, 911

Springel V., Frenk C. S., White S. D., 2006, Nature, 440, 1137

Stocke J. T., Hart Q. N., Hallman E. J., 2009, in Heinz S., Wilcots E., eds, American Institute of Physics Conference Series Vol. 1201, American Institute of Physics Conference Series. pp 206–209, doi:10.1063/1.3293036

Tasse C., et al., 2018, A&A, 611, A87

Thompson A. R., 1999, in Taylor G. B., Carilli C. L., Perley R. A., eds, Astronomical Society of the Pacific Conference Series Vol. 180, Synthesis Imaging in Radio Astronomy II. p. 11

Vazza F., Eckert D., Brüggen M., Huber B., 2015, Monthly Notices of the Royal Astronomical Society, 451, 2198

Vazza F., Brüggen M., Wittor D., Gheller C., Eckert D., Stubbe M., 2016, MNRAS, 459, 70

Vazza F., Jones T. W., Brüggen M., Brunetti G., Gheller C., Porter D., Ryu D., 2017, MNRAS, 464, 210

Vazza F., Brunetti G., Brüggen M., Bonafede A., 2018, MNRAS, 474, 1672

Venturi T., Giacintucci S., Dallacasa D., Cassano R., Brunetti G., Bardelli S., Setti G., 2008, A&A, 484, 327

Vikhlinin A., Markevitch M., Murray S. S., Jones C., Forman W., Van Speybroeck L., 2005, ApJ, 628, 655

Wilber A., et al., 2018a, MNRAS, 473, 3536

Wilber A., et al., 2018b, MNRAS, 476, 3415

Wilber A., Brüggen M., Bonafede A., et al. 2019, Evolutionary phases of merging clusters as seen by LOFAR, Manuscript accepted for publication in A&A

Williams W. L., et al., 2016, MNRAS, 460, 2385

Willson M. A. G., 1970, MNRAS, 151, 1

Wittor D., Jones T., Vazza F., Brüggen M., 2017, MNRAS, 471, 3212

Yusef-Zadeh F., Morris M., Chance D., 1984, Nature, 310, 557

Zaroubi S., et al., 2012, MNRAS, 425, 2964

de Gasperin F., et al., 2012, Astronomy & Astrophysics, 547, A56

de Gasperin F., et al., 2017, Science Advances

de Gasperin F., Dijkema T. J., Drabent A., et al. 2019, Systematic effects in LOFAR data: a unified LOFAR-LBA and LOFAR-HBA calibration strategy for calibrator fields, Manuscript accepted for publication in A&A

Šuhada R., et al., 2012, A&A, 537, A39

van Haarlem M. P., et al., 2013, A&A, 556, A2

van Weeren R. J., Röttgering H. J. A., Brüggen M., Hoeft M., 2010, Science, 330, 347 van Weeren R. J., Röttgering H. J. A., Intema H. T., Rudnick L., Brüggen M., Hoeft M., Oonk J. B. R., 2012, A&A, 546, A124

van Weeren R. J., et al., 2016a, ApJS, 223, 2

van Weeren R. J., et al., 2016b, ApJ, 818, 204

van Weeren R., et al., 2016c, The Astrophysical Journal, 818, 204

van Weeren R. J., et al., 2017, Nature Astronomy, 1, 0005

van Weeren R. J., de Gasperin F., Akamatsu H., Brüggen M., Kang H., Stroe A., Zandanel F., 2018, Diffuse Radio Emission from Galaxy Clusters, review to be published.

2 LOFAR discovery of an ultra-steep radio halo and giant head-tail radio galaxy in Abell 1132

– Amanda Wilber, Marcus Brüggen, Annalisa Bonafede, Federica Savini, Timothy W. Shimwell, Reinout J. van Weeren, David Rafferty, Alexander P. Mechev, Huib Intema, Felipe Andrade-Santos, Alex O. Clarke, Elizabeth K. Mahony, Raffaella Morganti, Isabella Prandoni, Gianfranco Brunetti, Huub J. A. Röttgering, Soumyajit Mandal, Francesco de Gasperin, Matthias Hoeft –

Monthly Notices of the Royal Astronomical Society, published on 3 October 2017

Abstract

LOFAR observations at 144 MHz have revealed large-scale radio sources in the unrelaxed galaxy cluster Abell 1132. The cluster hosts diffuse radio emission on scales of $\sim$ 650 kpc near the cluster center and a head-tail (HT) radio galaxy, extending up to 1 Mpc, south of the cluster center. The central diffuse radio emission is not seen in NVSS, FIRST, WENSS, nor in C & D array VLA observations at 1.4 GHz, but is detected in our follow-up GMRT observations at 325 MHz. Using LOFAR and GMRT data, we determine the spectral index of the central diffuse emission to be $\alpha = -1.75 \pm 0.19$ ($S \propto \nu^{\alpha}$). We classify this emission as an ultra-steep spectrum radio halo and discuss the possible implications for the physical origin of radio halos. The HT radio galaxy shows narrow, collimated emission extending up to 1 Mpc and another 300 kpc of more diffuse, disturbed emission, giving a full projected linear size of 1.3 Mpc – classifying it as a giant radio galaxy (GRG) and making it the longest HT found to date. The head of the GRG coincides with an elliptical galaxy (SDSS J105851.01+564308.5) belonging to Abell 1132. In our LOFAR image, there appears to be a connection between the radio halo and the GRG. The turbulence that may have produced the halo may have also affected the tail of the GRG. In turn, the GRG may have provided seed electrons for the radio halo.

2.1 Introduction

Cluster-scale diffuse radio emission, in the form of radio halos and radio relics, indicates the presence of large-scale magnetic fields and relativistic electrons within the intracluster medium (ICM). During a cluster merger, turbulence and shocks are produced in the ICM (e.g. Vazza et al., 2009) and can lead to the re-acceleration of mildly-relativistic ICM electrons to ultra-relativistic speeds. The ultra-relativistic electrons (Lorentz factor $\gamma \gg 1000$) then interact with the ICM B-field (on the order of a few μG) to produce synchrotron emission in the radio regime, and can lead to the formation of large-scale radio sources called halos and relics (e.g. Kempner et al., 2004; see Feretti et al., 2012 for review). The origin of radio halos and relics involves complex mechanisms, and further investigation is needed to understand how these mechanisms affect the physics of the ICM (see Brunetti & Jones, 2014 for review).

Radio halos are classified as diffuse radio emitters that fill the central regions of galaxy clusters, and are found to coincide with the thermal gas seen in X-ray observations. These radio structures are vast in size, usually extending up to 1 Mpc, and are typically characterised by a steep spectrum ($\alpha \lesssim -1$)[1] and low surface brightness (~ 1 μJy arcsec^{-2} at 1.4 GHz; e.g Feretti et al., 2012). Two main models have been proposed for the origins of radio halos: the hadronic model and the turbulent re-acceleration model. The hadronic model states that collisions between cosmic-ray protons and thermal protons in the ICM would continuously produce the secondary electrons needed to generate radio halo emission at the cluster center (Dennison, 1980; Blasi & Colafrancesco, 1999; Enßlin et al., 2011). Hadronic collisions should also produce secondary gamma-ray photons, but the non-detection of galaxy clusters in the gamma-ray regime has constrained the contribution from secondary electrons to be subdominant (e.g. Ackermann et al., 2010, 2016; Jeltema & Profumo, 2011; Brunetti et al., 2012). The turbulent re-acceleration model states that mildy-relativistic ICM electrons are re-accelerated to ultra-relativistic energies *in situ* during a cluster-sub-cluster merger (Brunetti et al., 2001; Petrosian, 2001).

Cluster mergers are thought to produce turbulence that can accelerate cosmic rays and may amplify the magnetic fields in the ICM via the small-scale dynamo (Vazza et al., 2017; Keshet et al., 2010; Ryu et al., 2008; Miniati & Beresnyak, 2016). Indeed, studies that combine radio and X-ray data of galaxy clusters have suggested a causal link between merging activity of clusters and the occurrence of radio halos (e.g. Cassano et al., 2013). Currently, turbulent re-acceleration is the favoured scenario for the origin of radio halos, although several questions remain in identifying the seed source of mildy-relativistic electrons within the ICM

---

[1] We define the spectral index, α, where $S \propto \nu^{\alpha}$.

and in understanding the physics of cluster shocks and shock-induced turbulence. There are also a few outliers, where giant radio halos are found in cool-core, non-merging clusters (e.g. Bonafede et al., 2014; Sommer et al., 2017), that challenge our present interpretation of ICM acceleration mechanisms.

A unique prediction of turbulent re-acceleration models is the existence of a large number of radio halos with very steep spectra (Cassano et al., 2006; Brunetti et al., 2008). Steep-spectrum halos are produced when the turbulent re-acceleration rate is not efficient enough to accelerate electrons emitting at GHz frequencies, or during late evolutionary stages when turbulence is dissipated in the ICM (e.g. Cassano et al., 2012; Donnert et al., 2013). Searching for fading ultra-steep spectrum halos may assist in clarifying the physical origins of radio halos: the identification of breaks in the spectrum of halos can be used to infer the efficiency of the mechanism that produces the emitting cosmic-ray electrons (Thierbach et al., 2003; Donnert et al., 2010a,b). A few cases of ultra-steep spectrum halos have been found (e.g. Brunetti et al., 2008; Macario et al., 2013; Bonafede et al., 2012), but further sensitive low-frequency observations may be needed to reveal the population of ultra-steep halos.

Active galactic nuclei (AGN) injection from individual cluster radio galaxies is one explanation for the large supply of mildly-relativistic seed electrons needed for the turbulent re-acceleration that produces cluster-scale radio emission (such a connection has been established for certain cluster radio relics, as for example in van Weeren et al., 2017). Giant radio galaxies (GRGs), which are generally defined as radio galaxies with a linear projected size of $\gtrsim 0.7$ Mpc (e.g. Saripalli et al., 2005), can have a significant influence on their surrounding medium by supplying a large quantity of cosmic rays. Different scenarios may explain the formation and large extent of GRGs: the AGN may have been active for a very long time, the jets may be powerful enough to push emission out to large distances without much deterrence from the surrounding medium, and/or the surrounding medium could be much less dense as compared to the medium around typical radio galaxies (Kaiser & Alexander, 1999).

Tailed and bent-tailed radio galaxies are often found within the rich environments of galaxy clusters, and their jets give an indication of where cosmic-ray electrons are being injected into the surrounding medium. These tailed sources have been typically categorized by their morphologies as seen in projection: as wide-angle-tail (WAT) when two radio jets, or plumes, are distinguishable, collimated, and open at an angle of $\lesssim 60°$, or narrow-angle-tail (NAT) when the radio jets open in a very small angle such that they appear aligned on one side of the host galaxy or conjoined as a single tail (also referred to as head-tail (HT) radio galaxies) (e.g. Dehghan et al., 2014). It is generally thought that bent-tailed galaxies form when the jets experience ram pressure as the host galaxy moves through the ICM. A host galaxy traveling at high velocity may experience a ram pressure shock that aligns both radio jets behind the host's trajectory, leaving the radio source with a perceived NAT/HT morphology (Miley, 1980). Of the known bent-tailed radio galaxies, only a small percentage are also GRGs. The longest HT discovered so far is in Abell 1314 with a projected linear size of 700 kpc (Srivastava & Singal, 2016).

Abell 1132

Abell 1132 is a massive cluster ($5.87^{+0.22}_{-0.23} \times 10^{14}$ $M_{\odot}$ from the Planck Collaboration et al., 2014) that shows signs of merging (Cuciti et al., 2015), but has not shown diffuse radio emission in past VLA observations at 1.4 GHz (Giovannini & Feretti, 2000). Abell 1132 is centred at R.A., decl. 10h58m25.8s, $+56°47'30''$ (equatorial, J2000.0) and located at a redshift of $z = 0.1369$ (Struble & Rood, 1999). It contains several Fanaroff-Riley (FR) type-I radio galaxies (O'Dea & Owen, 1985), was covered by the NRAO VLA Sky Survey (NVSS; Condon et al., 1998), and has been observed by the Chandra X-ray Observatory.

Rudnick & Lemmerman (2009) reported an extended head-tail source, 370 kpc long, about $6'$ south of the cluster center using reprocessed data from the Westerbork Northern Sky Survey (WENSS; Rengelink et al., 1997). They noted that the head of this source is visible in NVSS and coincides with an elliptical galaxy[2] belonging to the cluster.

In this paper, we report on Low-Frequency Array (LOFAR) observations and follow-up Giant Meterwave Radio Telescope (GMRT) observations of the galaxy cluster Abell 1132 and newly discovered extended radio emission. In the following section, details of our observations, data calibration, and imaging techniques are described. In Sec. 2.3 we show our LOFAR and GMRT images of the radio emission seen in Abell 1132, and in Sec. 2.4 we discuss how these images provide clues as to the morphology and possible origins of the detected emission. The scale at Abell 1132's redshift is 2.439 kpc''^{-1} with the cosmological parameters $H_0 = 69.6$, $\Omega_m = 0.286$, and $\Omega_\Lambda = 0.714$, adopted hereafter.

---

[2] mR = 16.78 galaxy in SDSS (R.A., decl. = 10h58m50.96s, $+56°43'08''$), with a redshift of $z = 0.138954 \pm 0.000162$.

2.2 Methods

2.2.1 LoTSS

LOFAR is a low-frequency radio interferometer based in the Netherlands with additional international stations throughout Europe (van Haarlem et al., 2013). The array includes low-band and high-band antennae (LBA and HBA) that receive signals over a frequency range of 10-90 MHz and 120-240 MHz, respectively. LOFAR's large field-of-view, compact core, and its high sensitivity at low frequencies makes it the ideal instrument to study steep spectrum diffuse radio emission in galaxy clusters as well as giant radio galaxies with large angular diameter and low surface brightness.

The LOFAR Two-meter Sky Survey (LoTSS) (Shimwell et al., 2017) Tier-1 has currently observed 14% of the northern sky at 120 -168 MHz (as of July 2017) with one of its main science goals to study galaxy clusters and search for cluster-scale radio emission. With a depth of $\sim 100\ \mu$Jy beam^{-1} at a resolution of $\sim 5''$, this survey is particularly sensitive to steep spectrum radio emission, and thanks to the compact core of LOFAR it can detect radio objects with low surface brightness (see Shimwell et al., 2016, 2017, for details).

The observation of Abell 1132 was part of a standard Tier-1 survey observation, covering an area of ~ 19 deg^2 centered on R.A., decl. 11h00m20s, $+57°11'48''$, made with the LOFAR Dutch HBA array[3]. The north-western region of this field overlaps the Lockman hole (a region of space that has a low column density of hydrogen) which was also covered by LoTSS. Although Abell 1132 is visible in those observations (see Mahony et al., 2016 and Brienza et al., 2017 for details), here we provide a more detailed analysis of the radio emission seen in Abell 1132 with our more recent and more sensitive Tier-1 observation centered on Abell 1132. Our survey field was observed for 8 h to ensure sufficient *uv* coverage. The observation covers a total bandwidth of 48 MHz with a central frequency of 144 MHz. See Table 3.1 for observation details.

2.2.2 LOFAR data reduction

The standard data reduction for LoTSS data can be summarized into the following steps:

- Pre Facet Calibration via Prefactor[4]: Computes direction-independent solutions from

---

[3] The Dutch array consists of 24 core and 14 remote stations in the Netherlands.

[4] https://github.com/lofar-astron/prefactor

Table 2.1: Radio observations of A1132.

Telescope	LOFAR	GMRT
Observation ID	544905	9101 / 9104
Pointing center (RA,DEC: J2000)	11h00m20s, +57°11′48″	10h58m25.8s +56°47′30″
Observation date	2016 Sep 6	2016 Dec 30 / 31
Total on-source time	8 h	8 h
Flux calibrator	3C196	3C147 & 3C286
Total on-calibrator time	10 min	20 min
Central frequency	144 MHz	325 MHz / 610 MHz
Bandwidth	48 MHz	16 MHz / 32 MHz

observation of a standard calibrator and transfers these solutions to the target data. Performs an initial phase calibration for the target data using a global sky model. Produces preliminary images of the full field of view.

- Facet Calibration via FACTOR[5] (van Weeren et al., 2016): Performs direction-dependent calibration in multiple directions over the full bandwidth of target data. Corrects for ionospheric disturbances and beam errors. Produces high-resolution images.

In the following subsections, these steps will be elaborated upon for this particular observation.

2.2.2.1 Pre Facet Calibration

The calibrator chosen for this observation was 3C196, a bright quasar (74 Jy according to the Scaife & Heald (2012) absolute flux scale). The Prefactor pipeline was used to compute the amplitude gains, station clock offsets, station phase correlation offsets, and station differential total electron content (dTEC) from the standard calibrator data and apply all direction-independent solutions to the target data[6]. After direction-independent solutions were transferred, an initial phase calibration was performed on the target field using a global sky model produced from the VLA Low-Frequency Sky Survey (VLSSr; Lane et al., 2012), WENSS (Rengelink et al., 1997), and NVSS (Condon et al., 1998). Data from the station CS030HBA were discarded (flagged) because it was not operational for most of the observation.

The Initial-Subtract step, as part of the Pre Facet Calibration pipeline, imaged the direction-independent calibrated target data in both high and low resolution using `WSClean` (Offringa

---

[5] https://github.com/lofar-astron/factor

[6] dTEC solutions from the calibrator were not transferred to the target data since they correspond to the ionosphere and are therefore direction-dependent.

et al., 2014). The pipeline first created an image at a resolution of $\sim 36'' \times 27''$ and automatically detected and masked sources using the source detection software PYBDSF[7]. The clean components of the masked sources were subtracted from the *uv*-data. Then an image was created at a resolution of $\sim 120'' \times 100''$ where more extended sources were revealed, masked, and also subtracted. The final result was a sky model with all high-resolution (compact sources) and low-resolution sources (extended sources) subtracted and a source-subtracted *uv*-dataset, which was then used for direction-dependent calibration.

2.2.2.2 Facet Calibration

Facet Calibration is a direction-dependent calibration method for LOFAR, implemented by the FACTOR[8] package (van Weeren et al., 2016). The first step is to tesselate the full field into multiple facets. Each facet must have its own calibrator, designated by a square region within the facet. The calibrator region is chosen by default to be centered on a compact source at least 0.3 Jy in flux density. The calibration region can be modified by the user to include multiple sources (increasing the calibrator flux density) and/or to include extended emission. To accurately calibrate a typical LoTSS widefield, up to 50 facet directions may be needed.

A process of self-calibration is conducted within the calibration region per facet, where several phase only and phase + amplitude self-calibration cycles are performed until there is convergence. The self-calibration solutions of a given calibrator region are then applied to its full facet, and the facet is imaged using `WSClean`. Each subsequent facet is imaged where all sources from prior facets are subtracted. Typically, facets are processed in order of calibrator brightness; this gradually decreases the effective noise in the *uv*-data. Facet images can be stitched together and primary-beam-corrected for a mosaic image of the full target field. For more details on Facet Calibration the reader is referred to van Weeren et al. (2016), Shimwell et al. (2016), and Williams et al. (2016).

FACTOR was run on the full 48 MHz bandwidth for our observation. A total of 39 directions were designated and 15 bright and nearby facets were processed before processing the target facet containing the cluster Abell 1132. Initially our target calibration region included Abell 1132's complex cluster center. The calibration in this region was inadequate since emission was being displaced and creating bright and negative artifacts. We decided instead to use the calibration solutions from the nearest facet, $\sim 0.25°$ east of Abell 1132's center. The final

---

[7] http://www.astron.nl/citt/pybdsf

[8] http://www.astron.nl/citt/facet-doc

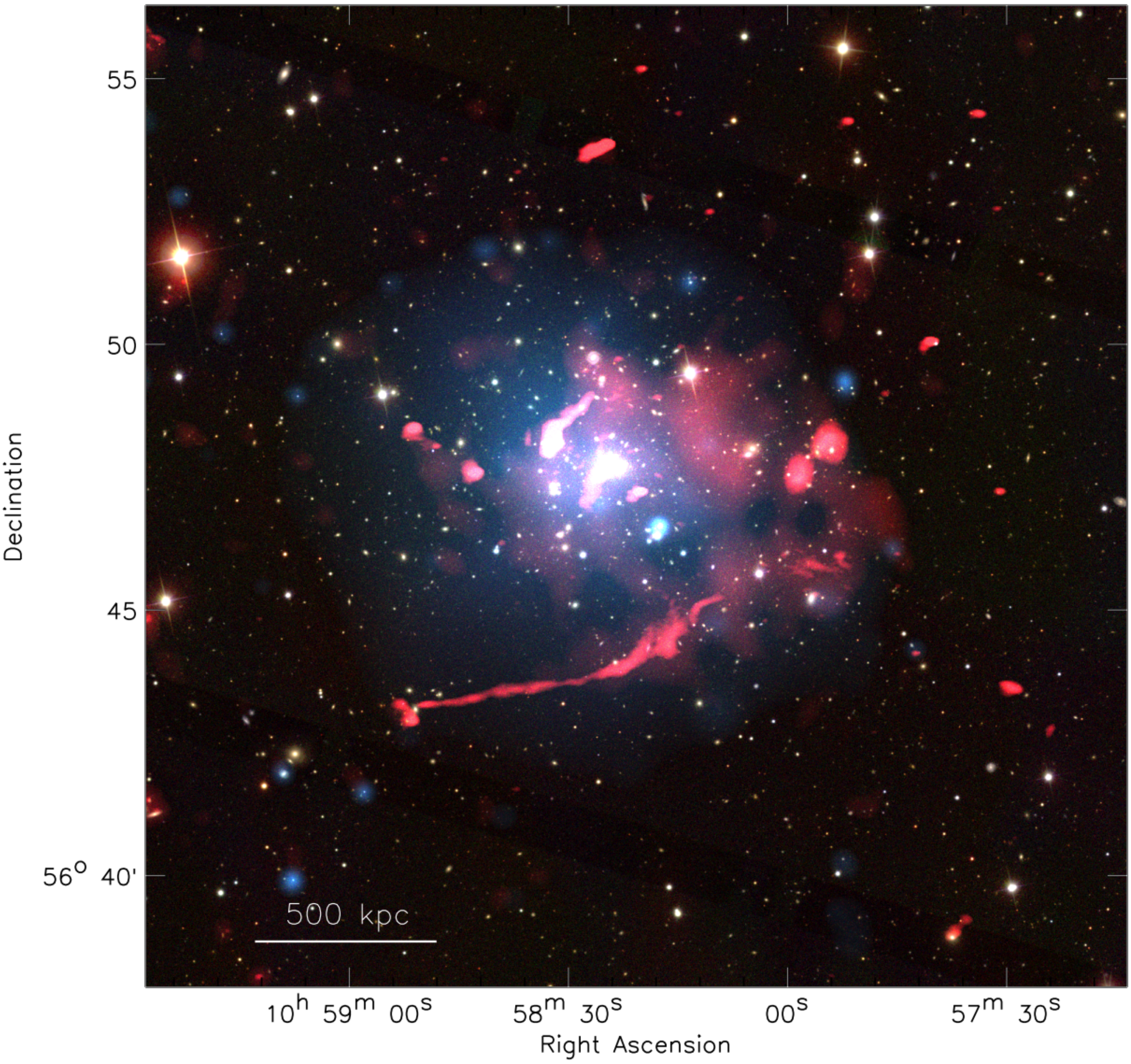

Figure 2.1: Overview image of Abell 1132: LOFAR high-resolution and low-resolution emission are both shown in red. LOFAR high-resolution emission is imaged with a beam size of $\sim 8'' \times 5''$ and RMS noise of 120 μJy beam^{-1}. LOFAR low-resolution diffuse emission (imaged after performing a subtraction of compact sources, as explained in Sec. 2.3.1) is imaged with a beam size of $\sim 30'' \times 26''$ and RMS noise of 350 μJy beam^{-1}. Chandra X-ray emission is in blue. Radio and X-ray emission are overlaid on optical SDSS *g, r, i* images. Diffuse radio emission is present near the center of the cluster, as well as in the length of the southern HT GRG. The central diffuse radio emission, characteristic of a radio halo, is offset from the center of the X-ray emission by $\sim$ 200 kpc. There also appears to be a connection between the radio halo and the diffuse radio emission of the GRG tail.

image produced by FACTOR using `WSClean` has a beam size of $\sim 8'' \times 5''$ with root mean square (RMS) noise of $\sigma \approx 120\ \mu$Jy beam^{-1}.

The FACTOR-calibrated data were also imaged outside of FACTOR using CASA (Common Astronomy Software Applications; McMullin et al., 2007) tools. CASA `CLEAN` was used with various adjusted parameters (uv-taper and Briggs' robust[9] weighting schemes) so that diffuse emission would be properly masked and deconvolved. An increased outer uv-taper was used to bring out diffuse emission at lower resolutions.

2.2.3 Chandra X-ray data reduction

Abell 1132 was observed with the Chandra ACIS-I (ObsID: 13376) in Aug 2011 for 8 ks. We processed the Chandra data following Vikhlinin et al., 2005[10]. This processing includes filtering of periods with elevated background by examining the light curves in the 6–12 keV band, the application of gain maps to calibrate photon energies, and corrections for the position-dependent charge transfer inefficiency. For the final exposure corrected image we used a pixel binning of 4 ($2''$pixel^{-1}). The instrumental and sky background were subtracted. For more details the reader is referred to Vikhlinin et al. (2005).

To obtain the global temperature and luminosity within R_{500} we fitted the spectrum in `XSPEC` (v12.9, Arnaud, 1996), extracting counts in the 0.7–7.0 keV band. For R_{500} we took a value 1.218 Mpc, derived from the mass of 5.9×10^{14} M$_{\odot}$ (Planck Collaboration et al., 2014). Compact sources were excluded from the fitting. The abundance was fixed to 0.3 Z$_{\odot}$ (from the abundance table of Anders & Grevesse, 1989) and the redshift at $z = 0.1366$. The hydrogen column density, N$_{\rm H}$, was fixed to 6.29×10^{19}cm^{-2}, adopting the galactic value (atomic + molecular) from Willingale et al. (2013).

From the `XSPEC` fitting we determine a global temperature of $7.85^{+0.46}_{-0.46}$ keV and a luminosity of $(4.4 \pm 0.1) \times 10^{44}$ erg s^{-1} in the 0.1–2.4 keV energy band and $(2.7 \pm 0.1) \times 10^{44}$ erg s^{-1} in the 0.5–2.0 keV energy band. The bolometric luminosity is $(10.6 \pm 0.3) \times 10^{44}$ erg s^{-1}.

Abell 1132 is an unrelaxed, merging cluster according to its disturbed X-ray morphology revealed by Chandra, and it is one of the few merging systems belonging to samples of massive clusters without diffuse radio emission seen at higher frequencies (Cuciti et al., 2015). Given

---

[9] http://www.aoc.nrao.edu/dissertations/dbriggs

[10] We used CIAO v4.6 and CALDB v4.7.2.

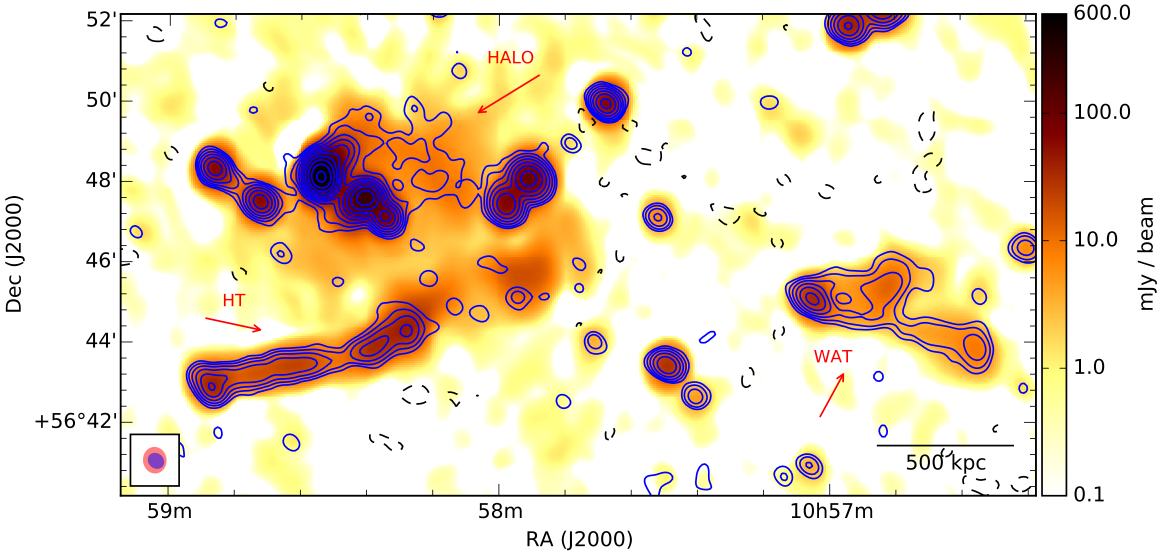

Figure 2.2: Abell 1132: 144 MHz LOFAR low-resolution emission is shown in color (on a logarithmic scale) with 325 MHz GMRT low-resolution contours overlaid in blue. LOFAR and GMRT emission are imaged in CASA `CLEAN` with *uv*-taper 25″ and Briggs' robust 0, with respective RMS noise of 400 μJy beam^{-1} and 220 μJy beam^{-1}. Contours are $\sigma \times [-2, 2, 4, 8, 16, 32, 128, 256, 512, 1024]$. Beam size is designated by the red (LOFAR $\sim 40'' \times 35''$) and blue (GMRT $\sim 26'' \times 22''$) ellipses. Diffuse emission is present near the cluster center as well as in the westward portion of the giant HT. A WAT is visible $\sim 0.2°$ (1.8 Mpc) west of the cluster center.

the $L_1 - T_1$ relation (BCES (Y|X) fitting) in Table 2 of Pratt et al. (2009), the global temperature we measure ($7.85^{+0.46}_{-0.46}$ keV) would correspond to a luminosity of $(2.2 \pm 0.1) \times 10^{45}$ erg s^{-1} in the 0.1–2.4 keV energy band. This is an order of magnitude higher than our measured luminosity, thus fitting into the evidence that suggests this cluster is a merger.

2.2.4 GMRT data reduction

Follow-up GMRT observations of Abell 1132 at 325 MHz and 610 MHz were performed on December 30, and 31, 2016 (see Table 3.1 for observation details). The GMRT data were processed using the SPAM pipeline (see Intema et al., 2017, for details). Our images with the highest resolution and lowest noise were produced in AIPS (Astronomical Image Processing System; Wells, 1985). These data were also imaged with CASA `CLEAN` interactively with various adjusted parameters so that diffuse emission would be properly masked and deconvolved.

2.3 Results

Observations of Abell 1132, as part of LoTSS Tier-1 (Shimwell et al., 2017), reveal several previously unknown regions of radio emission associated with the cluster. In Fig. 2.1 we present our overview image of Abell 1132 where LOFAR radio emission in high- and low-resolution and Chandra X-ray emission are overlaid on an optical image from the Sloan Digital Sky Survey (SDSS). The cluster hosts diffuse radio emission near the cluster center, slightly offset from the X-ray emission, and a giant HT/NAT radio galaxy south of the cluster center with collimated emission to the east and diffuse emission to the west. A WAT radio galaxy, lying $\sim 0.2^\circ$ (1.8 Mpc) west of the cluster center, is also visible in our LoTSS observation (as shown in Fig. 2.2). Follow-up GMRT observations also show a significant portion of the HT radio galaxy and the full WAT radio galaxy at 325 and 610 MHz (see Fig. 2.3). The heads of the two tailed radio galaxies coincide with elliptical galaxies belonging to the cluster: SDSS J105851.01+564308.5 at $z \approx 0.139$ (HT) and SDSS J105702.79+564503.1 at $z \approx 0.136$ (WAT) (see Fig. 2.4; redshifts taken from the Sloan Digital Sky Survey Data Release 2 from Abazajian et al., 2004).

2.3.1 Radio Halo Emission in Abell 1132

Cluster-scale diffuse emission, characteristic of a radio halo, is visible in both the LOFAR image at 144 MHz and the GMRT image at 325 MHz of Abell 1132. Fig. 2.2 shows our low-resolution LOFAR image with our low-resolution GMRT 325 MHz image contours overlaid. In Fig. 2.2 the halo appears more extensive in the LOFAR image, extending toward and possibly connecting to the diffuse emission of the giant southern HT galaxy.

As seen in Fig. 2.2, there are several bright and extended FRI galaxies near the cluster center. We performed a compact-source-subtraction on our 144 and 325 MHz data to better image the diffuse emission and eliminate contamination from the central radio galaxies. Since the halo is detected as diffuse emission on the scale of $\sim 500 - 700$ kpc, we subtracted compact sources corresponding to emission spanning less than 500 kpc. At Abell 1132's redshift, this corresponds to visibility data greater than 1000λ in the uv-plane. We made an image in CASA `CLEAN` with a uv-cut below 1000λ and an outer uv-taper of $10''$, and subtracted the model component from the uv-data using CASA tools `FT`[11] and `UVSUB`. We then re-imaged the source-subtracted datasets with their full uv-range[12] to bring out extended emission (see Fig. 2.6: Left). The residual emission from the central galaxies is $< 1\%$ of their flux densities.

---

[11] We used our own CASA task called `FTW` which includes the widefield w-projection parameter.

[12] $> 80\lambda$ for 144 MHz and $> 100\lambda$ for 325 MHz

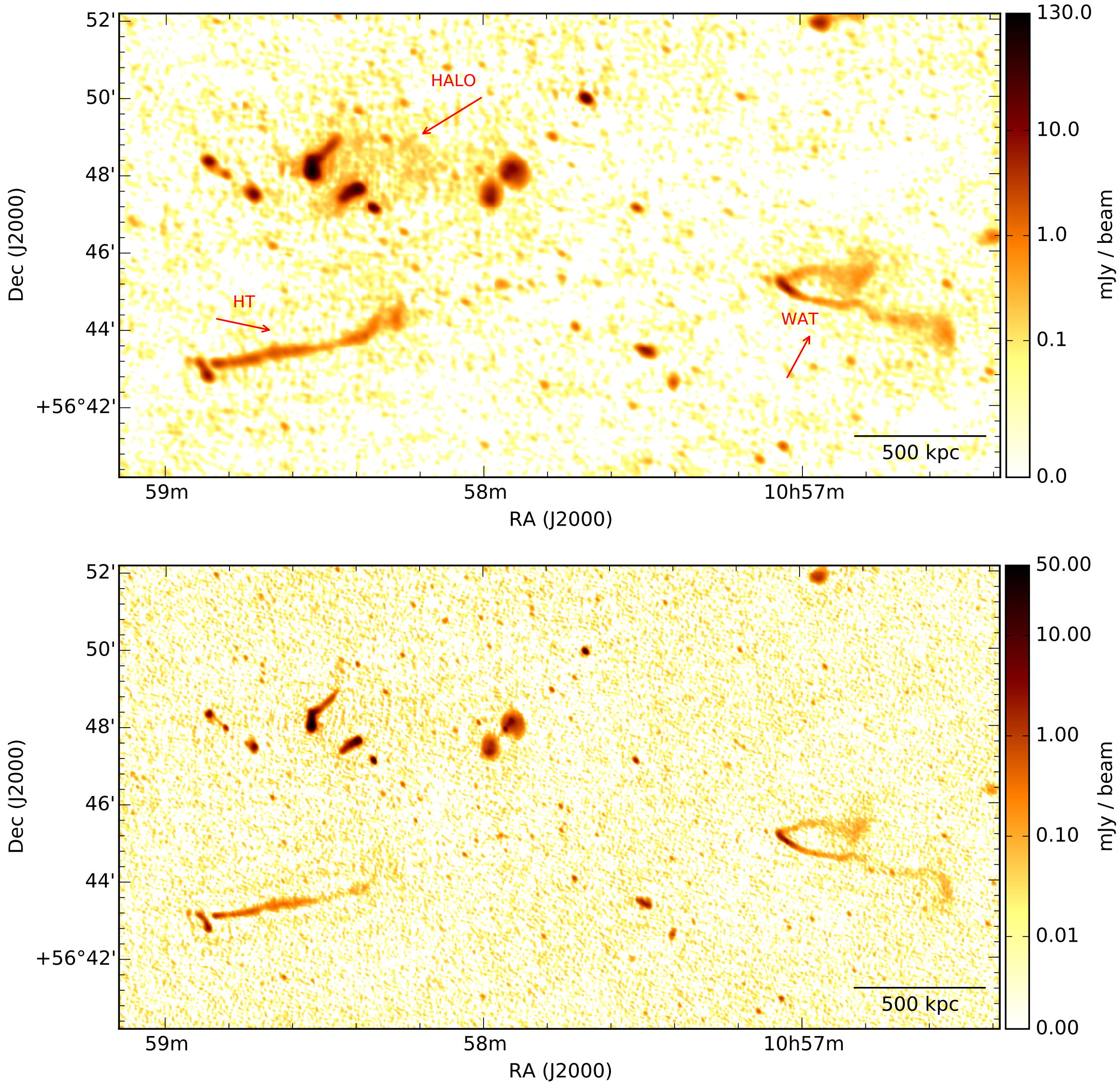

Figure 2.3: Top: GMRT image at 325 MHz with a resolution of $\sim 10'' \times 7''$ and RMS noise of $\sigma \approx 45$ μJy beam^{-1}. Bottom: GMRT image at 610 MHz with a resolution of $\sim 6'' \times 4''$ and RMS noise of $\sigma \approx 20$ μJy beam^{-1}. GMRT data was calibrated via the SPAM pipeline and imaged in AIPS with Briggs' robust -1. Both GMRT images show a significant portion of the HT radio galaxy and the full WAT radio galaxy. The radio halo is partially visible at 325 MHz.

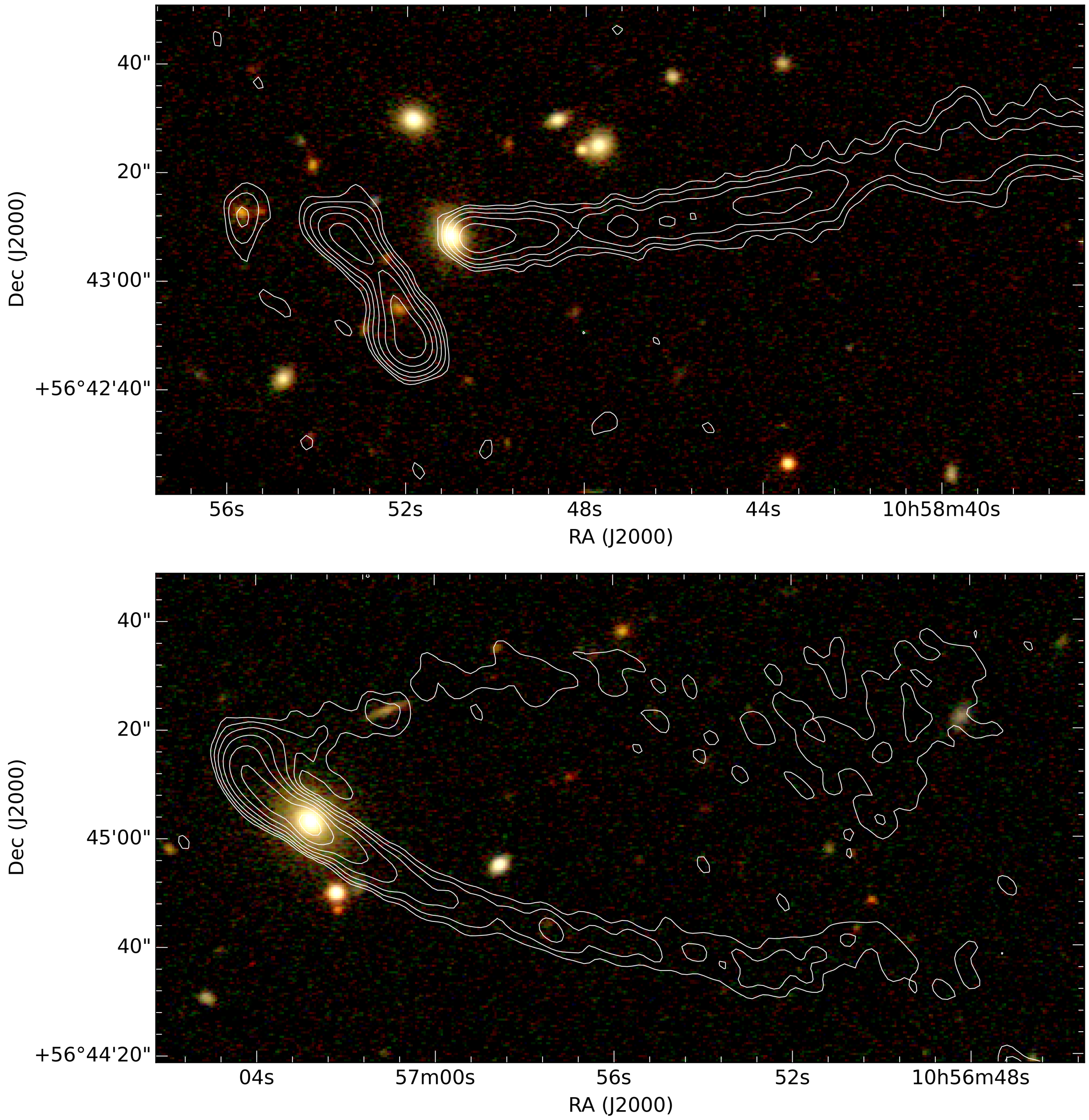

Figure 2.4: SDDS g, r, i optical images overlaid with GMRT contours at 610 MHz. The levels are $[3, 6, 12, 24, 48, 96] \times \sigma$ where $\sigma = 20$ μJy beam^{-1}. Top: the optical source associated with the HT GRG is the elliptical galaxy SDSS J105851.01+564308.5 at a redshift of $z \approx 0.139$, within Abell 1132. The double source to the east of the HT is likely associated with the background galaxy SDSS J105852.18+564255.3 at a redshift of $z \approx 0.496$. Bottom: the optical source associated with the WAT is the elliptical galaxy SDSS J105702.79+564503.1 at a redshift of $z \approx 0.136$, within Abell 1132.

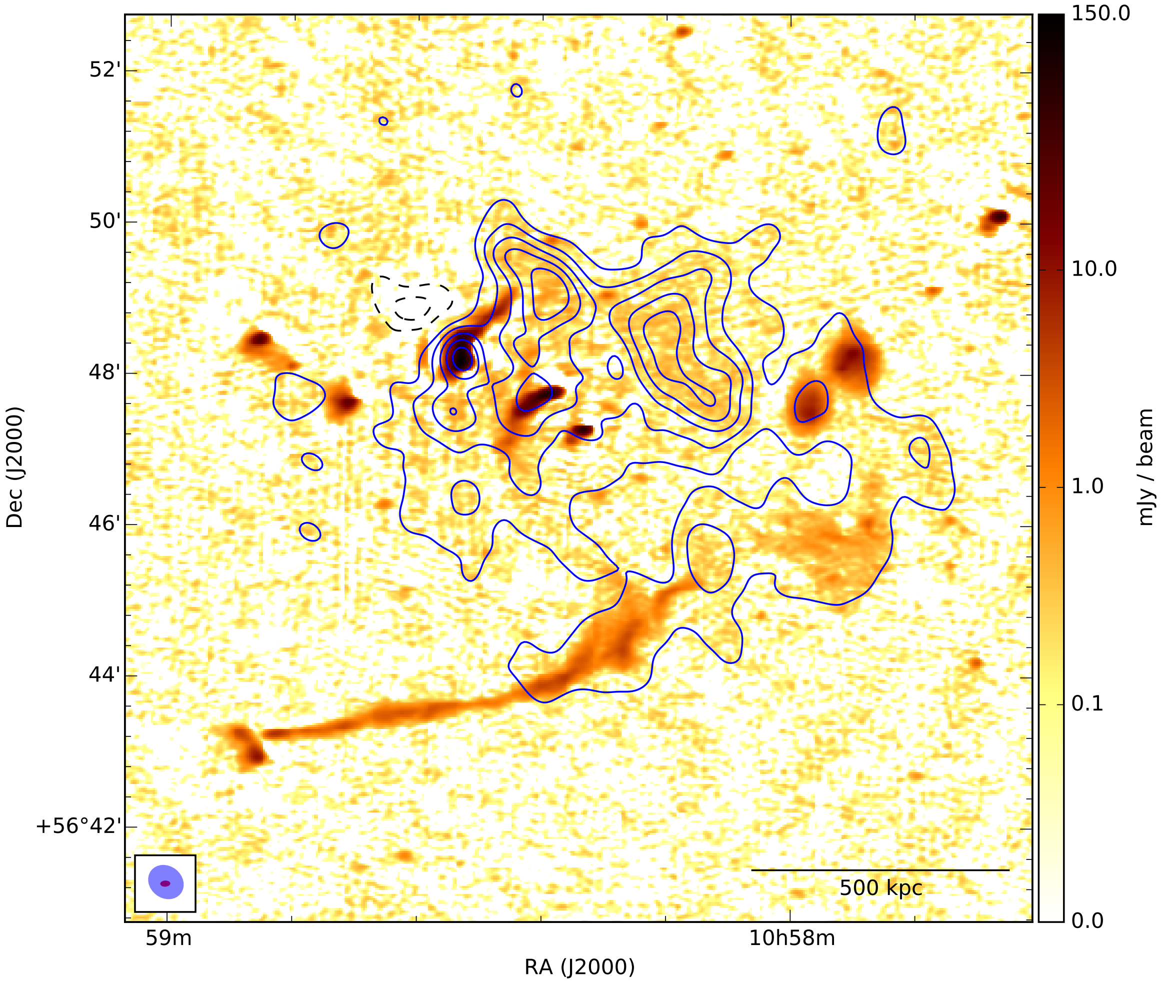

Figure 2.5: Our FACTOR image: LOFAR high-resolution emission is shown in color (on a logarithmic scale), imaged with a beam size of $\sim 8'' \times 5''$ and RMS noise of 120 μJy beam^{-1}, with LOFAR low-resolution diffuse emission contours overlaid in blue. LOFAR diffuse emission is imaged in CASA `CLEAN` with an outer *uv*-taper of 20$''$ and Briggs' robust 0 after subtracting compact sources imaged above a *uv*-range of 1000λ (as explained in Sec. 2.3.1). RMS noise of LOFAR low-resolution diffuse emission is $\sigma = 350\mu$Jy beam^{-1} and the contour levels are $[-6, -3, 3, 6, 9, 12, 15] \times \sigma$. Beam size is designated by the red (high-resolution $\sim 8'' \times 5''$) and blue (low-resolution $\sim 30'' \times 26''$) ellipses.

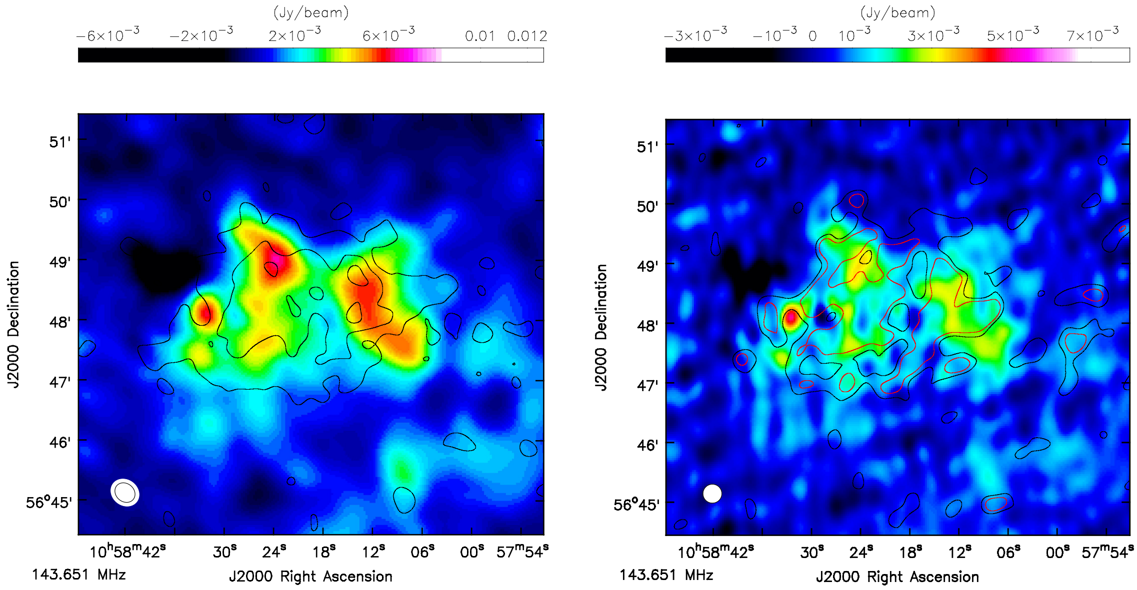

Figure 2.6: LOFAR low-resolution diffuse emission after subtraction of compact sources (as explained in Sec. 2.3.1) is shown in color and GMRT 325 MHz low-resolution diffuse emission after subtraction of compact sources is show as contours overlaid. Left: Our optimal image of the diffuse component in Abell 1132. Both LOFAR and GMRT compact-source-subtracted datasets were imaged in CASA `CLEAN` with an outer uv-taper of 20$''$and Briggs' robust 0. Contours represent $[3, 6, 9] \times \sigma$ at 325 MHz where $\sigma = 75$ μJy beam^{-1}. Right: Our uniform-weighted image of the diffuse emission in Abell 1132. Both LOFAR and GMRT compact-source-subtracted datasets were imaged in CASA `CLEAN` with the same minimum uv-range (100λ), same outer uv-taper ($20''$), and uniform weighting, and were re-gridded and smoothed to the same beam ($19''$). Black contours represent 2σ and red contours represent 3σ at 325 MHz where $\sigma = 130$ μJy beam^{-1}. The spectral index estimates stated in Sec. 2.3.1 were calculated by comparing the measured flux density within the 2σ and 3σ regions at 325 MHz. The red 3σ contours at 325 MHz define an east and west region of the halo, where separate measurements were taken. The final estimate for the spectral index is an average of the values calculated within the 2σ region and the two 3σ regions. The residual flux of the brightest cluster galaxy was not included as measured flux in these regions.

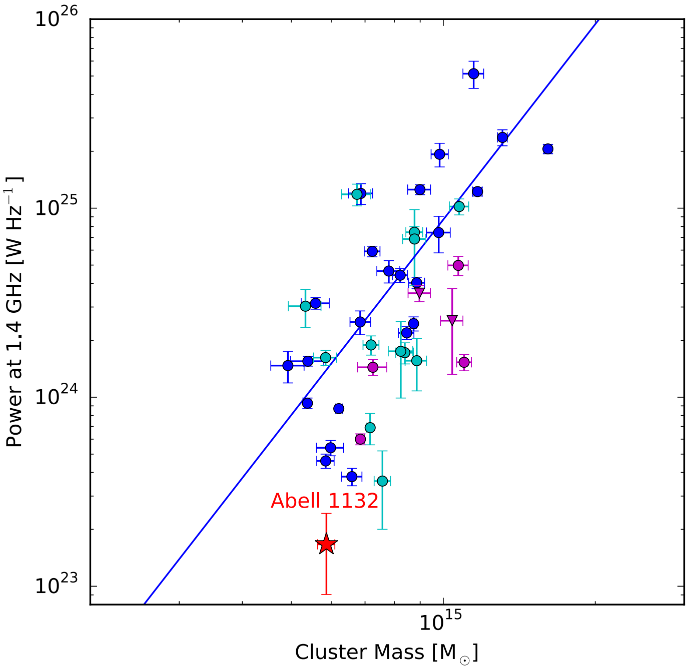

Figure 2.7: A sample of radio halos plotted by their radio power at 1.4 GHz versus their cluster mass (M_{500} – as determined from Planck observations). The sample of halos and their correlation is reproduced from Martinez Aviles et al. (2016). Halos with flux measured at 1.4 GHz are marked by blue circles and their derived fit is shown as a blue line. Cyan circles represent halos with flux measured at frequencies other than 1.4 GHz. Magenta circles represent ultra-steep halos, and magenta triangles represent ultra-steep halos with flux measured at frequencies other than 1.4 GHz. Abell 1132 is marked by the red star, and falls well below the correlation line as well as below all the halos in this sample.

LOFAR diffuse emission, after compact-source-subtraction, is shown in red in Fig. 2.1 and as contours overlaid on our FACTOR image in Fig. 2.5. It is apparent in Fig. 2.5 that there is a hole (negative artifact) to the north-east of the brightest cluster galaxy. The negative artifact likely occurred because there was imperfect calibration, modelling, and subtraction of the brightest cluster galaxy, as it has no prior model and it is embedded in diffuse halo emission. In LOFAR facet-calibrated images, negative artifacts, or negative bowls, often occur near bright sources that have not been previously modeled. This hole appears to be the only one in the cluster field and is on a relatively small scale. The negative artifact remains after the compact-source-subtraction, and is indicated by negative contours (dashed) in Fig. 2.5. It is possible that the halo emission extends within this region, but future low-frequency observations would be needed for confirmation.

Diffuse emission, after compact-source-subtraction, at 144 and 325 MHz are shown together in Fig. 2.6. The size and morphology of the halo is comparable in both the LOFAR and GMRT images, however, the LOFAR image of the halo shows some additional, weaker emission to the south, possibly connecting to the diffuse emission in the giant HT. The bulk of the detected diffuse emission lies slightly west of the cluster center, exhibiting a subtle offset (~ 200 kpc) from the center of the Chandra X-ray emission. The halo takes on a roughly elliptical shape, shorter in the north-south direction and elongated from south-east to north-west, with a major axis of ~ 750 kpc and minor axis of ~ 570 kpc, as seen by LOFAR. The surface brightness of the halo (after subtraction of central galaxies) within 3σ contours is ~ 0.8 μJy arcsec^{-2} at 144 MHz with $\sigma = 350$ μJy beam^{-1} and a beam size of $30'' \times 26''$ (see Fig. 2.5).

We produced GMRT images at 610 MHz tapered to $30''$ resolution to enhance diffuse emission, but the radio halo is not detected above 2σ where $\sigma \approx 100$ μJy beam^{-1}. Archival VLA observations performed in D array were retrieved, reduced and re-imaged, but diffuse emission near the cluster center is not detected above 2σ where $\sigma \approx 250$ μJy beam^{-1}.

Halo spectral index estimate

We estimate the spectral index of the halo by imaging the compact-source-subtracted datasets at 144 and 325 MHz in CASA `CLEAN` with the same minimum uv-range (100λ), same outer uv-taper ($20''$), and uniform weighting, and compare the flux densities within the same region after re-gridding[13] and smoothing to the same beam size ($19'' \times 19''$). In a region indicated by 2σ contours at 325 MHz where $\sigma = 130$ μJy beam^{-1}, the spectral index is $\alpha = -1.80 \pm 0.18$. In a region indicated by 3σ contours at 325 MHz (east portion of halo), the spectral index is $\alpha = -1.71 \pm 0.19$, and in another region indicated by 3σ contours at 325 MHz (west portion of halo) the spectral index is $\alpha = -1.74 \pm 0.20$. (See the regions as contours in Fig. 2.6: Right.) Therefore, we give an average spectral index estimate of $\alpha = -1.75 \pm 0.19$ and classify this radio halo as ultra-steep. With a spectral index of $\alpha = -1.75$, the surface brightness of the halo emission would be ~ 1.3 μJy arcsec^{-2} at 1.4 GHz, and considering a 15% error[14] in our total measured flux at 144 MHz and an error of ± 0.19 in the spectral index, the radio power at 1.4 GHz is determined to be $P_{1.4} = (1.66 \pm 0.76) \times 10^{23}$ W Hz^{-1}.

It has been found that the radio power of halos correlate with the X-ray luminosity of the

---

[13] We shifted the LOFAR map by -2 pixels in X-direction and -3 pixels in Y-direction to correct for an astrometric offset. This pixel shift was determined by comparing the high-resolution LOFAR and GMRT maps imaged with the same settings and convolved to the same beam ($11''$) and calculating the offset of the maximum pixel of several point sources near the cluster center.

[14] We approximate the error in the halo's flux by assuming a 10% error from FACTOR calibration, modeling, and imaging (based on experience) and introducing a 5% error from the contamination of the residual emission of subtracted central galaxies.

host cluster (Brunetti et al., 2007, 2009; Cassano et al., 2013; Yuan et al., 2015). In Fig. 2.7, we plot the radio power at 1.4 GHz versus the Planck cluster mass M_{500} for a sample of radio halos and include Abell 1132's halo, indicated by the red star. The halo is not only ultra-steep but also extremely weak: the plot in Fig. 2.7 shows Abell 1132's halo lying well below the correlation line. It is possible that this ultra-steep halo sets an unprecedented record for the weakest halo discovered so far. The fact that it is so steep and weak, as seen at low-frequency, is consistent with the non-detection of diffuse emission at 1.4 GHz.

2.3.2 Giant Radio Galaxy: Head-Tail

The GRG is a prominent feature of the radio emission from the cluster, exhibiting long and narrow emission with a projected linear size of 1.3 Mpc. The head of this emission coincides with an elliptical galaxy[2] near the same redshift as Abell 1132 (see Fig. 2.4). The giant tail, as seen by LOFAR, is the same head-tail source as seen in NVSS and in reprocessed WENSS data, but there the tail is only detected to be 370 kpc long (Rudnick & Lemmerman, 2009). The GRG appears to be one-sided, since only one jet is visible. It is likely that the jets have joined into a single tail aligned behind the trajectory of the galaxy as it has moved west-to-east. The giant tail in Abell 1132 has similar physical characteristics to the tail in Abell 2256 (Owen et al., 2014), however, it is more than twice as long as the tail in Abell 2256. If the host galaxy was moving at the sound speed of the cluster, ~ 1000 km s^{-1}, then it is possible that the AGN has been active for ~ 1 Gyr, which is much greater than typical AGN life cycles (on the order of a few Myr).

The GRG has traveled from west-to-east through the cluster outskirts, leaving the observed tail as a trail of AGN emission, but its vast extent challenges the fact that the tail electrons 1 Mpc and further from the AGN head should no longer be emitting. The separation in the tail at 1 Mpc, where the emission becomes more diffuse (see Fig. 2.1 & 2.5), is interesting: here, dormant tail electrons may have been disrupted and re-accelerated, leading to a re-brightening that gives rise to the additional 300 kpc of diffuse emission (de Gasperin et al., 2017 reports a similar re-brightening of dormant tail electrons from a WAT radio galaxy within the massive merging cluster Abell 1033 and attributes it to “gentle re-energisation”). It also appears that the radio halo connects to the diffuse portion of the tail (see Fig. 2.5). A connection between the halo and tail may give an indication of where the seed particles needed for turbulent re-acceleration come from. However, a question remains in how the length of the tail up to 1 Mpc could retain its collimated form if it has been affected by merger turbulence. Since the diffuse portion is not visible in the GMRT images at 325 or 610 MHz (Fig. 2.3), it is likely to be very steep and very weak emission. If the diffuse portion has been re-accelerated, its emission should have a slightly flatter spectral index than the steepest part of the collimated portion.

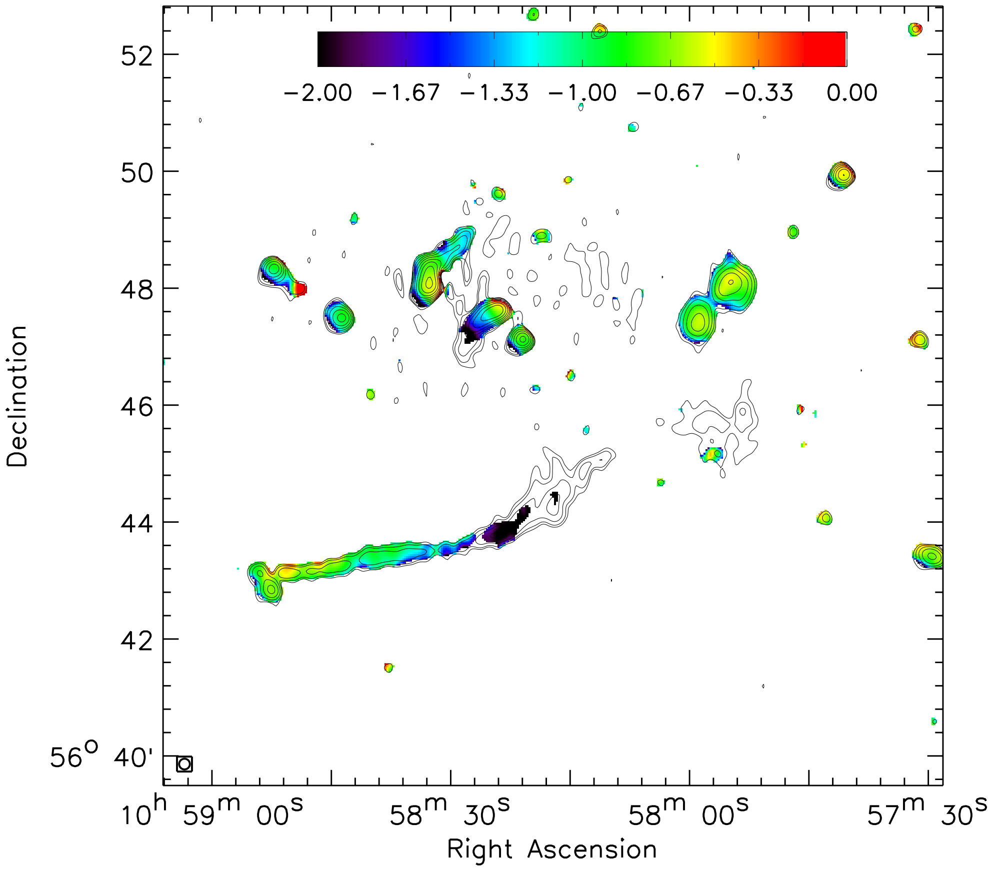

Figure 2.8: Spectral index map of the giant HT galaxy using emission cut above 3σ from LOFAR at 144 MHz and GMRT at 325 and 610 MHz. LOFAR and GMRT emission are imaged in CASA `CLEAN` with an outer uv-taper of $10''$, uniform weighting, and a minimum uv-range of 200λ with RMS noise of $\sigma_{140} = 300$ μJy beam^{-1}, $\sigma_{325} = 100$ μJy beam^{-1}, and $\sigma_{610} = 60$ μJy beam^{-1}. All images were smoothed to the same beam size ($11'' \times 11''$). Maps at 144 MHz and 325 MHz were re-gridded to the map at 610 MHz[13]. LOFAR emission is also shown as black contours with levels $\sigma_{140} \times [3.45, 6, 12, 24, 48, 96, 192, 384, 768]$.

In Fig. 2.8 a spectral index map of LOFAR and GMRT images aids in classifying the HT galaxy. The spectrum steepens along the length of the tail, with a spectral index of $\alpha \approx -2$ at a distance of ~ 800 kpc from the head. At further distances only LOFAR detects emission, hence a spectral index could not be determined for the detached portion of the tail beyond 1 Mpc. An upper limit can be placed for the detached, more diffuse portion by comparing the mean flux at 144 MHz to 2σ at 325 and 610 MHz (see caption of Fig. 2.8 for values of σ). The upper limit of the spectral index is $\alpha < -2.3$ for 325 MHz and $\alpha < -1.7$ for 610 MHz.

The WAT to the west of the cluster center (see Figs. 2.2 & 2.3) follows a similar trajectory to the HT. It appears to be moving from west-to-east on the outskirts of the cluster, leaving two tails of AGN emission. The longer tail has a projected size of ∼ 650 kpc and the shorter tail has a projected size of ∼ 450 kpc.

2.4 Discussion and Conclusions

The discovery of this radio halo in Abell 1132 demonstrates LOFAR's potential to detect weak, steep-spectrum emission on large scales. The steep-spectrum halo in Abell 1132 is noteworthy for three reasons:

(i) with a spectral index of $\alpha = -1.75 \pm 0.19$ it is one of the steepest halos detected to date

(ii) with a size of ∼ 650 kpc and radio power of $\mathrm{P}_{1.4} = (1.66 \pm 0.76) \times 10^{23}$ W Hz^{-1} the halo is smaller than usual and it is remarkably faint

(iii) the halo is ∼ 200 kpc offset from the X-ray emission of the cluster.

A few other ultra-steep halos include $\alpha \approx -2.1$ in A521 (Brunetti et al., 2008), $\alpha \approx -1.7$ to -1.8 in A697 (Macario et al., 2010), and A1682 (Macario et al., 2013). Steep-spectrum radio halos challenge hadronic models because energy arguments rule out the possibility that very steep halos with $\alpha \sim -1.5$ to -2 are produced by cosmic-ray electrons that follow power-laws in momentum (Pfrommer & Enßlin, 2004; Brunetti et al., 2008). However, turbulent re-acceleration models do predict a large population of steep-spectrum halos, which exhibit a break in their electron spectra near energies of a few GeV (Brunetti et al., 2004, 2008). Most radio halos known today, discovered at higher radio frequencies (1.4 GHz), are produced by mergers between the most massive galaxy clusters. According to the turbulent re-acceleration model, radio halos with much steeper spectra should be produced by less energetic, more frequent mergers. Hence, the bulk of radio halos may have yet to be discovered because they are only visible at low frequencies. Given its sensitivity to diffuse emission with low surface brightness, LOFAR will be a valuable tool to reveal this population.

In hadronic models the radio emission of the halo should also roughly follow the X-ray surface brightness, as the X-ray emission traces the thermal ICM that provides the targets for the hadronic collisions. Clearly, this is not the case in the halo in Abell 1132. The fact that the halo is smaller and fainter also supports a turbulent re-acceleration origin of halos, as the steeper-spectrum halos are produced by older populations of relativistic electrons that can no longer sustain a luminous halo. Hence, we may be witnessing a radio halo that is transitioning into an “off” state. It would be interesting to determine the dynamical status of the cluster merger using optical spectroscopy, in order to relate the radio properties of the halo to the phase and energetics of the cluster merger. With much better spectral capabilities than the current X-ray telescopes, the future X-ray observatory ATHENA may be able to probe turbulence within Abell 1132’s intracluster medium.

The discovery of the radio halo and GRG found together in one cluster has raised the question about a possible connection. The presence of a radio halo suggests that the cluster has recently undergone a merger, but it is unclear whether the merger has affected the emission of the GRG. Near the GRG-head the emission appears to be mostly undisturbed, very narrow, and collimated, but the furthest emission of the tail is more diffuse. It may be possible that the 1.3 Mpc tail is visible because it has been re-accelerated by turbulent merger activity. A spectral index measurement of this disturbed portion as compared to the collimated portion would reveal the age of this emission and clarify whether it has been re-accelerated. This cluster is a prime target for studying merger mechanisms and the re-acceleration of dormant electrons.

Acknowledgements

This work was supported by the Deutsche Forschungsgemeinschaft (DFG) through the Collaborative Research Centre SFB 676 “Particles, Strings and the Early Universe”, project C2. LOFAR, the Low Frequency Array designed and constructed by ASTRON, has facilities in several countries, that are owned by various parties (each with their own funding sources), and that are collectively operated by the International LOFAR Telescope (ILT) foundation under a joint scientific policy. The LOFAR software and dedicated reduction packages on https://github.com/apmechev/GRID$_LRT$ were deployed on the e-infrastructure by the LOFAR e-infragroup, consisting of J. B. R. Oonk (ASTRON & Leiden Observatory), A. P. Mechev (Leiden Observatory) and T. Shimwell (Leiden Observatory) with support from N. Danezi (SURFsara) and C. Schrijvers (SURFsara). This work has made use of the Dutch national e-infrastructure with the support of SURF Cooperative through grant e-infra160022. We thank the staff of the GMRT that made these observations possible. GMRT is run by the National Centre for Radio Astrophysics of the Tata Institute of Fundamental Research. This research has made use of the NASA/IPAC Extragalactic Data Base (NED) which is operated by the JPL, California institute of technology under contract with the National Aeronautics and Space administration. TS acknowledges support from the

ERC Advanced Investigator programme NewClusters 321271. F.A-S. acknowledges support from *Chandra* grant GO3-14131X. EKM acknowledges support from the Australian Research Council Centre of Excellence for All-sky Astrophysics (CAASTRO), through project number CE110001020. RM gratefully acknowledges support from the European Research Council under the European Union's Seventh Framework Programme (FP/2007-2013) ERC Advanced Grant RADIOLIFE-320745. AOC gratefully acknowledges support from the European Research Council under grant ERC-2012-StG-307215 LODESTONE. We also thank A. Botteon (Università di Bologna) and G. Kokotanekov (University of Amsterdam) for their helpful comments.

References

Abazajian K., et al., 2004, AJ, 128, 502

Ackermann M., et al., 2010, ApJ, 717, L71

Ackermann M., et al., 2016, ApJ, 819, 149

Anders E., Grevesse N., 1989, Geochimica Cosmochimica Acta, 53, 197

Arnaud K. A., 1996, in Jacoby G. H., Barnes J., eds, Astronomical Society of the Pacific Conference Series Vol. 101, Astronomical Data Analysis Software and Systems V. p. 17

Blasi P., Colafrancesco S., 1999, Astroparticle Physics, 12, 169

Bonafede A., et al., 2012, MNRAS, 426, 40

Bonafede A., et al., 2014, MNRAS, 444, L44

Brienza M., et al., 2017, A&A, 606, A98

Brunetti G., Jones T. W., 2014, International Journal of Modern Physics D, 23, 1430007

Brunetti G., Setti G., Feretti L., Giovannini G., 2001, MNRAS, 320, 365

Brunetti G., Blasi P., Cassano R., Gabici S., 2004, MNRAS, 350, 1174

Brunetti G., Venturi T., Dallacasa D., Cassano R., Dolag K., Giacintucci S., Setti G., 2007, ApJ, 670, L5

Brunetti G., et al., 2008, Nature, 455, 944

Brunetti G., Cassano R., Dolag K., Setti G., 2009, A&A, 507, 661

Brunetti G., Blasi P., Reimer O., Rudnick L., Bonafede A., Brown S., 2012, MNRAS, 426, 956

Cassano R., Brunetti G., Setti G., 2006, MNRAS, 369, 1577

Cassano R., Brunetti G., Norris R. P., Röttgering H. J. A., Johnston-Hollitt M., Trasatti M., 2012, A&A, 548, A100

Cassano R., et al., 2013, ApJ, 777, 141

Condon J. J., Cotton W. D., Greisen E. W., Yin Q. F., Perley R. A., Taylor G. B., Broderick J. J., 1998, AJ, 115, 1693

Cuciti V., Cassano R., Brunetti G., Dallacasa D., Kale R., Ettori S., Venturi T., 2015, A&A, 580, A97

Dehghan S., Johnston-Hollitt M., Franzen T. M. O., Norris R. P., Miller N. A., 2014, AJ, 148, 75

Dennison B., 1980, ApJ, 239, L93

Donnert J., Dolag K., Brunetti G., Cassano R., Bonafede A., 2010a, MNRAS, 401, 47

Donnert J., Dolag K., Cassano R., Brunetti G., 2010b, MNRAS, 407, 1565

Donnert J., Dolag K., Brunetti G., Cassano R., 2013, MNRAS, 429, 3564

Enßlin T., Pfrommer C., Miniati F., Subramanian K., 2011, A&A, 527, A99

Feretti L., Giovannini G., Govoni F., Murgia M., 2012, A&ARv, 20, 54

Giovannini G., Feretti L., 2000, New Astron., 5, 335

Intema H. T., Jagannathan P., Mooley K. P., Frail D. A., 2017, A&A, 598, A78

Jeltema T. E., Profumo S., 2011, ApJ, 728, 53

Kaiser C. R., Alexander P., 1999, MNRAS, 302, 515

Kempner J. C., Blanton E. L., Clarke T. E., Enßlin T. A., Johnston-Hollitt M., Rudnick L., 2004, in Reiprich T., Kempner J., Soker N., eds, The Riddle of Cooling Flows in Galaxies and Clusters of galaxies. (`arXiv:astro-ph/0310263`)

Keshet U., Markevitch M., Birnboim Y., Loeb A., 2010, ApJ, 719, L74

Lane W. M., Cotton W. D., Helmboldt J. F., Kassim N. E., 2012, Radio Science, 47, RS0K04

Macario G., Venturi T., Brunetti G., Dallacasa D., Giacintucci S., Cassano R., Bardelli S., Athreya R., 2010, A&A, 517, A43

Macario G., et al., 2013, A&A, 551, A141

Mahony E. K., et al., 2016, MNRAS,

Martinez Aviles G., et al., 2016, A&A, 595, A116

McMullin J. P., Waters B., Schiebel D., Young W., Golap K., 2007, in Shaw R. A., Hill F., Bell D. J., eds, Astronomical Society of the Pacific Conference Series Vol. 376, Astronomical Data Analysis Software and Systems XVI. p. 127

Miley G., 1980, ARA&A, 18, 165

Miniati F., Beresnyak A., 2016, IAU Focus Meeting, 29, 700

O'Dea C. P., Owen F. N., 1985, AJ, 90, 954

Offringa A. R., et al., 2014, MNRAS, 444, 606

Owen F. N., Rudnick L., Eilek J., Rau U., Bhatnagar S., Kogan L., 2014, ApJ, 794, 24

Petrosian V., 2001, ApJ, 557, 560

Pfrommer C., Enßlin T. A., 2004, A&A, 413, 17

Planck Collaboration et al., 2014, A&A, 571, A29

Pratt G. W., Croston J. H., Arnaud M., Böhringer H., 2009, A&A, 498, 361

Rengelink R. B., Tang Y., de Bruyn A. G., Miley G. K., Bremer M. N., Roettgering H. J. A., Bremer M. A. R., 1997, A&AS, 124

Rudnick L., Lemmerman J. A., 2009, ApJ, 697, 1341

Ryu D., Kang H., Cho J., Das S., 2008, Science, 320, 909

Saripalli L., Hunstead R. W., Subrahmanyan R., Boyce E., 2005, AJ, 130, 896

Scaife A. M. M., Heald G. H., 2012, MNRAS, 423, L30

Shimwell T. W., et al., 2016, MNRAS, 459, 277

Shimwell T. W., et al., 2017, A&A, 598, A104

Sommer M. W., Basu K., Intema H., Pacaud F., Bonafede A., Babul A., Bertoldi F., 2017, MNRAS, 466, 996

Srivastava S., Singal A. K., 2016, preprint, (`arXiv:1610.07783`)

Struble M. F., Rood H. J., 1999, ApJS, 125, 35

Thierbach M., Klein U., Wielebinski R., 2003, A&A, 397, 53

Vazza F., Brunetti G., Gheller C., 2009, MNRAS, 395, 1333

Vazza F., Jones T. W., Brüggen M., Brunetti G., Gheller C., Porter D., Ryu D., 2017, MNRAS, 464, 210

Vikhlinin A., Markevitch M., Murray S. S., Jones C., Forman W., Van Speybroeck L., 2005, ApJ, 628, 655

Wells D. C., 1985, NRAO'S Astronomical Image Processing System (AIPS). Springer US, Boston, MA, pp 195–209, doi:10.1007/978-1-4615-9433-8_18, `http://dx.doi.org/10.1007/978-1-4615-9433-8_18`

Williams W. L., et al., 2016, MNRAS, 460, 2385

Willingale R., Starling R. L. C., Beardmore A. P., Tanvir N. R., O'Brien P. T., 2013, MNRAS, 431, 394

Yuan Z. S., Han J. L., Wen Z. L., 2015, ApJ, 813, 77

de Gasperin F., et al., 2017, Science Advances

van Haarlem M. P., et al., 2013, A&A, 556, A2

van Weeren R. J., et al., 2016, ApJS, 223, 2

van Weeren R. J., et al., 2017, Nature Astronomy, 1, 0005

3 Search for low-frequency diffuse radio emission around a shock in the massive galaxy cluster MACS J0744.9+3927

– **Amanda Wilber, Marcus Brüggen, Annalisa Bonafede, David Rafferty, Federica Savini, Timothy W. Shimwell, Reinout J. van Weeren, Andrea Botteon, Rossella Cassano, Gianfranco Brunetti, Francesco de Gasperin, Denis Wittor, Matthias Hoeft, Laura Birzan** –

Monthly Notices of the Royal Astronomical Society, published on 19 February 2018

Abstract

Merging galaxy clusters produce low Mach number shocks in the intracluster medium. These shocks can accelerate electrons to relativistic energies that are detectable at radio frequencies. MACS J0744.9+3927 is a massive ($M_{500} = (11.8 \pm 2.8) \times 10^{14} M_{\odot}$), high-redshift ($z = 0.6976$) cluster where a Bullet-type merger is presumed to have taken place. Sunyaev-Zel'dovich maps from MUSTANG indicate that a shock, with Mach number $\mathcal{M} = 1.0 - 2.9$ and an extension of ~ 200 kpc, sits near the centre of the cluster. The shock is also detected as a brightness and temperature discontinuity in X-ray observations. To search for diffuse radio emission associated with the merger, we have imaged the cluster with the LOw Frequency ARray (LOFAR) at 120-165 MHz. Our LOFAR radio images reveal previously undetected AGN emission, but do not show clear cluster-scale diffuse emission in the form of a radio relic nor a radio halo. The region of the shock is on the western edge of AGN lobe emission from the brightest cluster galaxy. Correlating the flux of known shock-induced radio relics versus their size, we find that the radio emission overlapping the shocked region in MACS J0744.9+3927 is likely of AGN origin. We argue against the presence of a relic caused by diffusive shock acceleration and suggest that the shock is too weak to accelerate electrons from the intracluster medium.

3.1 Introduction

3.1.1 Cluster mergers and shocks

Mergers between galaxy clusters produce large-scale, low-Mach number ($\mathcal{M} \leq 4 - 5$) shock waves in the intracluster medium (ICM). These shocks are thought to accelerate ICM particles to ultra-relativistic energies and potentially amplify ICM magnetic fields (e.g. Vazza et al., 2009; Brüggen et al., 2012; Vazza et al., 2017). Observations of merging clusters over a wide range of wavelengths are currently constraining the physics behind these shocks. See Hoeft & Brüggen (2007) and Brunetti & Jones (2014) for reviews of shocks and non-thermal emission associated with these events.

The thermal component of the ICM consists of hot gas (10^{7-8} K or 1-10 keV) that is visible in X-rays through bremstrahlung emission. A merging cluster may show an elongated or disturbed X-ray morphology, usually indicating the direction of the merger. Shocks are pressure discontinuities that can be identified as sharp edges in the brightness and temperature distribution of the ICM X-ray emission (e.g. Markevitch et al., 2002; Markevitch & Vikhlinin, 2007; Ogrean et al., 2013; Botteon et al., 2018).

The mass and merging status of a cluster can also be inferred from the thermal Sunyaev-Zel'dovich (SZ) effect, where electrons in the ICM up-scatter cosmic microwave background (CMB) photons. The SZ decrement[1] is proportional to the line-of-sight integral of the plasma pressure and hence shocks appear as substructures in the SZ signal of a cluster. Since the SZ decrement has no dependence on the distance, there is the opportunity to discover shocks even in distant clusters (Komatsu et al., 2001; Kitayama et al., 2004; Korngut et al., 2011; Mason et al., 2010; Korngut et al., 2011; Romero et al., 2015; Young et al., 2015). Ferrari et al. (2011) were the first to use MUSTANG SZ maps and X-ray data to confirm a shocked region in the most X-ray luminous cluster RX J1347-1145, and showed that there was a radio excess coincident with the shock in the form of a mini halo. Recently the SZ effect was used to characterize a shock in the Coma cluster using Planck data (Erler et al., 2015). More recently, ALMA has achieved very high resolutions (up to 3.5 arcsec), detecting the highest redshift shock known ($z = 0.87$) in ACT-CL J0102-4915 or the 'El Gordo' cluster (Basu et al., 2016).

Many merging cluster systems are observed to host cluster-scale radio emission in the form of radio halos and/or radio relics (see Feretti et al., 2012, for a review). Radio halos are

---

[1] A decrement is seen only below $\sim$ 220 GHz; above this frequency there is an increment.

classified as diffuse emission at the cluster centre, thought to be the product of turbulent re-acceleration of ICM particles driven by a cluster merger (e.g. Brunetti et al., 2001). Gischt relics are classified as elongated or arching diffuse radio emission typically found on the cluster periphery (e.g. Rottgering et al., 1997; Bagchi et al., 2006; Bonafede et al., 2009; van Weeren et al., 2010, 2012; Bonafede et al., 2014), and are thought to trace shock waves induced by cluster mergers (Brüggen et al., 2011, 2012). Active galactic nuclei (AGN) relics, or phoenix relics, are usually much smaller, more roundish in appearance, and consist of aged or "ghost" AGN emission that has been re-energized by shocks (e.g Enßlin & Gopal-Krishna, 2001; Slee et al., 2001; de Gasperin et al., 2015).

The details of the necessary acceleration mechanisms and the efficiencies of low Mach number shocks are still largely unknown (see Brunetti & Jones, 2014, for a review). Along a shock front, diffusive shock acceleration (DSA) is believed to accelerate electrons that could produce synchrotron emission at radio wavelengths (Blandford & Ostriker, 1978; Ensslin et al., 1998). However, the low Mach numbers of most observed shocks are usually too weak to accelerate particles from the thermal pool (van Weeren et al., 2016b; Botteon et al., 2016a; Eckert et al., 2016). Hence, some form of pre-acceleration or an upstream population of relativistic seed electrons is required for DSA to operate. One possible pre-acceleration mechanism is shock drift acceleration (SDA) (Matsukiyo et al., 2011; Guo et al., 2014b,a), which has been simulated in a cosmological context by Vazza et al. (2016) and Wittor et al. (2017). AGN are another potential source for seed electrons, and several examples have been found, the clearest being the connection between a radio relic and radio galaxy in Abell 3411-3412 (van Weeren et al., 2017).

Most merging clusters with X-ray detected shocks are shown to host some type of diffuse radio emission. There are a few cases where shocks coincide with the edges of radio halos (e.g Markevitch et al., 2005; Uchida et al., 2016), but most shocks in merging clusters are associated with radio relics. Very recently, Hlavacek-Larrondo et al. (2018) presented highly sensitive Jansky Very Large Array (JVLA) observations of the low mass merging cluster Abell 2146 that revealed diffuse radio emission associated with two confirmed X-ray shocks which was previously undetected by Russell et al. (2011) in observations by the Giant Meterwave Radio Telescope (GMRT).

Searching for diffuse radio emission at confirmed shock locations in the ICM is a key test to validate the widely held model that radio relics are produced by shocks. Radio observations of smaller shocks and shocks with lower Mach numbers are especially of interest, potentially yielding limits on the efficiencies of theorized acceleration mechanisms. High redshift clusters also test the sensitivities of our radio telescopes, and allow us to determine the effect of inverse Compton scattering which becomes stronger as the CMB energy density increases.

3.1.2 MACS J0744.9+3927

An intracluster shock sits just outside the centre of the massive and distant galaxy cluster MACS J0744.9+3927 (Korngut et al., 2011). This cluster is located at RA: 07h44m52.47s, Dec: $+39°27'27.3''$, at a redshift of $z = 0.6976$ (Ebeling et al., 2007). Durret et al. (2016) give a mass derived from the XMM Newton archival data as $M_{500} = 9.9 \times 10^{14} M_{\odot}$. MACS J0744.9+3927 is a CLASH (Cluster Lensing And Supernova survey with Hubble; Postman et al., 2012) cluster with a weak lensing derived mass of $M_{500} = (11.837 \pm 2.786) \times 10^{14} M_{\odot}$ (Sereno et al., 2015), consistent (within 1σ) with the XMM-derived mass.

Using MUSTANG observations, Korngut et al. (2011) found an SZ-decrement as a kidney-shaped ridge in the north-south direction with a length of $\sim$ 25 arcsec (180 kpc). The kidney-shaped feature is located between the system's main mass peak and a second, smaller mass peak. The region of this ridge overlaps a discontinuity in the Chandra X-ray image. To accurately quantify the discontinuity, Korngut et al. (2011) measured X-ray surface brightness and temperature changes over the elliptical radius of the cluster, and found that there is temperature increase and a slight brightness drop-off coincident with the SZ decrement, suggesting that this region is shock-heated gas and the second highest redshift shock known after the one in El Gordo (Botteon et al., 2016b).

The Mach number obtained from the density jump conditions, as calculated from the fit to the X-ray surface brightness, was $\mathcal{M} = 1.2^{+0.2}_{-0.2}$ where the errors are 1σ. The temperature jump conditions at the shock yield a higher value, $\mathcal{M} = 2.1^{+0.8}_{-0.5}$; however, the error bars are large and the value agrees with the Mach number inferred from the density jump condition at the 1.3σ level. The shock velocity in this cluster is $V_{\rm sh} = 1827^{+267}_{-195}$ km s^{-1} assuming the Mach number obtained from the density jump conditions (Korngut et al., 2011).

The dynamics of the cluster-sub-cluster merger is unclear. A subcluster lies 300 kpc west of the centre of the main cluster and a mass lensing reconstruction from Richard et al. (2011) shows elongation toward the west. Korngut et al. (2011) suggest that the subcluster has passed through the main cluster core from the east to the west in a Bullet-type fashion and ram-pressure has stripped off baryons from the subcluster. Shocked gas appears to be hugging the westward portion of the main cluster core, in between the two merging clusters, which is not the place where a merger shock would be expected. Typically, the shocks found in Bullet-type mergers, either bow or counter, are found outside of the merged system as a whole, and not in between the two subclusters (e.g Russell et al., 2010; Shimwell et al., 2014; Botteon et al., 2016b). The size and position of the shock suggest that it is not the type of merger shock that has been observed to produce prominent radio relics such as the Sausage (e.g. Hoang et al., 2017) or Toothbrush (e.g. van Weeren et al., 2016b) relics because those are all on the peripheral regions of the cluster and exhibit significant scale ($\sim$ 1 Mpc). Guennou et al. (2014) presented an X-ray image of the cluster from XMM Newton and state that the residual X-ray image shows an extended structure coincident with the SZ excess as seen by Korngut et al. (2011), but they favour the scenario that the extended appearance is due to a substructure attached to the cluster, potentially from an infalling group. The direction of the potential infalling group and the angular separation between it and the main cluster is uncertain.

Radio surveys covering MACS J0744.9+3927, including the Faint Images of the Radio Sky at Twenty-Centimeters (FIRST; White et al. 1997) and the NRAO VLA Sky Survey (NVSS; Condon et al. 1998), do not detect any significant radio sources in the cluster field. MACS J0744.9+3927 was selected to be targeted with the LOw Frequency ARray (LOFAR; van Haarlem et al., 2013) because it is a very high-mass and high-z cluster with evidence of merging activity and a shock detection in SZ. In this paper we present LOFAR observations of MACS J0744.9+3927 at 120-165 MHz (with a central frequency of 143 MHz) to search for a radio relic associated with the shock. LOFAR's sensitivity to steep-spectrum low-surface-brightness emission is crucial for detecting weak and diffuse radio emission on cluster scales. Assuming the following cosmology, $\mathrm{H}_0 = 70$, $\Omega_m = 0.3$, and $\Omega_\Lambda = 0.7$, the angular scale at MACS J0744.9+3927's redshift ($z = 0.6976$) is 7.223 kpc arcsec^{-1}, used hereafter.

3.2 LOFAR observation of MACS J0744.9+3927

LOFAR is a low-frequency radio interferometer with a compact core and stations that extend over large parts of Northern Europe (van Haarlem et al., 2013). Our observation was part of the LOFAR Two-meter Sky Survey (LoTSS; Shimwell et al. 2017) and uses the high-band antennas (HBA) over a frequency range of 120-165 MHz. The data reduction steps for this data are identical to the data reduction steps described in Wilber et al. (2018), and are summarised below.

3.2.1 Prefactor

Prefactor[2] is a package containing automated pipelines called Pre-Facet-Calibration and Initial-Subtract. Pre-Facet-Calibration compresses and averages the original data and performs all initial, direction-independent calibration. In this step a flux calibrator (observed at the beginning and end of the target observation) is used to compute amplitude gain solutions, station clock offsets, station phase offsets, and station differential total electron content (dTEC). Amplitude gain solutions and corrections for clock and phase offsets are then transferred to the target field data. An initial phase calibration is also performed using a global sky model from the TIFR GMRT Sky Survey (TGSS) at 150 MHz (Intema et al., 2017). For this observation the calibrator 3C196 was used, a bright quasar (66 Jy at 159 MHz according to the Scaife & Heald 2012 absolute flux scale). After the direction-independent calibration is completed, preliminary imaging is carried out via the Initial-Subtract pipeline. The full wide-field of the calibrated target data is imaged in high and low resolution using `WSClean` (Offringa et al., 2014). These full field images are used to model and subtract all sources in preparation for direction-dependent calibration.

3.2.2 FACTOR

Direction-dependent calibration for LoTSS data is significantly simplified and refined through the facet calibration technique (van Weeren et al., 2016a). This method of calibration is executed via the FACTOR[3] software package. FACTOR first tesselates the full target field into several smaller patches of sky called facets. Each facet is automatically chosen to be centered on a bright compact source to be used as a facet calibrator. TEC, phase, and amplitude solutions are computed from the facet calibrator and applied to all sources in that facet. Facets are processed in order of brightness and as the brighter sources are progressively subtracted, with adequate calibration solutions, the effective noise in the *uv*-data is reduced. After a facet is calibrated, it is imaged with `WSClean` and a primary beam correction is applied. For more details on facet calibration the reader is referred to van Weeren et al. (2016a), Shimwell et al. (2016a), and Williams et al. (2016).

For this observation, FACTOR was run on the full 45 MHz bandwidth of target data. The wide-field was tessellated into 40 directions with one direction designated as the target facet, containing MACS J0744.9+3927, and 18 bright and nearby facets were processed before imaging the target facet. The target facet was imaged after applying the calibration solutions from a nearby[4] bright source in a neighboring facet. The final image of the target facet produced

---

[2] https://github.com/lofar-astron/prefactor

[3] http://www.astron.nl/citt/facet-doc

[4] $\sim 0.3^\circ$ angular separation

by FACTOR has a resolution of 8.6 arcsec × 6.5 arcsec with root mean square (rms) noise of $\sigma \approx 180\ \mu\text{Jy beam}^{-1}$.

Data calibrated with FACTOR often show a slight astrometric offset because phase solutions change quickly over small regions of sky (due to the spatially changing conditions of the ionosphere; Williams et al. 2016). The LOFAR map was initially offset from the optical and SZ map. We calculated an astrometric shift by comparing the LOFAR radio map at 143 MHz to a high resolution GMRT map at 610 MHz with corrected astrometry from van Weeren et al. (in preparation). We measured the offset in arcseconds between the maximum pixel locations of several point sources in and around the cluster centre. A shift of RA, Dec: [-2.5,0] arcsec was applied to all LOFAR images to match the GMRT astrometry.

3.3 Results

3.3.1 Subtraction of compact sources

Our LOFAR image of MACS J0744.9+3927 shows an active galaxy at the cluster centre. It sits within the X-ray emission of the cluster but slightly toward the east (see Fig. 3.1). This central AGN is likely associated with the optical source SDSS J074452.77+392726.7, the brightest cluster galaxy (BCG), with a redshift of $z = 0.6986 \pm 0.0007$[5]. The radio emission from this galaxy appears round and compact in the high-resolution image. There is another compact radio source on the northern edge of the X-ray emission (labeled in Fig. 3.1). This emission might come from an active galaxy, but the only optically visible galaxy coincident with the radio peak in this region does not have a confirmed redshift (SDSS J074452.36+392748.8). Therefore, it is not possible to say whether this northern emission is a background or foreground galaxy, or if it is actually extended lobe emission from the AGN associated with the BCG.

In order to search for cluster-scale diffuse emission associated with the shocked region, a subtraction of compact sources was carried out using CASA (Common Astronomy Software Applications; McMullin et al., 2007). The subtraction was performed on the *uv*-data by imaging with a *uv*-range of $> 6000\ \lambda$ (filtering out emission that spans more than 34 arcsec or ~ 250 kpc)[6] and Briggs' robust parameter of 0.25. The CLEAN components of the result-

---

[5] From the Sloan Digital Sky Survey Data Release 1 as obtained Aug. 28, 2003 from http://das.sdss.org/DR1/data/spectro/ss$_tar_2$0

[6] We also attempted the subtraction at a *uv*-range of $> 2000\ \lambda$ and $> 4000\ \lambda$ which correspond to emission spanning less than $\sim$ 750 kpc and $\sim$ 400 kpc, respectively, but decided to increase the cut to reduce the possibility of subtracting diffuse emission possibly related to the shocked region since this region is on a

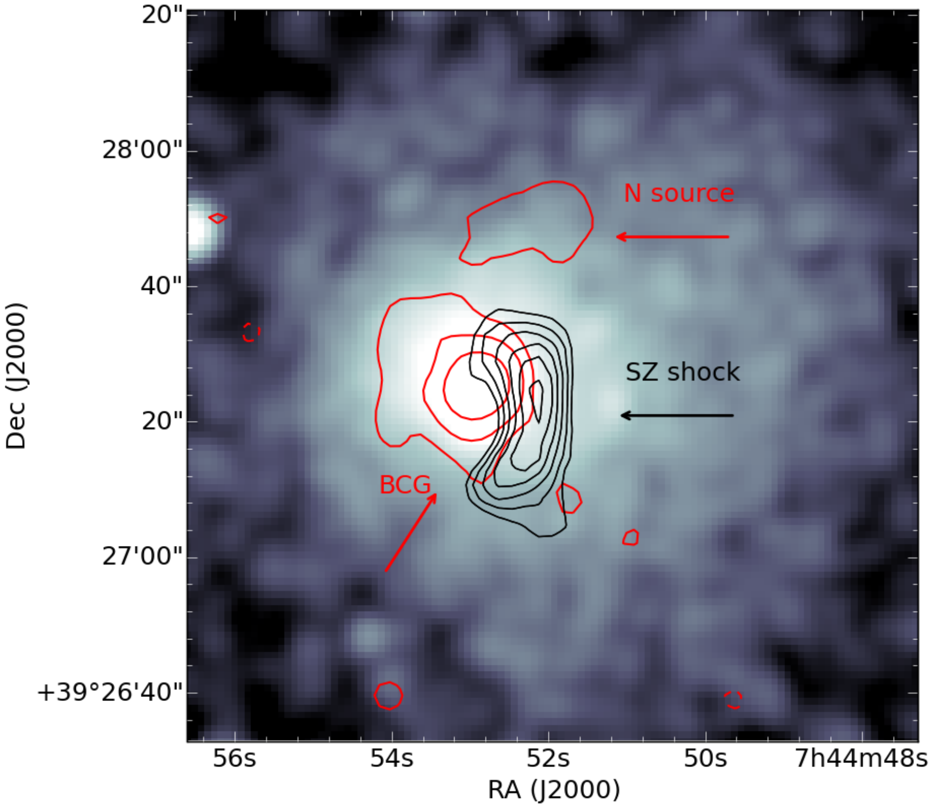

Figure 3.1: Chandra X-ray emission in blue with LOFAR high-resolution FACTOR image contours $[-3, 3, 6, 12] \times \sigma$ overlaid in red. X-ray emission is smoothed with a Gaussian kernel. RMS noise of our LOFAR image is $\sigma = 180$ μJy beam^{-1} with a beam size of 8.6 arcsec × 6.5 arcsec. Black contours show the SZ-decrement as detected by MUSTANG, from Korngut et al., 2011, starting at 3σ with 0.5σ increments. LOFAR detects a compact BCG AGN and a compact northern source.

ing image were then subtracted from the *uv*-dataset using the tasks FTW and UVSUB. The dataset was then re-imaged with a *uv*-range of > 80 λ[7], a slight outer *uv*-taper to bring out extended emission (6 arcsec as shown in Fig. 3.2 and 10 arcsec as shown in Fig. 3.3)[8], and a robust parameter of 0. This method of compact source subtraction is not perfect and the resulting image may still include residual emission or artefacts associated with the compact source, or diffuse emission can be subtracted, but a manual inspection of the clean component model proved that no diffuse emission was removed.

---

relatively small scale.

[7] FACTOR calibration solutions are determined from data with a *uv*-range of > 80 λ to eliminate the shortest baselines which can introduce significant large scale emission manifested as noise. Since the target data is calibrated with solutions > 80 λ we also image selecting data > 80 λ.

[8] Outer *uv*-taper values greater that 10 arcsec appeared to artificially inflate the size of existing emission due to smearing from a larger synthesized beam. Since it is at such high redshift, this cluster requires higher-resolution imaging.

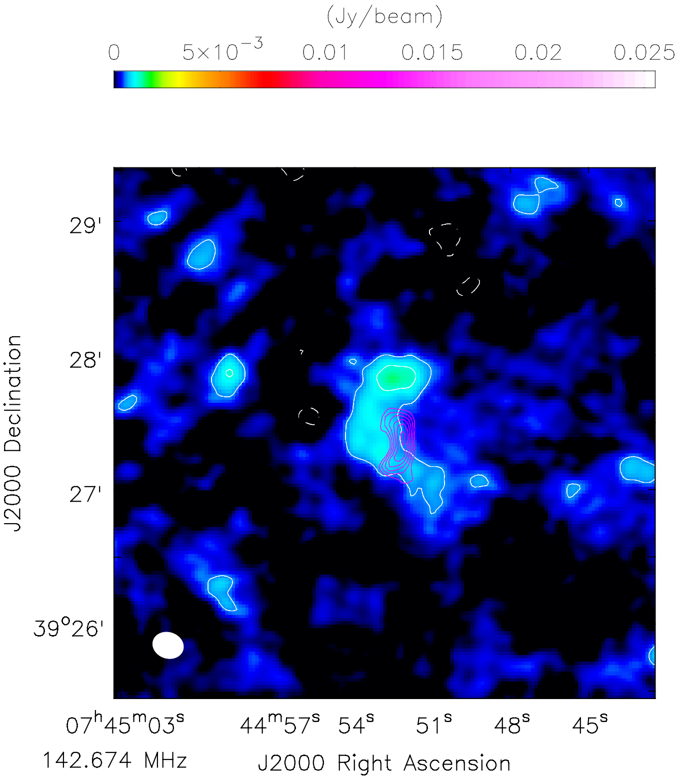

Figure 3.2: LOFAR image after subtracting compact sources imaged at a *uv*-range of $> 6000\ \lambda$. An outer *uv*-taper of 6 arcsec was used to bring out diffuse emission. RMS noise is $\sigma = 180\ \mu$Jy beam^{-1} and the restoring beam is 14 arcsec × 12 arcsec. White contours are $[-3, 3, 6, 9] \times \sigma$. Magenta contours show the SZ feature, considered to be a merger-induced shock, as detected by MUSTANG from Korngut et al., 2011.

Our final compact-source-subtracted image shows faint diffuse emission near the cluster centre extending to the north and south of the BCG (Fig. 3.2 & Fig. 3.3). An optical image of the cluster with LOFAR compact emission and diffuse emission overlaid as contours can be seen in Fig. 3.4. The northern diffuse emission is brightest with a peak flux of 933 μJy within the 9σ contour where $\sigma = 200\,\mu$Jy beam^{-1} (in Fig. 3.3), which is likely from a separate AGN north of the BCG. We suspect that the diffuse emission at the cluster centre extending southwest is part of radio lobes associated with the BCG. There is no significant emission coincident with the kidney-shaped ridge seen in the SZ map. In fact, the diffuse radio emission falls off in the direction that the SZ decrement increases (see Fig. 3.4). There is also no diffuse emission resembling a radio halo at the cluster centre.

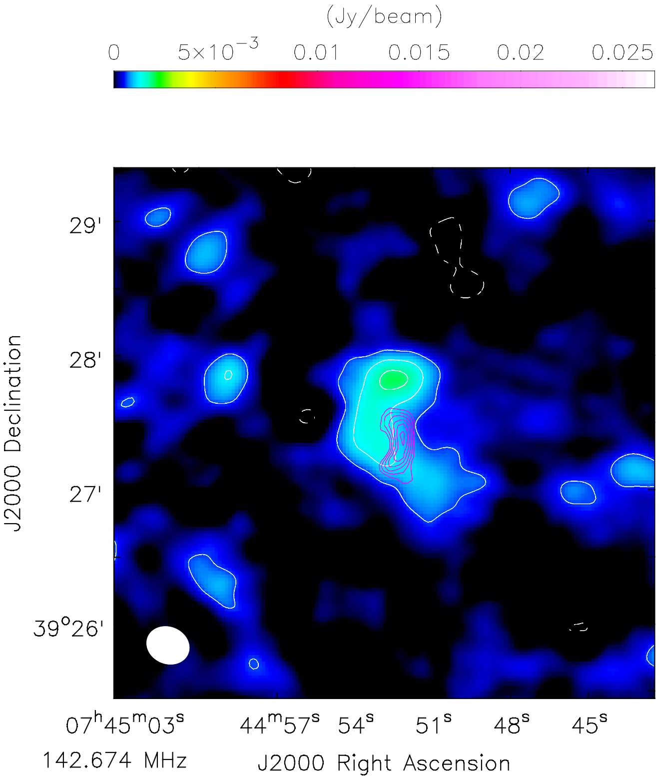

Figure 3.3: LOFAR image after subtracting compact sources imaged at a *uv*-range of $> 6000\ \lambda$. An outer *uv*-taper of 10 arcsec was used to bring out diffuse emission. White contours are $[-3, 3, 6, 9] \times \sigma$ where $\sigma = 200\ \mu$Jy beam^{-1} and the restoring beam is 19 arcsec × 16 arcsec. Magenta contours are from the MUSTANG SZ map. Extended emission is visible up to 570 kpc, and likely consists of emission from multiple AGN.

3.3.2 Search for radio relics

There is no clear radio structure coinciding with the shock detected by SZE observations. The only emission present at the shocked region is what we suspect to be the fading southwestern edge of the AGN lobe associated with the BCG. To determine an upper limit on a potential radio relic associated with the shock, we calculate the radio power within the shocked region from our low-resolution image (14 arcsec × 12 arcsec) made with the compact-source-subtracted *uv*-dataset that was imaged in CASA `CLEAN` with an outer *uv*-taper of 6 arcsec (Fig. 3.2).

The flux density at 143 MHz is measured within a pie cut of three annuli, where the beginning and ending angles of the pie align with the north and south boundaries of the lowest

Table 3.1: Small & faint radio relics / candidate radio relics

Relic	$\log_{10}(P_{1.4})$[W Hz^{-1}]	LLS [Mpc]	References
A13	23.85	0.25	Feretti et al. (2012); Slee et al. (2001)
A85	23.50	0.35	Feretti et al. (2012); Slee et al. (2001)
A725	23.11	0.44	Böhringer et al. (2000); Kempner & Sarazin (2001)
A2034 F	22.60	0.6	Shimwell et al. (2016b)
A2048	23.66	0.31	van Weeren et al. (2011b)
A2443	23.30	0.43	Feretti et al. (2012); Cohen & Clarke (2011)
A4038	23.01	0.13	Feretti et al. (2012); Slee et al. (2001)
MAXBCG138+25	25.01	0.19	van Weeren et al. (2011a)
Sausage R1	24.03	0.63	Hoang et al. (2017)
Sausage R2	24.27	0.67	Hoang et al. (2017)
Toothbrush D	24.15	0.25	van Weeren et al. (2016b)
24P73	23.88	0.27	van Weeren et al. (2011b)

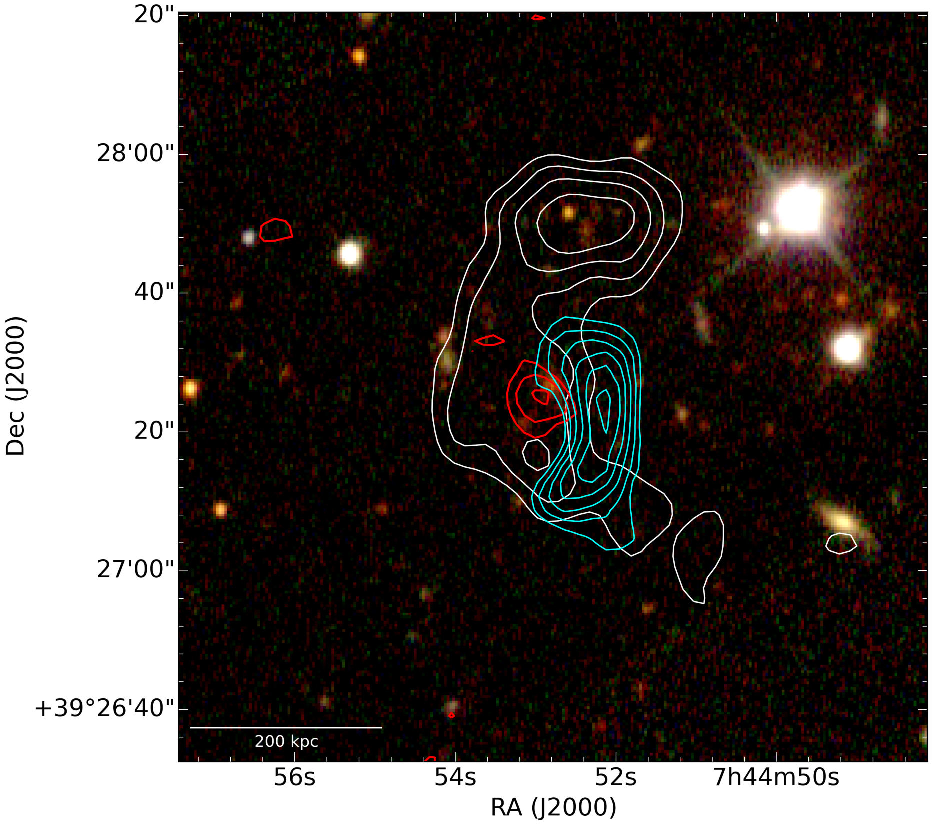

Figure 3.4: SDSS *g,r,i* image with radio emission overlaid as contours. LOFAR compact emission imaged with a *uv*-range > 6000 λ is shown by red contours $[3, 6, 9] \times \sigma$ where $\sigma = 200\mu$Jy beam^{-1}. LOFAR diffuse emission after compact source subtraction is shown in white contours where contours are $[3, 4, 5, 6] \times \sigma$ and $\sigma = 200\mu$Jy beam^{-1} (same as Fig. 3.3). Cyan contours are from the SZ MUSTANG map from Korngut et al. 2011.

contour (3σ) of the SZ decrement as seen by MUSTANG (presented in Korngut et al., 2011). Fig. 3.5 shows the pie cut annuli region in white and the SZ ridge in black overlaid on our low-resolution LOFAR image. The outer two annuli effectively cover the area of the shock as indicated by SZE observations, and the inner annulus extends from the inner edge of the kidney-shaped ridge toward the cluster centre[9].

Within a region defined by the outer two annuli shown in Fig. 3.5, the flux density at 143 MHz is $S_{143} = 1.18 \pm 0.12$ mJy with a corresponding radio power of $P_{143} = (2.84 \pm 0.28) \times 10^{24}$ W Hz^{-1}. Within a region defined by the total pie cut, including the inner annulus, the flux density is found to be $S_{143} = 2.05 \pm 0.21$ mJy with a corresponding radio power of $P_{143} = (4.90 \pm 0.49) \times 10^{24}$ W Hz^{-1}. Here we include a k-correction to account for redshift using a spectral index of $\alpha = -1.2$ where $S \propto \nu^{\alpha}$. The error in our flux density measurement

---

[9] The cluster centre as marked by the brightness distribution in X-ray emission.

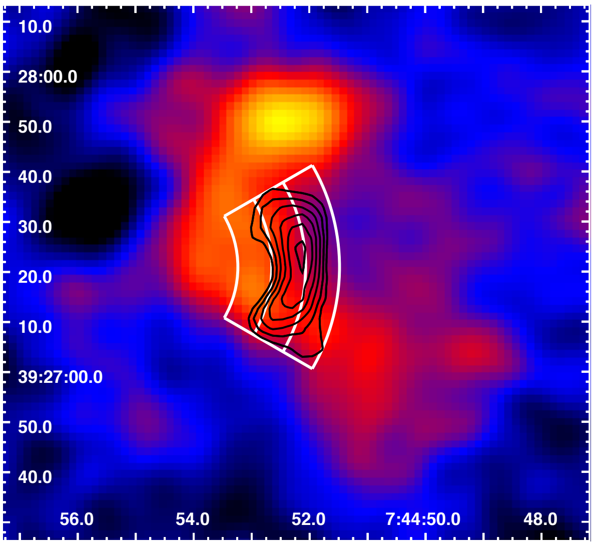

Figure 3.5: Pie cut region (shown in white) in which the flux density is measured to determine a radio relic upper limit. Black contours are from the MUSTANG map. The radio relic upper limit is measured from our compact-source-subtracted LOFAR image with an outer *uv*-taper of 6 arcsec.

is assumed to be 10%, which is determined by comparing flux densities of several sources in our LOFAR map to the same sources in TGSS (Intema et al., 2017) and the 7C survey (Hales et al., 2007).

We extrapolate the flux density value within the total pie cut, defined by the three annuli, to 1.4 GHz by assuming a range of potential spectral indices that include the typical values measured for relics found at merger shocks (gischt-type relics) and AGN-relics which can have even steeper spectral indices. We choose a conservative range of $\alpha = -1$ to -1.5. This gives a 1.4 GHz flux density range of $S_{1.4} = (0.06 - 0.23)$ mJy, corresponding to a radio power range of $P_{1.4} = (1.71 - 4.99) \times 10^{23}$ W Hz^{-1}.

In the above calculations for flux density and radio power at 1.4 GHz, we choose to use the 143 MHz flux density within the total pie cut (which is a region starting at the cluster centre and ending at the outer edge of kidney-shaped ridge, ~ 140 kpc in width) rather than just using the flux which is coincident with the MUSTANG SZE contours. An ALMA detection from Basu et al. (2016) showed that a pressure discontinuity (SZ decrement) of the merger shock in El Gordo is coincident with the width of the radio relic seen at 2.1 GHz. However, MUSTANG has a lower resolution and lower sensitivity than ALMA, and radio relics are seen to widen at low frequencies. For this reason, we calculate the potential relic flux density from annuli covering the shocked region as indicated by SZE observations in addition to the flux within an annulus extending east of the SZ ridge toward the cluster centre.

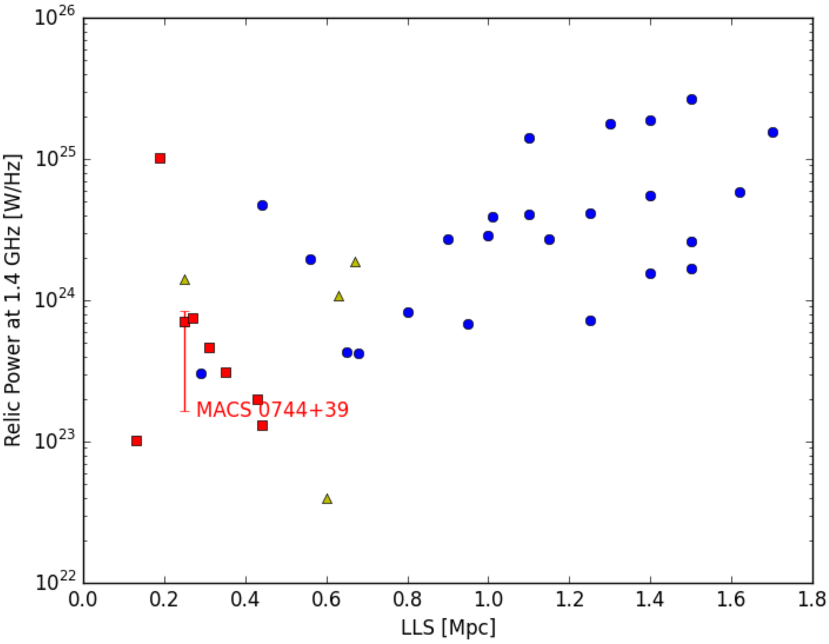

Figure 3.6: A sample of gischt radio relics (blue circles) and AGN/phoenix relics (red squares) from Nuza et al. (2017) plotted by their power at 1.4 GHz versus their LLS in Mpc. Yellow triangles represent additional relics / candidate relics from Table 4.1. The red line represents the upper limit range of the power for the radio emission detected within the shocked region for MACS J0744.9+3927. Powers include a k-correction to account for redshift, with an average spectral index of $\alpha = -1.2$, as is used in Nuza et al. (2017).

In Table 4.1 we make a list of observed relics / candidate relics that are smaller (largest linear scale (LLS) < 0.7 Mpc) and/or fainter ($\log_{10}(P_{1.4}) < 24.3$ W Hz^{-1})[10] than most gischt relics. In Fig. 3.6 we plot a large sample of observed radio relics by their power at 1.4 GHz versus their LLS. This sample is taken from a list of confirmed gischt-type relics and smaller phoenix relics presented in Nuza et al. (2017) as well as the additional smaller relics / candidate relics listed in Table 4.1. We calculate the power for each relic from the flux density at 1.4 GHz and include a k-correction with an average spectral index of $\alpha = -1.2$, as is used in Nuza et al. (2017). We include the extrapolated radio power range for the shocked region in MACS J0744.9+3927, using the LLS of the shock as seen by MUSTANG (250 kpc). The largest value of this power range is fainter than that of most observed gischt-type relics (shown as blue circles in Fig. 3.6), however, since the LLS is smaller than most gischt-type relics, a lower power would be expected. On the basis of the measured power range alone, a gischt-type relic cannot be ruled out. The power range and LLS agree more closely with powers and sizes seen

---

[10] We note that the small relic in MAXBCG138+25 is perhaps an important outlier since it is much brighter than other small phoenix/AGN relics.

in phoenix-type relics (shown as red squares in Fig. 3.6).

Based on the location of the shock and the LLS, it does not seem likely that a gischt-type relic would be generated, and indeed we see no such clear radio structure resembling a gischt relic at the shock site. The absence of a morphological structure resembling a relic is interesting, particularly in light of the high electron acceleration efficiency observed in radio relics, which is still poorly understood (Vazza & Brüggen, 2014).

3.3.3 Upper limit on particle acceleration efficiency

Taking the parameters of the shock wave detected in MACS J0744.9+3927 (an average Mach number of $\mathcal{M} = 1.75$ and shock velocity $V_{\rm sh} = 1827$ km s^{-1}) and the non-detection of a radio relic, we can compute an upper limit on the particle acceleration efficiency. Comparing the dissipated kinetic power at the shock to the total power in the radio emission, we can estimate the acceleration efficiency using equation 2 in Botteon et al. (2016a):

$$\int_{\nu_0} L(\nu) d\nu \simeq \frac{1}{2} \eta_{\rm e} \Psi \rho_{\rm u} V_{\rm sh}^3 (1 - C^{-2}) \frac{B^2}{B_{\rm cmb}^2 + B^2} S, \tag{3.1}$$

where $\eta_{\rm e}$ is the acceleration efficiency, $\rho_{\rm u}$ is the upstream density, $V_{\rm sh}$ is the shock velocity, C is the compression factor which is related to the Mach number via $C = 4\mathcal{M}^2/(\mathcal{M}^2 + 3)$, B is the magnetic field strength and $B_{\rm cmb} = 3.25(1+z)^2$, S is the surface area of the shock[11], and Ψ is the ratio of the energy injected in electrons emitting over the full spectrum versus electrons emitting in radio wavelengths, given by

$$\Psi = \frac{\int_{p_0} Q(p) E(p) dp}{\int_{p_{\rm min}} Q(p) E(p) dp}, \tag{3.2}$$

where $Q(p) \propto p^{-\delta_{\rm inj}}$ and $\delta_{\rm inj} = 2(\mathcal{M}^2 + 1)/(\mathcal{M}^2 - 1)$ (Blandford & Eichler, 1987). The momentum, p_0, is the momentum associated with electrons that emit the characteristic frequency of the synchrotron emission, $\nu_0 = p_0^2 eB/2\pi m_{\rm e}^3 c^3$. Here, $m_{\rm e}$ is the electron mass, e its charge, and c the speed of light. For the minimum momentum in the denominator, $p_{\rm min}$, we consider two cases: 1) for a low value of $p_{\rm min} = 0.1 m_{\rm e} c$ the efficiency has to be unrealistically high, $\gg 100\%$, and we cannot infer an upper bound for $\eta_{\rm e}$, or 2) the shock re-accelerates a population of relativistic seed electrons with $p_{\rm min} = 100 m_e c$, in which case the efficiency must be $\leq 19\%$ since a relic is not observed. Clearly, this number is uncertain, since it depends not only on $p_{\rm min}$, but also quite strongly on the assumed velocity of the shock, $V_{\rm sh}$, the upstream

---

[11] This area is the largest linear length times the largest linear width of the shocked region, defined by the pie cut in Fig. 3.5 (250×140 kpc^2).

density, $\rho_{\rm u}$, as well as the magnetic field, B. We used the value from Figure 5 in Korngut et al. (2011) for the upstream density ($\rho_{\rm u} = 0.013$ cm^{-3}), and since the magnetic field in this cluster is not known we assume a value of $B = 1$ μG.

3.3.4 Missing radio halo

The study of radio halos in high-mass and high-z merging clusters is crucial to constrain the model of turbulent re-acceleration. In the turbulent re-acceleration scenario, it is expected that the fraction of ultra-steep-spectrum radio halos increases strongly with redshift because of stronger inverse Compton losses (Cassano et al., 2010).

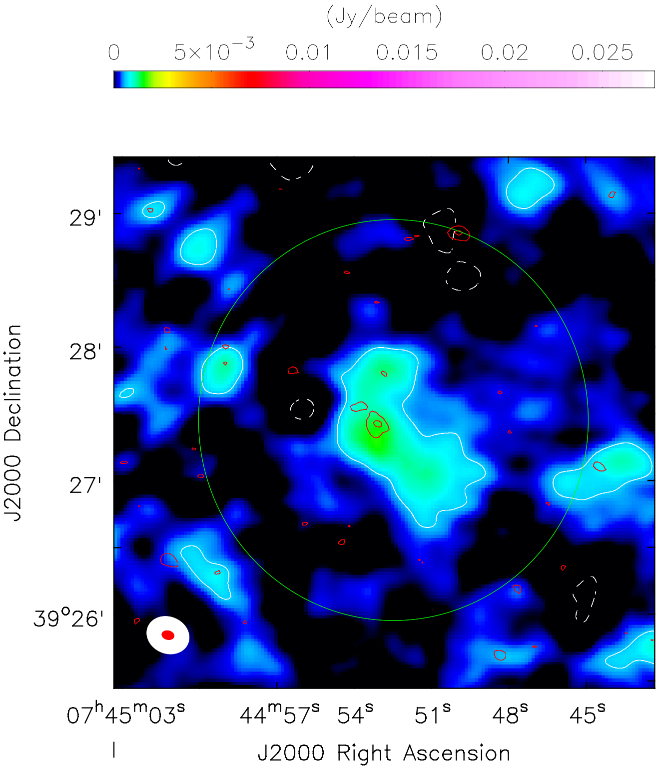

Figure 3.7: LOFAR image after subtracting sources imaged at a uv-range of > 4000 λ. An outer uv-taper of 10 arcsec was used to bring out diffuse emission. RMS noise is $\sigma = 200\mu$Jybeam^{-1}. White contours represent $[-3, 3] \times \sigma$. Red contours $[3, 12] \times \sigma$ are the compact sources imaged with uv-range > 4000 λ, which were subtracted. The green circle represents the area that would be expected for a radio halo in a cluster of this mass, with a radius of 650 kpc. We use flux density measurements in this region to determine a the radio halo power upper limit.

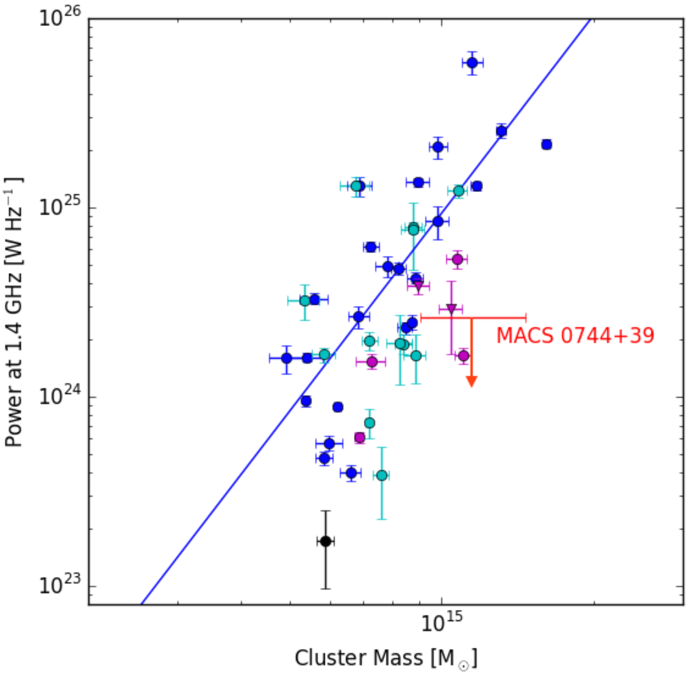

Figure 3.8: A sample of radio halos plotted by their radio power at 1.4 GHz versus their cluster mass (M_{500} – as determined from Planck observations). The sample of halos and their correlation is reproduced from Martinez Aviles et al. (2016). Halos with flux measured at 1.4 GHz are marked by blue circles and their derived fit is shown as a blue line. Cyan circles represent halos with flux measured at frequencies other than 1.4 GHz. Magenta circles represent ultra-steep halos, and magenta triangles represent ultra-steep halos with flux measured at frequencies other than 1.4 GHz. The ultra-steep-spectrum radio halo in Abell 1132 is also included from Wilber et al. 2018, and is marked by a black circle. The upper limit of radio halo power at 1.4 GHz in MACS J0744.9+3927 is represented by the red arrow. We note that this power is likely an overestimation since it consists of AGN lobe power. All the halo powers include a k-correction with an averaged spectral index of $\alpha = -1.3$, as in Martinez Aviles et al. (2016).

In MACS J0744.9+3927, the LOFAR image does not show a radio halo, even though the X-ray and SZ data indicate that this system is in the process of a merger, albeit not a major one. Diffuse emission at the cluster centre is most likely caused by the active BCG as well as the galaxy north of it whose redshift is unknown. If there is radio halo emission, it is eclipsed by the emission of the active galaxies, whose lobes extend to ~ 570 kpc. However, a high-mass cluster such as this would be expected to host a radio halo on larger scales (Cassano et al., 2007).

To determine an upper limit on the flux of a radio halo, we use an image made after subtracting compact sources imaged at a *uv*-range of $> 4000\ \lambda$ (corresponding to emission spanning less than ~ 400 kpc) with rms noise of $\sigma = 200\ \mu$Jy beam^{-1} (see Fig. 3.7). We estimate the upper limit of a radio halo by defining a circular region (shown as the green circle in Fig. 3.7) with an origin at the cluster centre and a radius of 650 kpc, as would be expected for a cluster this mass. The upper limit on the flux density is expressed as the summation of flux density from two regions within this circle: 1) the flux density within 3σ contours of the central diffuse emission (which includes AGN emission), and 2) the rms noise, σ, times the number of beams covering the remaining area inside the circle and outside of the central 3σ contours. We state that this upper limit of $S_{143} = 19.9$ mJy is probably an overestimate since it clearly includes emission originating from AGN. Assuming a spectral index of $\alpha = -1.3$ and including k-correction, we find that the extrapolated power at 1.4 GHz of this upper limit is $P_{1.4} = 2.61 \times 10^{24}$ W Hz^{-1} and falls below the correlation for radio halo power versus cluster mass for a sample of clusters (see Fig. 3.8). Since there are no Planck observations of this cluster, we must use the cluster mass as derived by weak-lensing from CLASH[12]. Given the large errors in the mass for MACS J0744.9+3927, the upper limit for the radio power shown in Fig. 3.8 is not far from the correlation at the lower end of the mass estimate. Moreover, for a given mass, the scatter in radio halo power is quite large, and the correlation may change once deeper and more systematic searches for halos are underway.

3.3.5 Radio halo injection

We simulate a radio halo by injecting a radio source into the *uv*-data that has a central brightness I_0 and an e-folding radius of r_e, which is defined as the radius at which the brightness drops to I_0/e (e.g. Brunetti et al., 2007; Venturi et al., 2008; Bonafede et al., 2017). The length scale r_e is therefore relatively independent on the sensitivity of the radio images. The radio halo we inject has a size and brightness specified by the correlation in Fig. 3.8 ($P_{1.4} = 8.54 \times 10^{24}$ W Hz^{-1} and $R_H = 650$ kpc for a cluster with $M_{500} = 9.9 \times 10^{14} M_\odot$), such that $I_0 = 0.115$ μJy arcsec^2 and $r_e = 250$ kpc. The model of this mock radio halo is Fourier transformed into the visibility data (MODEL_DATA column), taking into account the w-projection parameter. A relatively empty region near the cluster centre, void of bright sources or artefacts, is chosen to host the injected flux (at RA: 07h44m34.12s, Dec: $+39°26'42.3''$). The dataset is then re-imaged with Briggs' robust parameter 0 and an outer *uv*-taper of 10 arcsec. Since we set the power at 1.4 GHz, a flatter spectral index would translate to a weaker power at 143 MHz than a steeper spectral index[13]. We adjust the spectral index from $\alpha = -1.0$ to -1.8 and determine when the injected flux is visible at 143 MHz. The injected halo is considered detected when it is recovered above 2σ with a diameter of roughly $3r_e$. We find that the spectral index must be $\alpha \leq -1.5$ for the halo to be recovered in our LOFAR

---

[12] The CLASH mass range is consistent within 1σ with the cluster mass value derived from XMM Newton X-ray data.

[13] Radio halos are usually shown to exhibit spectral indices < -1.

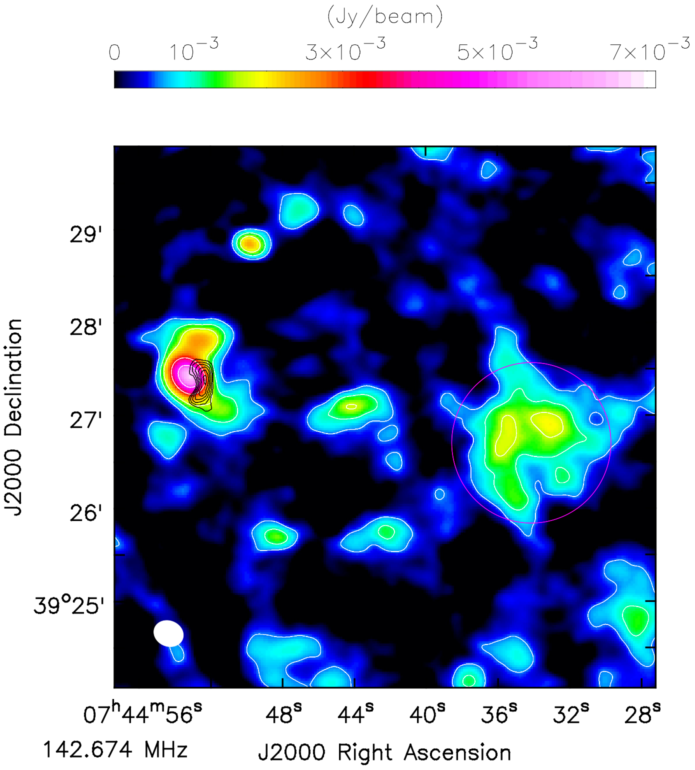

Figure 3.9: LOFAR image after injecting a simulated radio halo, with a power of $P_{1.4} = 8.54 \times 10^{24}$ W Hz^{-1} at 1.4 GHz and a spectral index of $\alpha = -1.5$, to the west of the cluster centre. The magenta circle has a radius of $3r_e$ centered on the coordinates where the simulated halo was injected. White contours are $[2, 4, 6, 12, 18] \times \sigma$ where $\sigma = 300$ μJybeam^{-1}. The flux density of the recovered halo is measured within the circular magenta region, above 2σ, and is found to be 20.02 ± 2.00 mJy.

images. With a spectral index of $\alpha = -1.5$, the total integrated flux density of the injected halo is 26.6 mJy at 143 MHz. Our LOFAR image of this simulated halo is shown in Fig. 3.9.

The flux density of the recovered halo is then measured in our LOFAR image within a region centered on the coordinates of the injected halo with a diameter of roughly $3r_e$. The integrated flux density of the recovered halo, above 2σ, is found to be 20.02 ± 2.00 mJy. This observed flux density is 75% that of the injected flux density. Compared to our upper limit determined in Sec. 3.3.4, the recovered flux density of the mock halo is approximately equal. If a halo with a spectral index ≤ -1.5 was present in this cluster, it is likely that our flux density upper limit would have been greater than the flux density of the recovered mock halo since our upper limit was measured including AGN emission as well. We argue that a halo with spectral index ≤ -1.5 is not present in this cluster, and that a halo with a flatter spectral index may exist but cannot be detected by our LOFAR observations at 143 MHz.

3.4 Discussion and Conclusion

Sunyaev-Zel'dovich and X-ray observations have revealed a shock, with Mach number $\mathcal{M} = 1.0 - 2.9$ and a length of ~ 200 kpc, near the centre of the cluster MACS J0744.9+3927. To search for diffuse radio emission associated with the merger, we have imaged the cluster with LOFAR at 120-165 MHz. Our LOFAR radio images do not show a radio relic coincident with the shock nor the presence of a radio halo at the cluster centre. With its estimated Mach number close to the Mach numbers of giant shock waves observed on cluster outskirts (which form powerful radio relics such as the Toothbrush relic) a search for radio emission associated with the shock in MACS J0744.9+3927 is important to understand the mechanisms of particle acceleration in the ICM.

Although the shock detected by MUSTANG is considered to be merger-induced by Korngut et al. (2011), it is very different from shocks that produce gischt-type relics, which are typically found on the cluster outskirts, since it is smaller and near the cluster centre. Instead of being induced by a merger, the shock may have been caused by an outburst of the central AGN. However, in (Korngut et al., 2011) it is also reported that there is the presence of a cold front behind the shock; this lends support to the merger-induced scenario for the shock front. Interestingly, simulations show bright mock relics occurring close to the cluster centre (Nuza et al., 2017); however, these have not yet been confirmed by observations.

The upper limit of the radio luminosity in the shocked region also suggests that no DSA at the shock front takes place as this process generally leads to higher luminosities relative to the size of the source (see Fig. 3.6). It is unclear why no DSA takes place, at least not with the efficiency that is observed in large radio relics. The magnetic field direction may have an influence on the efficiency of electron acceleration (e.g. Guo et al., 2014b). However, Wittor et al. (2017) have shown that the magnetic field distributions in galaxy clusters as predicted by cosmological magneto-hydrodynamical simulations have little effect on the radio luminosities of radio relics.

If pre-existing populations of older cosmic ray (CR) electrons are required for the injection into a DSA process, one would expect that close to a central radio galaxy there should be no shortage of seed CR-electrons: a phoenix-type relic caused by the re-acceleration of old AGN lobes might be expected in MACS J0744.9+3927. The AGN should contribute mildly energetic electrons which could then be re-accelerated via compression by the shock front. Another recently proposed mechanism is “gentle reenergization” (de Gasperin et al., 2017), in which old CR-electrons get accelerated on time-scales larger than sound crossing times to produce steep and filamentary radio emission, but this does not appear to happening in MACS J0744.9+3927.

While we suggest that the radio flux within the shocked region is probably not attributed to a gischt-type relic, due to the small size and central location of the shock, deeper upper limits on the radio power would be required to rule out this possibility. The upper limit of the radio power and the LLS of the shocked region agree more closely to known phoenix/AGN relics, but we argue that the emission present is not actually re-energized relic emission but simply a contamination from the original AGN lobe emission of the BCG.

Since we do not see a relic, or a re-brightening of AGN emission (in the form of a phoenix), it could be the case that the shock and the AGN are not in the same plane and that there is not a sufficient supply of seed electrons being injected into the shocked region. We find that the energy dissipated at the shock would be insufficient to accelerate a population of only very mildly relativistic electrons ($p_{\mathrm{min}} = 0.1 m_{\mathrm{e}} c$).

There is some disparity between the Mach numbers as determined from X-ray observations versus radio observations. It has been shown that radio emission of relics traces higher Mach numbers than those inferred from temperature or brightness discontinuities in X-ray (Hong et al., 2015; Itahana et al., 2015; Trasatti et al., 2015; Akamatsu et al., 2017). However, a Mach number of $\mathcal{M} = 2.1^{+0.8}_{-0.5}$ as inferred from MUSTANG and Chandra data is comparable to Mach numbers found, e.g. in the Toothbrush relic.

Finally, we also see no signs of a giant radio halo despite that this cluster is massive ($M_{500} = (11.837 \pm 2.786) \times 10^{14} M_{\odot}$; Sereno et al. 2015) and considered to be a merger. Radio halos at high redshifts are expected to have shorter life times because of the higher inverse Compton losses. Hence, one would expect a higher fraction of ultra-steep spectrum halos compared to lower redshifts. Still, the El Gordo cluster, which is one of the highest redshift ($z = 0.9$) and most massive merging clusters known, exhibits, both, radio relics and a radio halo that can be seen over a range of radio frequencies. Since MACS J0744.9+3927 has a mass similar to that of the El Gordo cluster, and is at a slightly lower redshift, it is surprising that a radio halo is not visible at low radio frequencies.

A simulation of a radio halo injected into our LOFAR data proves that a halo falling on the correlation line for a cluster this mass, with a spectral index $\alpha \leq -1.5$, is not present in the cluster. This cluster may host a radio halo with a flatter spectrum to which our low-frequency observations are not sensitive. This also brings into question the merger phase of this cluster. If it is in an early phase, it may explain why the merger shock is small and so close to the cluster center, and also why a radio halo with steep spectrum emission is not yet visible.

Acknowledgements

This work was supported by the Deutsche Forschungsgemeinschaft (DFG) through the Collaborative Research Centre SFB 676 “Particles, Strings and the Early Universe”, project C2. LOFAR, the Low Frequency Array designed and constructed by ASTRON, has facilities in several countries, that are owned by various parties (each with their own funding sources), and that are collectively operated by the International LOFAR Telescope (ILT) foundation under a joint scientific policy. The LOFAR software and dedicated reduction packages on https://github.com/apmechev/GRID$_{L}RT$ were deployed on the e-infrastructure by the LOFAR e-infragroup, consisting of J. B. R. Oonk (ASTRON & Leiden Observatory), A. P. Mechev (Leiden Observatory) and T. Shimwell (Leiden Observatory) with support from N. Danezi (SURFsara) and C. Schrijvers (SURFsara). This work has made use of the Dutch national e-infrastructure with the support of SURF Cooperative through grant e-infra160022. This work has made use of the Lofar Solution Tool (LoSoTo), developed by F. de Gasperin. This research has made use of the NASA/IPAC Extragalactic Data Base (NED) which is operated by the JPL, California institute of technology under contract with the National Aeronautics and Space administration. AB acknowledges supports from the ERC Stg 714245 DRANOEL. RvW acknowledges support from the ERC Advanced Investigator programme NewClusters 321271. DW acknowledges support by the DFG through grants SFB 676 and BR 2026/17 and by the ERC through Project No. 714196.

References

Akamatsu H., et al., 2017, A&A, 600, A100

Bagchi J., Durret F., Neto G. B. L., Paul S., 2006, Science, 314, 791

Basu K., Sommer M., Erler J., Eckert D., Vazza F., Magnelli B., Bertoldi F., Tozzi P., 2016, ApJ, 829, L23

Blandford R., Eichler D., 1987, Phys. Rep., 154, 1

Blandford R. D., Ostriker J. P., 1978, ApJ, 221, L29

Böhringer H., et al., 2000, ApJS, 129, 435

Bonafede A., Giovannini G., Feretti L., Govoni F., Murgia M., 2009, A&A, 494, 429

Bonafede A., Intema H. T., Brüggen M., Girardi M., Nonino M., Kantharia N., van Weeren R. J., Röttgering H. J. A., 2014, ApJ, 785, 1

Bonafede A., et al., 2017, MNRAS, 470, 3465

Botteon A., Gastaldello F., Brunetti G., Dallacasa D., 2016a, MNRAS, 460, L84

Botteon A., Gastaldello F., Brunetti G., Kale R., 2016b, MNRAS, 463, 1534

Botteon A., Gastaldello F., Brunetti G., 2018, MNRAS, 476, 5591

Brüggen M., van Weeren R. J., Röttgering H. J. A., 2011, Mem. Soc. Astron. Italiana, 82, 627

Brüggen M., Bykov A., Ryu D., Röttgering H., 2012, Space Sci. Rev., 166, 187

Brunetti G., Jones T. W., 2014, International Journal of Modern Physics D, 23, 1430007

Brunetti G., Setti G., Feretti L., Giovannini G., 2001, MNRAS, 320, 365

Brunetti G., Venturi T., Dallacasa D., Cassano R., Dolag K., Giacintucci S., Setti G., 2007, ApJ, 670, L5

Cassano R., Brunetti G., Setti G., Govoni F., Dolag K., 2007, MNRAS, 378, 1565

Cassano R., Brunetti G., Röttgering H. J. A., Brüggen M., 2010, A&A, 509, A68

Cohen A. S., Clarke T. E., 2011, AJ, 141, 149

Condon J. J., Cotton W. D., Greisen E. W., Yin Q. F., Perley R. A., Taylor G. B., Broderick J. J., 1998, AJ, 115, 1693

Durret F., et al., 2016, A&A, 588, A69

Ebeling H., Barrett E., Donovan D., Ma C.-J., Edge A. C., van Speybroeck L., 2007, ApJ, 661, L33

Eckert D., Jauzac M., Vazza F., Owers M. S., Kneib J.-P., Tchernin C., Intema H., Knowles K., 2016, MNRAS, 461, 1302

Enßlin T. A., Gopal-Krishna 2001, A&A, 366, 26

Ensslin T. A., Biermann P. L., Klein U., Kohle S., 1998, A&A, 332, 395

Erler J., Basu K., Trasatti M., Klein U., Bertoldi F., 2015, MNRAS, 447, 2497

Feretti L., Giovannini G., Govoni F., Murgia M., 2012, A&ARv, 20, 54

Ferrari C., et al., 2011, A&A, 534, L12

Guennou L., et al., 2014, A&A, 561, A112

Guo X., Sironi L., Narayan R., 2014a, ApJ, 794, 153

Guo X., Sironi L., Narayan R., 2014b, ApJ, 797, 47

Hales S. E. G., Riley J. M., Waldram E. M., Warner P. J., Baldwin J. E., 2007, MNRAS, 382, 1639

Hlavacek-Larrondo J., et al., 2018, MNRAS, 475, 2743

Hoang D. N., et al., 2017, MNRAS, 471, 1107

Hoeft M., Brüggen M., 2007, MNRAS, 375, 77

Hong S. E., Kang H., Ryu D., 2015, ApJ, 812, 49

Intema H. T., Jagannathan P., Mooley K. P., Frail D. A., 2017, A&A, 598, A78

Itahana M., Takizawa M., Akamatsu H., Ohashi T., Ishisaki Y., Kawahara H., van Weeren R. J., 2015, PASJ, 67, 113

Kempner J. C., Sarazin C. L., 2001, ApJ, 548, 639

Kitayama T., Komatsu E., Ota N., Kuwabara T., Suto Y., Yoshikawa K., Hattori M., Matsuo H., 2004, PASJ, 56, 17

Komatsu E., et al., 2001, PASJ, 53, 57

Korngut P. M., et al., 2011, ApJ, 734, 10

Markevitch M., Vikhlinin A., 2007, Phys. Rep., 443, 1

Markevitch M., Gonzalez A. H., David L., Vikhlinin A., Murray S., Forman W., Jones C., Tucker W., 2002, ApJ, 567, L27

Markevitch M., Govoni F., Brunetti G., Jerius D., 2005, ApJ, 627, 733

Martinez Aviles G., et al., 2016, A&A, 595, A116

Mason B. S., et al., 2010, ApJ, 716, 739

Matsukiyo S., Ohira Y., Yamazaki R., Umeda T., 2011, ApJ, 742, 47

McMullin J. P., Waters B., Schiebel D., Young W., Golap K., 2007, in Shaw R. A., Hill F., Bell D. J., eds, Astronomical Society of the Pacific Conference Series Vol. 376, Astronomical Data Analysis Software and Systems XVI. p. 127

Nuza S. E., Gelszinnis J., Hoeft M., Yepes G., 2017, MNRAS, 470, 240

Offringa A. R., et al., 2014, MNRAS, 444, 606

Ogrean G. A., Brüggen M., Röttgering H., Simionescu A., Croston J. H., van Weeren R., Hoeft M., 2013, MNRAS, 429, 2617

Postman M., et al., 2012, ApJS, 199, 25

Richard J., Jones T., Ellis R., Stark D. P., Livermore R., Swinbank M., 2011, MNRAS, 413, 643

Romero C. E., et al., 2015, ApJ, 807, 121

Rottgering H. J. A., Wieringa M. H., Hunstead R. W., Ekers R. D., 1997, MNRAS, 290, 577

Russell H. R., Sanders J. S., Fabian A. C., Baum S. A., Donahue M., Edge A. C., McNamara B. R., O'Dea C. P., 2010, MNRAS, 406, 1721

Russell H. R., et al., 2011, MNRAS, 417, L1

Scaife A. M. M., Heald G. H., 2012, MNRAS, 423, L30

Sereno M., Giocoli C., Ettori S., Moscardini L., 2015, MNRAS, 449, 2024

Shimwell T. W., Brown S., Feain I. J., Feretti L., Gaensler B. M., Lage C., 2014, MNRAS, 440, 2901

Shimwell T. W., et al., 2016a, MNRAS, 459, 277

Shimwell T. W., et al., 2016b, MNRAS, 459, 277

Shimwell T. W., et al., 2017, A&A, 598, A104

Slee O. B., Roy A. L., Murgia M., Andernach H., Ehle M., 2001, AJ, 122, 1172

Trasatti M., Akamatsu H., Lovisari L., Klein U., Bonafede A., Brüggen M., Dallacasa D., Clarke T., 2015, A&A, 575, A45

Uchida Y., Simionescu A., Takahashi T., Werner N., Ichinohe Y., Allen S. W., Urban O., Matsushita K., 2016, PASJ, 68, S20

Vazza F., Brüggen M., 2014, MNRAS, 437, 2291

Vazza F., Brunetti G., Gheller C., 2009, MNRAS, 395, 1333

Vazza F., Brüggen M., Wittor D., Gheller C., Eckert D., Stubbe M., 2016, MNRAS, 459, 70

Vazza F., Jones T. W., Brüggen M., Brunetti G., Gheller C., Porter D., Ryu D., 2017, MNRAS, 464, 210

Venturi T., Giacintucci S., Dallacasa D., Cassano R., Brunetti G., Bardelli S., Setti G., 2008, A&A, 484, 327

White R. L., Becker R. H., Helfand D. J., Gregg M. D., 1997, ApJ, 475, 479

Wilber A., et al., 2018, MNRAS, 473, 3536

Williams W. L., et al., 2016, MNRAS, 460, 2385

Wittor D., Vazza F., Brüggen M., 2017, MNRAS, 464, 4448

Young A. H., et al., 2015, ApJ, 809, 185

de Gasperin F., Ogrean G. A., van Weeren R. J., Dawson W. A., Brüggen M., Bonafede A., Simionescu A., 2015, MNRAS, 448, 2197

de Gasperin F., et al., 2017, Science Advances

van Haarlem M. P., et al., 2013, A&A, 556, A2

van Weeren R. J., Röttgering H. J. A., Brüggen M., Hoeft M., 2010, Science, 330, 347

van Weeren R. J., Röttgering H. J. A., Brüggen M., 2011a, A&A, 527, A114

van Weeren R. J., Hoeft M., Röttgering H. J. A., Brüggen M., Intema H. T., van Velzen S., 2011b, A&A, 528, A38

van Weeren R. J., Röttgering H. J. A., Intema H. T., Rudnick L., Brüggen M., Hoeft M., Oonk J. B. R., 2012, A&A, 546, A124

van Weeren R. J., et al., 2016a, ApJS, 223, 2

van Weeren R. J., et al., 2016b, ApJ, 818, 204

van Weeren R. J., et al., 2017, Nature Astronomy, 1, 0005

4 Evolutionary phases of merging clusters as seen by LOFAR

– Amanda Wilber, Marcus Brüggen, Annalisa Bonafede, David Rafferty, Timothy W. Shimwell, Reinout J. van Weeren, Hiroki Akamatsu, Andrea Botteon, Federica Savini, Huib Intema, Lennart Heino, Virginia Cuciti, Rossella Cassano, Gianfranco Brunetti, Huub J. A. Röttgering, Francesco de Gasperin –

Astronomy & Astrophysics, accepted on 22 August 2018

Abstract

Massive, merging galaxy clusters often host giant, diffuse radio sources that arise from shocks and turbulence; hence, radio observations can be useful for determining the merger state of a cluster. In preparation for a larger study, we selected three clusters – Abell 1319, Abell 1314, and RXC J1501.3+4220 (Z7215) – making use of the new LOFAR Two-Metre Sky Survey (LoTSS) at 120-168 MHz, and together with archival data, show that these clusters appear to be in pre-merging, merging, and post-merging states, respectively. We argue that Abell 1319 is likely in its pre-merging phase, where three separate cluster components are about to merge. There are no radio haloes nor radio relics detected in this system. Abell 1314 is a highly disturbed, low-mass cluster that is likely in the process of merging. This low-mass system does not show a radio halo, however, we argue that the merger activates mechanisms that cause electron re-acceleration in the large 800 kpc radio tail associated with IC 711. In the cluster Z7215 we discover diffuse radio emission at the cluster centre, and we classify this emission as a radio halo, although it is dimmer and smaller than expected by the radio halo power versus cluster mass correlation. We suggest that the disturbed cluster Z7215 is in its post-merging phase. Systematic studies of this kind over a larger sample of clusters observed with LoTSS will help to constrain the timescales involved in turbulent re-acceleration and the subsequent energy losses of the underlying electrons.

4.1 Introduction

In the process of the hierarchical formation of structure in the Universe, clusters of galaxies merge to form more massive clusters (see Kravtsov & Borgani, 2012, for a review). Cluster mergers are violent phenomena, releasing large amounts of energy ($\sim 10^{63}$ erg) into the intra-cluster medium (ICM). A merging system of galaxy clusters goes through three main evolutionary phases in a period of about one gigayear: a pre-merging phase in which the galaxy clusters have begun their infall and the intracluster media begin to interact, a merging phase in which core passage occurs, and a post-merging phase in which the ICM relaxes as shocks and turbulence begin to dissipate. The avenues of this energy release are not well understood and concern fundamental properties of dilute, magnetised plasmas.

Customarily, X-ray observations are used to classify clusters of galaxies as either merging or non-merging. Merging clusters are identified by morphologically disturbed thermal Bremsstrahlung emission from the ICM while non-merging clusters typically have a relaxed morphology and compact cool cores (e.g. Molendi & Pizzolato, 2001). Several disturbed, massive clusters have been observed to host cluster-scale sources of radio synchrotron emission. Such sources come in two forms: radio haloes, which are diffuse, unpolarised sources that fill most of the inner volume of clusters; and radio relics, which are elongated, polarised sources found in the cluster outskirts. Radio haloes and relics typically exhibit a steep synchrotron spectrum ($\alpha < -1$ where $S \propto \nu^{\alpha}$), have low surface brightness, and are usually of the order of 500 kpc to 1 Mpc in size (see Feretti et al., 2012, for a review). The origins of radio haloes and relics and the acceleration mechanisms of the cosmic-ray electrons that power these sources are still under debate (see Brunetti & Jones, 2014, for a review).

Radio haloes are thought to be powered by turbulent re-acceleration of electrons. In this scenario, turbulence generated by a cluster merger re-accelerates mildly relativistic electrons in situ (Petrosian, 2001; Brunetti et al., 2001, 2008). These cosmic-ray electrons then produce synchrotron radiation at radio frequencies within the cluster magnetic field, which is of the order of a few μG (Carilli & Taylor, 2002). The specific radio luminosities of haloes observed at 1.4 GHz range between about 10^{23} [W Hz^{-1}] and 10^{25} [W Hz^{-1}]. Haloes usually occur in isolation with the exception of the double radio haloes in the pre-merging cluster pair Abell 399–401 (Murgia et al., 2010) and Abell 1758N–A1758S (Botteon et al., 2018). Radio haloes have a smooth brightness distribution that roughly follows the distribution of the thermal ICM; however, some haloes with irregular morphologies have been found (e.g. Giacintucci et al., 2009; Giovannini et al., 2011). Some radio haloes exhibit exceptionally steep spectra, where $\alpha \sim -2$. These ultra-steep spectrum radio haloes (USSRHs) may originate from low-mass mergers where the energy budget for turbulent re-acceleration is smaller, or when the radio halo starts to fade at a later evolutionary stage. A prominent example of such a USSRH is that discovered in Abell 521 (Brunetti et al., 2008; Dallacasa et al., 2009).

Questions remain concerning the particle acceleration efficiency of this turbulence, the source of mildly relativistic seed electrons that must already fill the ICM before they are re-accelerated, and the origin and amplification of the cluster magnetic field. A handful of unusual clusters offer interesting insights into these questions. For example, cluster-scale diffuse radio emission has been seen in some cool-core, relaxed clusters (e.g. Bonafede et al., 2014). Furthermore, not all merging systems show radio haloes and only upper limits for the diffuse radio flux are known (e.g. Brunetti et al., 2007). The fraction of clusters that host radio haloes provide fundamental input for theory (Cassano et al., 2010). Radio relics are more direct indicators of merger activity as they are thought to trace merger-induced shocks. The position of the radio relics with respect to other cluster components, such as galaxies and dark matter, can help to reconstruct the geometry of the merger (e.g. Golovich et al., 2018).

Another way to assess the merging state of clusters is to examine the interplay between the radio lobes of active galactic nuclei (AGNs) and the ICM. Active radio galaxies are suspected to contribute a population of relativistic electrons to their surrounding medium, which may provide a portion of the seed electrons needed to explain diffuse ICM radio sources. An example of such is the connection between a radio relic and a radio galaxy in Abell 3411-3412 (van Weeren et al., 2017). Extended radio galaxies, with sizes $\geq$ 700 kpc, may serve as large suppliers of these seed electrons (e.g. Wilber et al., 2018a). Injection of seed electrons from AGNs can also be studied by looking at remnant radio galaxies, which are radio galaxies in the phase after which nuclear activity has ceased (e.g. Brienza et al., 2017; Brunetti & Jones, 2014). For radio galaxies with intermittent activity, this remnant, or fossil, emission may appear as fading lobes that are visibly detached from an active AGN core. Radio galaxies moving through the cluster environment may also experience ram pressure that results in a bent-tail (BT) morphology (Miley, 1980). Studying the output of radio AGNs within cluster environments is crucial to understanding the characteristics of the ICM.

In recent years, the LOw Frequency ARray (LOFAR) has been a key instrument used to study faint cluster-scale radio sources associated with merging galaxy clusters. The LOFAR instrument is a low-frequency radio interferometer with a compact core in the Netherlands and stations presently located in six other European countries (van Haarlem et al., 2013). The LOFAR Two-Metre Sky Survey (LoTSS; Shimwell et al., 2017) is a new low-frequency survey aiming to map the entire northern sky. When completed, it will be two orders of magnitude deeper in point-source sensitivity and one order of magnitude higher in resolution than any current very large radio survey at this frequency regime (Shimwell et al., 2019). The first 600 pointings (20% of the total) of this survey have recently been observed, covering the 120–168 MHz band using high-band antennas (HBAs). The LOFAR instrument has already yielded valuable insights into radio haloes. These include the observation of intricate and filamentary structures embedded in a radio halo (Shimwell et al., 2016a), the discovery of a new USSRH (Wilber et al., 2018a), the detection of extended radio emission in two cool-core clusters (Savini et al., 2019), and the observation of a tentative bridge of emission connecting two radio haloes (Botteon et al., 2018).

Theoretical studies have predicted that LOFAR will detect many more radio haloes, especially haloes with ultra-steep spectra ($\alpha \leq -1.5$) since these objects appear brighter at lower frequencies (e.g. Brunetti et al., 2008; Cassano et al., 2012). Studies of galaxy clusters made with observations from the Giant Metrewave Radio Telescope (GMRT), operating in a frequency range of 150 MHz to 1.4 GHz, have already revealed that radio haloes can change in brightness and morphology depending upon the observing frequency and that some radio haloes are only visible at lower frequencies (e.g. Venturi et al., 2007, 2008; Kale et al., 2015).

We report on our search for cluster-scale diffuse radio emission associated with three merging cluster systems: Abell 1314, Abell 1319, and RXC J1501.3+4220 (referred to as Z7215 hereafter). In preparation for a larger study, which will consist of LOFAR observations of many merging clusters, we selected these three clusters since they were already covered by LoTSS and appeared to host potential diffuse emission upon first inspection of preliminary images. These three clusters represent a small set of lower mass mergers that are likely at different evolutionary stages. We aim to determine the nature of the radio emission in these clusters and relate this to their merger phase. Hereafter we use the cosmology $H_0 = 69.6$, $\Omega_m = 0.286$, and $\Omega_\Lambda = 0.714$.

4.2 Methods

4.2.1 LOFAR observations and data reduction

The 8 hr LOFAR observations we report in this paper were made as part of LoTSS (Shimwell et al., 2017) over a frequency range of 120-168 MHz using the Dutch HBAs. The data reduction steps for these data are identical to the steps detailed in Wilber et al. (2018a,b), but are also reiterated below.

4.2.1.1 Prefactor

Prefactor[1] is a package containing automated pipelines called Pre-Facet-Calibration and Initial-Subtract. Pre-Facet-Calibration compresses and averages the original data and performs the initial direction-independent calibration (see de Gasperin et al. (2019) for details). In this step a flux calibrator (observed at the beginning and end of the target observation) was used to compute amplitude gain solutions, station clock offsets, station phase offsets, and station differential total electron content (dTEC). Amplitude gain solutions and corrections for clock and phase offsets were then transferred to the target field data. An initial phase calibration was also performed using a global sky model from the TIFR GMRT Sky Survey (TGSS) at 150 MHz (Intema et al., 2017). The calibrator 3C196, which is a bright quasar (66 Jy at 159 MHz according to the Scaife & Heald 2012 absolute flux scale) was used for the observations of all three of our selected clusters. After the direction-independent calibration was completed, preliminary imaging was carried out via the Initial-Subtract pipeline. The full wide-field of the calibrated target data was imaged in high and low resolution using `WSClean` (Offringa et al., 2014). These full-field images were used to model and subtract all sources in preparation for direction-dependent calibration.

4.2.1.2 FACTOR

Direction-dependent calibration for our LoTSS data was carried out through the facet calibration technique (van Weeren et al., 2016). This method of calibration is executed via the FACTOR[2] software package. FACTOR tesselated the full target field into several smaller portions of sky called facets, where each facet is automatically chosen to be centred on a bright compact source to be used as a facet calibrator. The TEC, phase, and amplitude solutions were computed from the facet calibrator and applied to all the sources in that facet. Facets were processed in order of brightness, and all facet sources were subtracted from the *uv*-data before processing the next facet. This method reduced the effective noise in subsequent calibration steps. The target facet, containing the cluster of interest, was appointed as the last facet in the processing list, such that all other nearby and bright sources were already calibrated and subtracted. The calibration region for the target facet was chosen either as the cluster centre, containing multiple sources, or as a single bright, compact source near the cluster centre. More details on facet calibration are provided in van Weeren et al. (2016), Shimwell et al. (2016b), and Williams et al. (2016).

---

[1] https://github.com/lofar-astron/prefactorhttps://github.com/lofar-astron/prefactor

[2] http://www.astron.nl/citt/facet-doc/

4.2.2 LOFAR imaging

The final FACTOR-calibrated data of all three clusters were imaged and analysed with CASA tools (Common Astronomy Software Applications; McMullin et al., 2007). To lower the resolution and increase the sensitivity to diffuse radio emission on large scales, we used the CASA task CLEAN and chose an increased outer *uv*-taper of up to 30 arcsec and Briggs' robust values of -0.25 or 0. Final images made in CASA were also corrected for the LOFAR station beam. The error in our flux density measurements are assumed to be 10%, which was determined by comparing flux densities of several sources in our LOFAR map to the same sources in TGSS (Intema et al., 2017) and the 7C survey (Hales et al., 2007). In the following subsections we describe the basic steps of data manipulation and imaging that were made on our LOFAR measurement sets.

4.2.2.1 Subtraction of compact sources

To accurately measure diffuse radio emission at the cluster centre, we used an image made after subtracting compact radio sources. Compact sources are usually found within the vicinity of the cluster centre and are typically associated with AGN. Hence, the scale of the compact emission we wish to subtract is of the order of < 200 kpc. A compact-source image was made using the task CLEAN in CASA by selecting a specific *uv*-range that corresponds to emission on a projected scale of > 200 kpc. Based on the redshift of the individual clusters, the *uv*-cut was made at 800λ for Abell 1314 and 4500λ for Abell 1319 and Z7215. The model components from this compact-source image were then subtracted from the measurement set using tasks FTW and UVSUB. We then re-imaged the source-subtracted data set with a *uv*-range of $> 80\lambda$, and used an increased outer *uv*-taper of 30 arcsec to bring out diffuse emission.

If diffuse emission was present at the cluster centre, we measured the flux density of this diffuse emission contained within 2σ or 3σ contours. From this flux density we calculated a power at 144 MHz considering the redshift of the cluster, and we extrapolated this power to 1.4 GHz with a spectral index of $\alpha = -1.3$. This power at 1.4 GHz is used to give a relative comparison to the power in the correlation for radio halo power versus cluster mass (referred to hereafter as the $P - M$ correlation) from Cassano et al. (2013).

4.2.2.2 Injection of mock halo

For the massive, merging cluster Z7215, we followed a previously used method of injecting a fake radio halo into the visibilities. This method has been typically used to compute upper limits to the diffuse emission of clusters without radio haloes (e.g. Venturi et al., 2008; Kale et al., 2013, 2015; Bonafede et al., 2017). These studies showed that the flux density of the injected radio halo is only partly recovered and this effect becomes relatively more important for fainter haloes. Since we detected faint diffuse emission at the centre of Z7215 (see section 4.3.3) we used the injection procedure to evaluate the effect of such losses in the measurement of this diffuse flux (e.g. Brunetti et al., 2007; Venturi et al., 2008; Bonafede et al., 2017; Cuciti et al., 2018). Although Abell 1314 is a highly disturbed cluster (as seen by X-ray observations), detectable emission is not expected in such a low-mass system ($M_{500} < 10^{14}$ $M_{\odot}$) owing to energy limitations (e.g. Cassano & Brunetti, 2005; Cassano et al., 2006; Cassano, 2010; Bernardi et al., 2016). Therefore, we decided not to implement halo injection for Abell 1314.

Following these methods, we simulated a radio halo by injecting a radio source into the *uv*-data that has a central brightness I_0 and an e-folding radius of r_e (Murgia et al., 2009). The length scale, r_e, is defined as the radius at which the brightness of a radio halo drops to I_0/e, and measuring this is independent of the sensitivity of the radio images[3]. The model of this mock radio halo was Fourier transformed into the visibility data (MODEL_DATA column), taking into account the w-projection parameter (Cornwell et al., 2005). A relatively empty region near the cluster centre, void of bright sources and artefacts, was chosen to host the injected flux. The data set was then re-imaged with an outer *uv*-taper of 30 arcsec. We considered the injected halo detected when it was recovered above 2σ contours with a diameter of roughly $3r_e$.

4.2.3 Supplementary observations

4.2.3.1 GMRT observations of Abell 1314

Archival GMRT data at 235 and 610 MHz (Obs ID: 7909) centred on the cluster Abell 1314 were obtained and reprocessed with the SPAM pipeline (see Intema et al., 2017, for details). We used the 610 MHz data with our LOFAR data at 144 MHz to produce a spectral index map of the sources in Abell 1314[4]. To produce the spectral index map, we imaged the cluster at both frequencies using the same clean settings in CASA clean: *uv*-range $> 200\lambda$, uniform weighting, and a *uv*-taper of 40 arcsec. We re-gridded the LOFAR map to the 610 MHz GMRT map and smoothed the images to give the same beam size (47 arcsec × 35 arcsec).

---

[3] Bonafede et al. (2017) compared the values of RH and re found by Cassano et al. (2007) and Murgia et al. (2009) for the eight clusters in common in their samples and found that the median value of the ratio R_H/r_e is 2.6.

[4] The 235 MHz image was not useful for our multi-frequency analysis.

4.2.3.2 X-ray observations

Shallow *XMM-Newton* observations (Obs ID: 0149900201 and 0402250201, raw exposure times = 18 and 27.2 ksec, respectively) were used to characterise the thermal ICM emission in Abell 1314 and Z7215, respectively. The SAS v15.0 and the built-in extended source analysis software (ESAS) were used to process and calibrate the data obtained with the *XMM-Newton* European Photon Imaging Camera (EPIC). Following a standard procedure, the raw data were created by *emchain*, and the light curves were extracted and screened for time-variable background components by the *mos-filter, pn-filter* task. The total exposure time after screening was 16.9 ks, 17.0 ks, and 12.9 ks for MOS1, MOS2, and pn, respectively, for the Abell 1314 (0149900201) observation. The total exposure time after screening was 25.6 ks, 25.4 ks, and 21.6 ks for MOS1, MOS2, and pn, respectively, for the Z7215 (0402250201) observation.

Abell 1319 was observed with Chandra ACIS-S for 9.91 ks (Obs ID: 11760) and Z7215 was observed with the Chandra ACIS-I VFAINT mode for 13ks (Obs ID: 7899). We processed the Chandra data following Vikhlinin et al., 2005[5]. The background was examined in the 0.5–7 keV band to search for high proton flares. For the final exposure corrected image we used a binning of 1 arcsec pixel^{-1}. More details are provided in Vikhlinin et al. (2005).

By analysing the surface brightness of the X-ray thermal emission of the ICM, we computed morphological parameters indicative of the merging status of the cluster. The centroid shift parameter, w, is defined as the projected separation between the peak and centroid of the X-ray surface brightness distribution when the aperture used to compute this parameter decreases from the aperture radius, $R_{ap} = 500$ kpc, to smaller radii (Böhringer et al., 2010). The concentration parameter, c, is defined as the ratio of the X-ray surface brightness within a radius of 100 kpc over X-ray surface brightness within a radius of 500 kpc (Santos et al., 2008). The c-w morphological diagram adapted from Cuciti et al. (2015) is shown in Fig. 4.1. The parameters c and w are anti-correlated; relaxed clusters lie on the top left region and merging clusters lie on the bottom right region. The boundary lines are taken from Cassano et al. (2010) and defined at $w \sim 0.012$ and $c \sim 0.2$, such that larger values of w and smaller values of c indicate a disturbed, merging cluster (Cassano et al., 2016). Our computed values for w and c for each cluster are listed in Table 4.1 and shown in the diagram in Fig. 4.1

---

[5] We used CIAO v4.6 and CALDB v4.7.2.

Table 4.1: Our selected clusters observed by LOFAR. The mass listed for Abell 1319 and Z7215 are SZ mass-estimates from Planck (Planck Collaboration et al., 2014). The last three columns give the characteristics of a radio halo falling on the $P-M$ correlation from Cassano et al. (2013) for a cluster corresponding to that mass. We use these correlation values to compare to the diffuse emission detected by LOFAR. (1): Our mass-estimate from *XMM-Newton* observations and scaling relations from Reichert et al. (2011). Since this cluster is at such a low mass, the $P-M$ correlation is not applicable. (2): w and c parameters are computed for Abell 1319-A only.

Cluster name (Obs ID)	RA, dec J2000	Redshift z	Scale kpc arcsec^{-1}	Mass [10^{14} M$_\odot$]	Dynamics $w_{500\ \mathrm{kpc}}$, $c_{100\ \mathrm{kpc}}$	Halo P$_{1.4\ \mathrm{corr}}$ log$_{10}$ [W Hz^{-1}]	R$_{\mathrm{H\ corr}}$ [kpc]	r$_e$ [kpc]
Abell 1314 (L229509)	11h34m50.5s, +49d03m28s	0.0335	0.672	$0.68^{(1)}$ Low	0.063 ± 0.003, 0.026 ± 0.01	N/A	N/A	N/A
Abell 1319 (L403936)	11h34m13.2s, +40d02m36s	0.2906	4.395	$4.79^{+0.51}_{-0.49}$ Intermediate	0.013, $0.148^{(2)}$	23.80	351	135
RXC J1501.3+4220 – Z7215 – (L371804)	15h01m23.0s, +42d20m40s	0.2917	4.406	$5.87^{+0.42}_{-0.41}$ Intermediate	0.096 ± 0.06, 0.052 ± 0.09	24.13	422	162

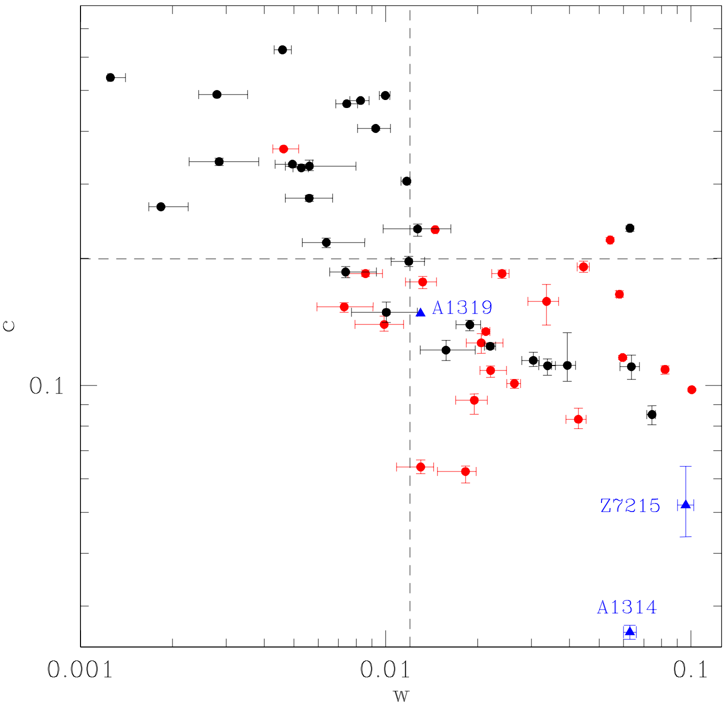

Figure 4.1: Sample of clusters with masses $> 6 \times 10^{14}$ $M_\odot$ plotted by their concentration parameter c vs. their centroid shift w from Cuciti et al. (2015). Red dots indicate clusters hosting radio haloes and black dots indicate clusters without radio haloes. The three blue points represent Abell 1314, Abell 1319, and Z7215. The w and c parameters of all clusters are computed from Chandra X-ray images, except for Abell 1314 and Z7215, which have parameters computed from *XMM-Newton* images. Our selected clusters have masses lower than the sample from Cuciti et al. (2015).

4.3 Results

Abell 1319 and Z7215 were detected by the Planck satellite (Planck Collaboration et al., 2014) via the Sunyaev-Zel'dovich (SZ) effect and have SZ-derived mass estimates (listed in Table 4.1). Abell 1314 was not detected by Planck, but the most recent mass estimate of Abell 1314, from MCXC (Meta-Catalogue X-ray galaxy clusters; Piffaretti et al. 2011), is $M_{500} = 0.4608 \times 10^{14}$ $M_\odot$, suggesting that this cluster has a very low mass. We report new radio emission detected by LOFAR in the low-mass cluster Abell 1314, and we derive a mass estimate from *XMM-Newton* X-ray observations. We also report new diffuse radio emission detected by LOFAR in the intermediate-mass cluster Z7215. Table 4.1 lists the individual details for our three selected clusters. In this paper we hypothesise the merging status of each cluster based on a joint radio-X-ray analysis and suggest that each cluster represents one of the three evolutionary phases of merging systems: Abell 1319 in a pre-merging phase, Abell 1314 in a merging phase, and Z7215 in a post-merging phase.

4.3.1 Abell 1319: Example of a pre-merging system

In Fig. 4.2 we present an overlay of Chandra X-ray and LOFAR radio emission on a Sloan Digitial Sky Survey (SDSS) optical image of the cluster Abell 1319. This image of the cluster shows three ICM components. The main component is Abell 1319-A, and the two additional ICM components, to the northwest (Abell 1319-B) and southwest (Abell 1319-C), show coincident galaxies with spectroscopic redshifts (from the SDSS database) similar to that of the galaxies in Abell 1319-A.

In Fig. 4.3 Planck contours are overlaid on a X-ray image of Abell 1319 from ROSAT. All three ICM clumps are included in the Planck contours. Therefore, it is likely that the SZ-derived mass-estimate from Planck ($\mathrm{M}_{500} = 4.79^{+0.51}_{-0.49} \times 10^{14}\ \mathrm{M}_{\odot}$) is the mass of the total system, including all three ICM components. Although the Chandra image shows the southwest clump, Abell 1319-C, as being the most faint, ROSAT shows this component to be the brightest of the three, but this effect could be due to differences in the pointing and exposure times of the two separate observations. Abell 1319-C also lies near the CCD edge of the Chandra observation. We did not estimate the mass values of each individual cluster component.

Our LOFAR image of this multi-component system shows compact radio emission at the centre of each ICM. These are likely to be the radio AGN of bright central galaxies (BCGs). The optical overlay shows that the galaxies coincident with these compact central radio sources are all at similar redshifts. A more extended radio galaxy is seen on the eastern edge of Abell 1319-C. This emission is likely a BT radio galaxy from within the cluster (north) and a background radio galaxy (south) appearing in projection to be one extended source. After compact-source subtraction and *uv*-tapering to lower the resolution of our LOFAR image, no diffuse sources appear to be present at the ICM centres nor on the ICM edges. We do not estimate upper limits for diffuse emission at the centre of each ICM component because residual AGN emission from the BCGs is too prominent for a reliable subtraction. We also cannot compare the residual emission to the $P - M$ correlation since we do not have the individual mass estimates for each clump, and each clump likely has a mass lower than cluster masses tested in the $P - M$ correlation.

Since the active BCGs all appear to reside in their respective ICM centres, and since no radio haloes or radio relics are detected in this system, we suggest that this multi-component system is in a pre-merging state, i.e. the separate ICM components are in gravitational infall, but have not yet merged. The centroid shift and the concentration parameter for Abell 1319-A, the eastern clump, also indicate that this ICM component is more relaxed, according to the

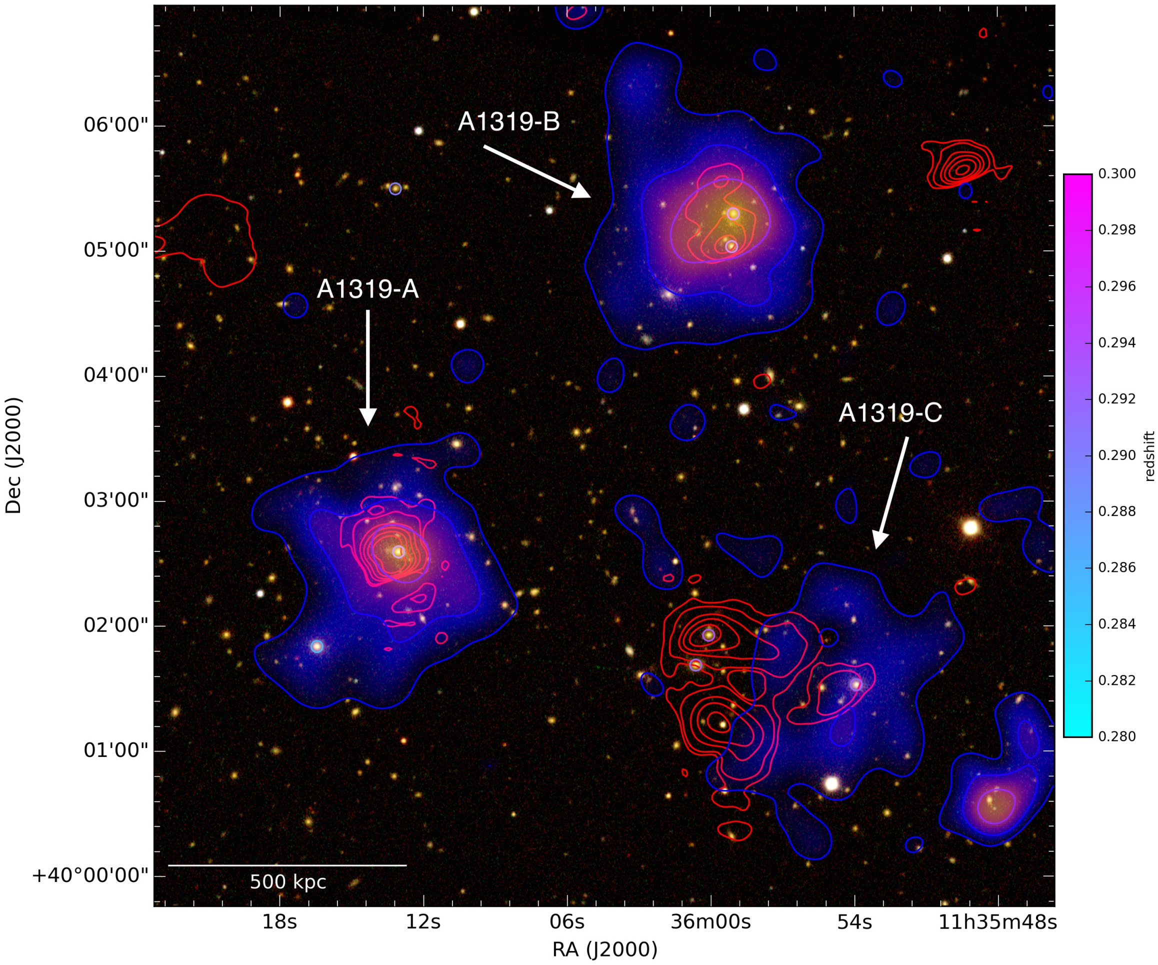

Figure 4.2: SDSS *i,r,g* image of Abell 1319 with LOFAR radio emission overlaid as contours. LOFAR high-resolution emission (11 arcsec × 6 arcsec) is shown by red contours $[3, 5, 16, 64, 128, 256, 512] \times \sigma$ where $\sigma = 170\ \mu\text{Jy beam}^{-1}$. The smoothed Chandra X-ray image is shown in blue-magenta and as blue contours. Cluster galaxies with known spectroscopic redshifts are indicated by coloured rings, where the colour represents redshift.

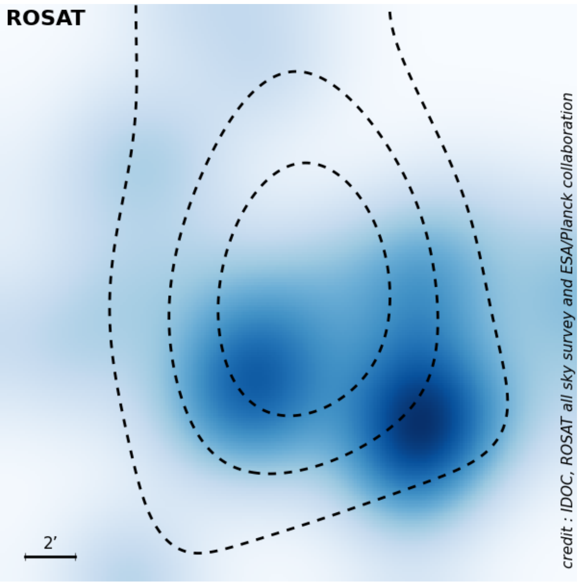

Figure 4.3: This image is taken from the Planck SZ Cluster Database. Abell 1319-A is accompanied by two additional cluster components of similar size at a similar redshift. We suggest the SZ-derived mass is a combination of three low-mass cluster components (faintly visible in blue, as seen by ROSAT).

boundaries on the $w - c$ diagram (with $w = 0.013$, and $c = 0.148$ from Fig. 4.1; also see Cassano et al. 2010; Cuciti et al. 2015; Cassano et al. 2016). These parameters are measured from our Chandra X-ray image of Abell 1319.

4.3.2 Abell 1314: Example of a merging system

Abell 1314 has been studied for several decades with radio telescopes, starting with Webber (1974). There are four IC galaxies in the cluster with radio counterparts. Two BTs, associated with IC 708 and IC 711, were identified in 1976 with the Westerbork telescope at 610 MHz and 5 GHz (Vallee & Wilson, 1976). IC 708 exhibits a wide-angle opening between two tails, both with short extents and radio lobes to the west of the host. IC 711 is a head-tail, or narrow-angle tail, with a single, long radio tail extending hundreds of kpc north of the host galaxy.

Srivastava & Singal (2016) presented GMRT observations at 235, 610, and 1300 MHz of the head-tail IC 711 in Abell 1314. These authors produced a spectral index map over the body of the emission and report a break in the spectrum. They suggest that the morphology of the tail did not form solely from N-S movement from the host galaxy because there is a sharp turn in the emission at the northernmost extent. More recently, Sebastian et al. (2017) presented a low-resolution image from a 240 MHz GMRT observation of the radio tail associated with

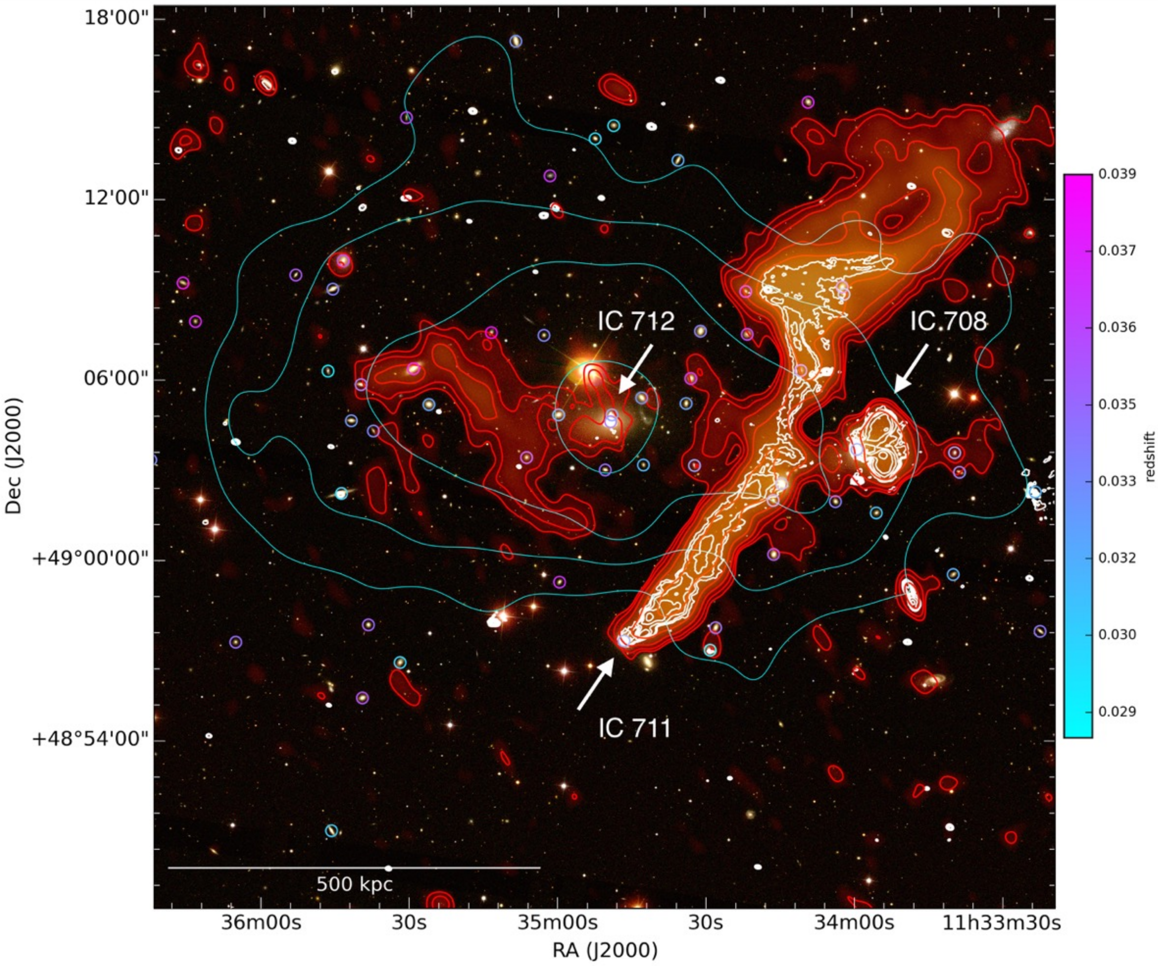

Figure 4.4: SDSS *i,r,g* image of Abell 1314 with radio emission overlaid as contours. LOFAR high-resolution (8 arcsec × 5 arcsec) emission is shown by white contours $[6, 12, 24, 48, 96, 192, 384, 768] \times \sigma$ where $\sigma = 180$ μJy beam^{-1}. LOFAR diffuse emission after compact source subtraction (with a resolution of 43 arcsec × 33 arcsec) is shown in red and red contours where contours are $[3, 6, 12, 24, 48] \times \sigma$ and $\sigma = 300$ μJy beam^{-1}. Smoothed *XMM-Newton* X-ray contours as also shown in cyan. Cluster galaxies with known spectroscopic redshifts are shown by coloured rings, where the colour represents redshift.

IC 711. In this image, it is apparent that there is more emission extending westward at the northernmost region referred to by Srivastava & Singal (2016).

An overlay of our LOFAR images of Abell 1314, in high and low resolution, can be seen in Fig. 4.4. The LOFAR high-resolution (8 arcsec × 5 arcsec) image of Abell 1314 reveals extended tail emission from IC 711. The wide-angle tail IC 708 is also visible to the west of the elongated head-tail. The sharp turn noted by Srivastava & Singal (2016) actually appears to be filamentary emission sweeping westward for ~ 300 kpc. As noted by Srivastava & Singal (2016), this northernmost emission that appears, in projection, perpendicular to the length of the tail likely did not form from the trajectory of the active host galaxy. It is more likely that the radio emission in the northern part of the tail has been disturbed by the ICM, such as ram pressure from turbulence or shocks traveling from the cluster centre outward and toward the west. The LOFAR low-resolution map (shown as red contours and colour in Fig. 4.4) reveals an additional 300 kpc of bulk diffuse emission beyond this high-resolution filamentary portion of the tail, giving a total projected size of 800 kpc.

In our low-resolution LOFAR image, faint diffuse emission is also detected in the central regions of the cluster, which has not been detected at higher frequencies. This emission is not spherically uniform in shape or brightness, but instead exhibits “arms”. It is possible that this emission is remnant AGN emission from the central BCG (IC 712: $z = 0.033553$, which shows a compact core) or from other radio galaxies within the cluster centre.

4.3.2.1 Spectral index on radio emission

A spectral index map is generated along the head-tail radio galaxy IC 711 by comparing the GMRT map at 610 MHz to our LOFAR map at 144 MHz. The spectral index along the tail steepens from south to north, but there is a region of flattening that takes place in the central part of the tail. The index goes from $\alpha \sim -2$ to -1.3 and then back to ~ -2 within this region. A compact source is also seen to the northeast edge of the tail emission, marked by a flat spectral index, but this is likely to be a foreground source. The spectral index in the northernmost portion of the tail, where emission sweeps westward, cannot be determined since this emission is not detected by the archival GMRT observations we obtained at 610 nor 235 MHz.

To determine an upper limit on the spectral index of the diffuse emission at the cluster centre, we compare the flux density within 3σ contours in our 144 MHz LOFAR map to the same

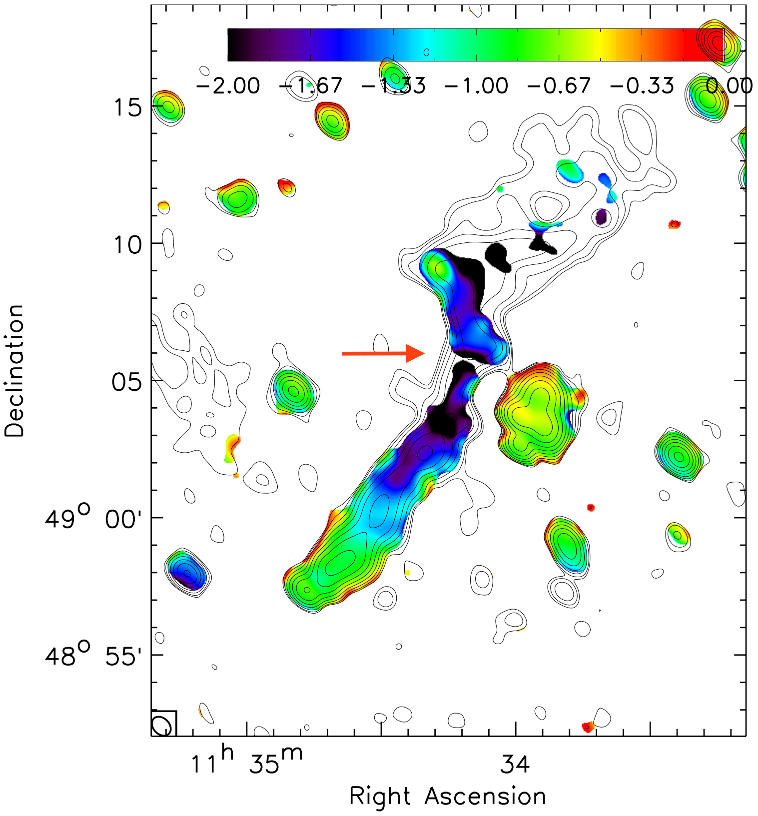

Figure 4.5: Spectral index map over the BT galaxies in Abell 1314. The map is made with the LOFAR map at 144 MHz and the GMRT map at 610 MHz. Both maps are imaged with the same setting and convolved to the same beam size. We indicated no RA, dec offset between the two maps. The radio head-tail from IC 711 shows steepening in the length of the tail with a portion of flattening in the mid-section. A red arrow roughly marks where the flattening of the spectral index occurs.

region of the 610 MHz GMRT map[6]. This flux density within this region is only at noise level at 610 MHz, so we integrate the noise (300 μJy beam^{-1}) over the area of the 3σ contour region from the LOFAR map and find the upper limit on the flux density to be 19.4 mJy at 610 MHz. Comparing the measurements gives a spectral index upper limit estimate of $\alpha < -1.3$.

4.3.2.2 Central diffuse radio emission

The non-spherical, limb-like emission at the centre of Abell 1314, with a largest linear size of $\sim$ 380 kpc, is probably not related to a cluster radio halo. The flux density of the central diffuse emission is measured in our compact-source-subtracted image made with a *uv*-taper of 30 arcsec. The flux density within 3σ contours where $\sigma = 400$ μJy beam^{-1} is 109 ± 11 mJy. This translates to a power of $(2.85 \pm 0.29) \times 10^{23}$ W Hz^{-1} at 144 MHz and $(1.48 \pm 0.15) \times 10^{22}$ W Hz^{-1} at 1.4 GHz if extrapolated assuming a spectral index of $\alpha = -1.3$. This power of $\log_{10}(\mathrm{P}_{1.4}$ / W Hz$^{-1}) = 22.17$ is much lower than the power of radio haloes even at the lowest end of the cluster mass range (see the $P - M$ correlation from Cassano et al. (2013) and Martinez Aviles et al. (2016)). As we discuss in Sec. 4.4.2, it is more plausible that this emission is a remnant radio galaxy.

4.3.2.3 X-ray results on Abell 1314

Fig. 4.6 shows the 0.3–2.0 keV X-ray band image of Abell 1314 obtained with *XMM-Newton* together with LOFAR high-resolution radio contours. As is clear from Fig. 4.6, Abell 1314 shows an elongated and disturbed morphology indicating that it is still at a dynamically young state.

Using *XMM-Newton* MOS data, we characterised the dynamical state of cluster and investigate the relationship between thermal (ICM) and non-thermal (radio) components. We derived the morphological parameters ($c_{100\ \mathrm{kpc}}$ and $w_{500\ \mathrm{kpc}}$) as 0.063 ± 0.003, 0.026 ± 0.01, respectively. The morphological parameters of Abell 1314 are in good agreement with those observed for merging clusters (see Fig. 4.1); however, we note that the values for Abell 1314 are computed from XMM data whereas the values of other clusters we use for comparison are computed from Chandra data. XMM has a larger point spread function (PSF), and this is taken into account in the errors on w and c.

---

[6] We compare the images made with the same clean settings including uniform weighting and the same beam size.

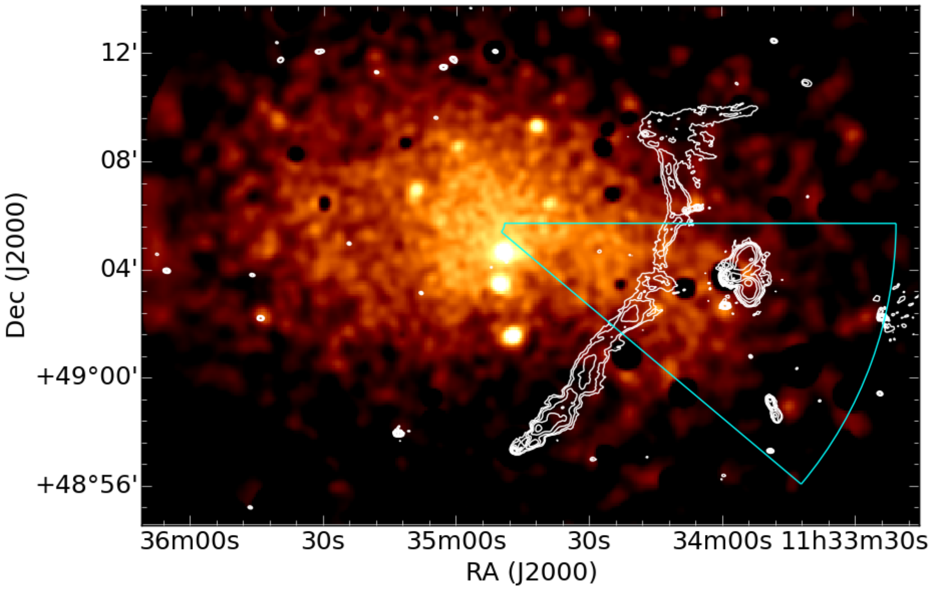

Figure 4.6: *XMM-Newton* map of Abell 1314 with LOFAR high resolution overlaid as white contours $[6, 12, 24, 48, 96, 192, 384, 768] \times \sigma$ where $\sigma = 180\ \mu$Jy beam^{-1}. The cyan region indicates where the surface brightness is analysed along the length of the tail, starting from the cluster centre and going to a radius of 600 kpc.

For the surface brightness profile, we used 0.3–2.0 keV energy range and fitted it with the PROFFIT software package (Eckert et al., 2011). We extracted the surface brightness profile in the western sector with an opening angle of 40 degrees (covering the full region where the spectral index is seen to flatten). The resulting surface brightness profile is shown in the Fig. 4.7. The discontinuity in *XMM-Newton* surface brightness profile is clearly visible. The location of the discontinuity around $r{\sim}10'$, is just outside of the BCG, IC 712. In order to characterise the discontinuity, we assume that the gas density follows two power-law profiles connecting at a discontinuity with a density jump. The density profile was projected onto the line of sight with the assumption of spherical symmetry. All the parameters of the model were let free in the fit. The surface brightness profile was well fitted with the above model (reduced $\chi^2 = 1.16$ for 32 degrees of freedom). The best-fitting broken power-law model is shown in Fig. 4.7. The compression factor and the location of the discontinuity are $C = 2.1 \pm 0.2$ and $r = 10.8 \pm 0.3$ arcmin, respectively.

Since the discontinuity is located near the edge of the field of view of the MOS instrument, the determination of the instrumental background might be inaccurate. We investigate the impact of this systematic effect by changing the normalisation of the instrumental background ±20%[7]. The effect of the systematic error on the location of the discontinuity and the com-

---

[7] We use a conservative, and likely overestimated, error value of 20% and note that the results and conclusion do not change with or without the systematic error.

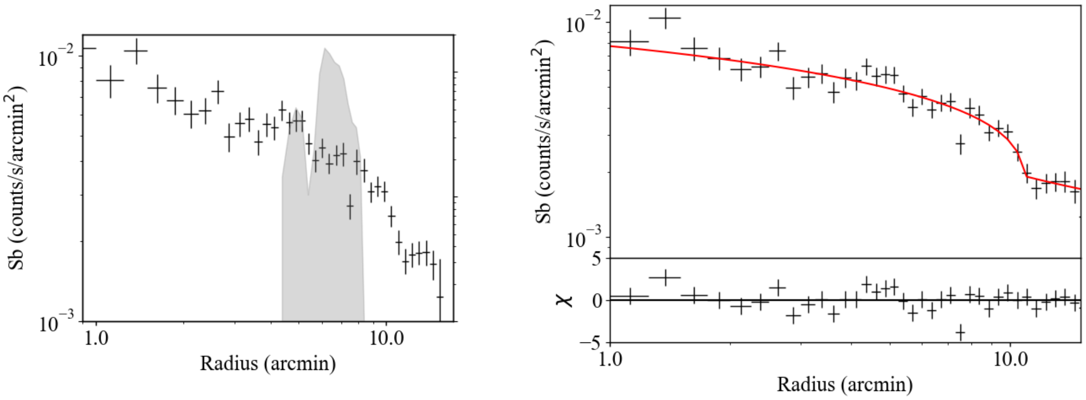

Figure 4.7: Left: *XMM-Newton* 0.3 - 2.0 keV band surface brightness profile. The grey shaded area represents the LOFAR radio brightness profile (in arbitrary units). Right: Same as left but with the best-fitting broken power-law model.

pression factor are smaller than or compatible with the statistical errors. In the following discussion section, we used the error defined by $\sigma \equiv \sqrt{\sigma^2_{\rm stat} + \sigma^2_{\rm syst}}$, which leads $C = 2.1 \pm 0.4$ and $r = 10.8 \pm 0.4$ arcmin, respectively.

Since Abell 1314 is not detected by Planck, we must estimate its mass from X-ray data. We estimate the mass of Abell 1314 from the spectrum of the *XMM-Newton* observation. The 0.5-2.4 keV band flux of Abell 1314 is $F_x = 6.13 \times 10^{-12}$ erg s^1 cm^2. The luminosity distance of Abell 1314 ($z \sim 0.034$) is 150.3 Mpc therefore, the estimated X-ray luminosity is $L_x = 1.7 \times 10^{43}$ erg s^{-1} and the estimated ICM temperature is $kT \sim 1.7$ keV. Our result is in good agreement with the $L_x - T$ relation from Xue & Wu (2000) (Fig. 1 in their paper). With this temperature we estimate the mass with the scaling relation in Reichert et al. (2011), which is based on 14 literature samples, and find $M_{500} \sim 0.68 \times 10^{14} M_\odot$. Our estimated mass is broadly consistent with that from MCXC ($M_{500} = 0.4608 \times 10^{14}$ M$_\odot$; Piffaretti et al. 2011)[8]

4.3.3 Z7215: Example of post-merging system

An overlay of our LOFAR images of the cluster Z7215, in high and low resolution, can be seen in Fig. 4.8. This overlay includes smoothed X-ray contours from Chandra data. According to the Chandra map, the thermal ICM appears to be moderately disturbed and elongated. The cluster does not host a cool core and looks moderately asymmetric. Because of the low counts and the position of the chips we cannot give reasonable estimates of w and c from

---

[8] There is a $\sim 30\%$ difference between our mass estimate and the mass estimate from Piffaretti et al. 2011, which is within the scatter of the $L_x - M$ scaling relationship.

the Chandra data alone. An *XMM-Newton* observation of Z7215 is used instead to estimate values for the centroid shift and concentration parameters, as was done for Abell 1314, but these estimates have larger errors: $w = 0.096 \pm 0.06$ and $c = 0.052 \pm 0.09$. These values and the estimated β parameter of 0.84 ± 0.07 indicate a disturbed morphology. The estimated core radius R_c is 1.29 ± 0.10 arcmin. Considering the distance to this cluster (1 arcmin $\sim$ 260 kpc), the core radius is $\sim$ 350 kpc, which is apparently on the larger side (e.g. Mohr et al., 1999).

The LOFAR image of Z7215 at high resolution does not show many radio sources associated with or located at the cluster centre. A FR-II radio galaxy is seen north of the cluster, coincident with an X-ray source seen by Chandra, but this source is likely in the background since it overlaps galaxies at higher redshifts. After subtracting sources and re-imaging at a lower resolution, diffuse emission is visible above 3σ at the cluster centre, where $\sigma = 450\ \mu$ Jy beam^{-1}. This diffuse emission is coincident with the Chandra X-ray contours at the cluster centre. However, this diffuse emission is not spherical in morphology, and instead appears to be elongated to the west, with a minor axis about half the size of the major axis (about 500 kpc in the N-S direction and 1 Mpc in the E-W direction). There is also a portion of diffuse emission detached from the centre on the N-W edge, but it overlaps several potentially active galaxies, coincides with an X-ray source seen by Chandra, and is also more compact in its extent. We do not include this emission on the northwest edge, which is likely of AGN origin, as part of the central diffuse emission when measuring flux densities and calculating powers in the following subsections.

We discover centrally located diffuse emission in Z7215, which is most likely a radio halo, although it is not spherically uniform in its shape and it is dimmer than expected from the $P-M$ correlation. The flux density of the central diffuse emission is measured in our compact-source-subtracted image made with a *uv*-taper of 30 arcsec (resolution of 43 arcsec × 33 arcsec). The flux density above 2σ contours where $\sigma = 450\ \mu$Jy beam^{-1} is 20.2 ± 2.0 mJy. This translates to a power of $(5.91 \pm 0.60) \times 10^{24}$ W Hz^{-1} at 144 MHz and $(3.07 \pm 0.31) \times 10^{23}$ W Hz^{-1} at 1.4 GHz if extrapolated assuming a spectral index of $\alpha = -1.3$. This power of $\log_{10}(\mathrm{P}_{1.4}$ / W Hz$^{-1}) = 23.49$ is slightly less than the expected power of a halo fitting on the correlation at 1.4 GHz (see Table 4.1), but close to the powers of other radio haloes at this cluster mass (see Fig. 4.9). A 610 MHz observation covering Z7215, as part of the GMRT Radio Halo Survey, was analysed by Venturi et al. (2008), and they found an upper limit for diffuse radio emission at the cluster centre: $\log_{10}(\mathrm{P}_{610}$ / W Hz$^{-1}) = 24.20$. Extrapolating this value to 1.4 GHz with a spectral index of $\alpha = -1.3$ gives $\log_{10}(\mathrm{P}_{610}$ / W Hz$^{-1}) = 23.73$. This value is comparable but slightly larger than the power we extrapolate from our 144 MHz LOFAR observations.

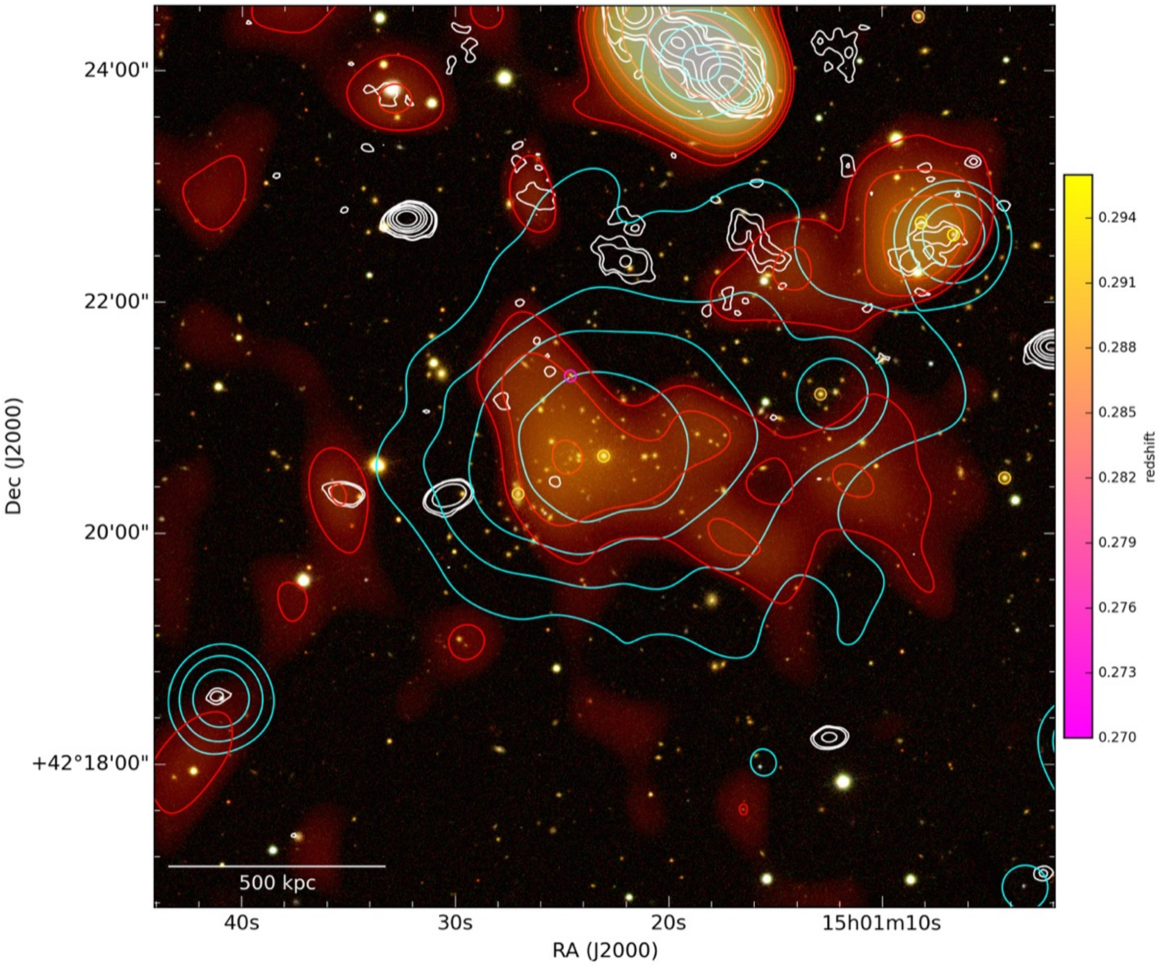

Figure 4.8: SDSS *i,r,g* image of Z7215 with LOFAR radio emission overlaid as contours. The LOFAR high-resolution (10 arcsec × 6 arcsec) emission is shown by white contours $[3, 5, 16, 64, 128, 256, 512] \times \sigma$ where $\sigma = 170$ μJy beam^{-1}. The LOFAR diffuse emission after compact source subtraction (with a resolution of 40 arcsec × 34 arcsec) is shown in red colour and red contours where contours are $[2, 4, 8, 16, 32, 64] \times \sigma$ and $\sigma = 350$ μJy beam^{-1}. Smoothed Chandra X-ray contours are also shown in cyan. Cluster galaxies with known spectroscopic redshifts are marked by coloured rings, where the colour represents redshift.

To test the capability of our LOFAR observation to recover such faint extended emission, we inject a modeled radio halo with a radius R_H determined by the correlations from Cassano et al. (2013) ($R_H = 422$ kpc and $r_e = 162$ kpc for a cluster with $M_{500} = 5.87 \times 10^{14} M_{\odot}$). We inject the mock radio halo in a relatively empty region of the cluster field (at RA, dec: 15h03m04.3s, +42d34m49.4s). The mock halo is initially assumed to have a power and central brightness, I_0, defined by the correlation, and we lower the injected flux until the recovered mock halo emission is comparable to the detected emission at the cluster centre. We measure and compare the recovered flux density of the injected source to the flux density of the diffuse emission at the cluster centre above 2σ and determine at which injected flux value they are approximately equal. The flux density of the recovered halo is measured in our LOFAR low-resolution image[9] above 2σ contours and is found to be 19.3 ± 1.9 mJy. This recovered flux density of the mock halo is about equal, within error, to the central diffuse source. The injected flux value of this halo is 26.3 mJy, and therefore the recovered flux is $\sim 73\%$ of the injected flux. These findings demonstrate that our LOFAR observation is able to partially, but not fully, recover the faint extended emission of this radio halo. Therefore, we conclude that the true flux density of the radio halo in Z7215 is more reasonably approximated by the injected flux density value of the mock halo. We extrapolate this flux density to 1.4 GHz assuming a spectral index of $\alpha = -1.3$ and find a power of 3.99×10^{23} W Hz^{-1}. We compare this power to the power of the detected emission above 2σ and to the powers of a sample of radio haloes, as shown in Fig. 4.9.

4.4 Discussion

4.4.1 Abell 1319

The three ICM clumps, A, B, and C, are separated by a distance of about ~ 500 kpc. It is not likely that this system is post-merger, as we might then expect to see X-ray filaments or an overall elongated, disturbed ICM of the combined components. However, a deeper X-ray observation would be needed to exclude the presence of such filaments. Additionally, if this system was post-merger the ICM of Abell 1319-A would be expected to be more disturbed with a higher w value and a lower c value.

Diffuse cluster-scale sources do not appear in our LOFAR images. We suggest that there are no radio relics or radio haloes associated with this multi-component system. The lack of ICM radio sources lends further support to the hypothesis that this system is in its pre-merging phase since radio relics and radio haloes are reliable tracers of mergers.

---

[9] Made with a uv-taper of 30 arcsec and Briggs' robust parameter of 0.

4.4.2 Abell 1314

Although there is a central diffuse source in this cluster, its morphology, scale, and brightness distribution is unlike that of a cluster radio halo. The power of the central diffuse source lies an order of magnitude below the $P - M$ correlation, even at the low end of the mass range, suggesting that this source is not similar to a radio halo. Indeed, this cluster is considered to have a very low mass, and the $P - M$ correlation has not yet been tested for such low-mass merging clusters. Although Abell 1314 is highly disturbed (see Fig. 4.6 and w, c parameters in Table 4.1), it is not so surprising that a halo is not detectable given the mass estimate we derive. It is possible that the ICM has been re-energised by merger turbulence, but a spherical, cluster-wide halo has not been generated.

One may speculate whether this elongated patch of radio emission is the beginning, or making, of a radio halo, that will develop into a full-scale halo at a later stage. Donnert et al. (2013) used simulations to show that radio haloes are transient sources with an evolving spectrum, and identified three stages of radio/X-ray activity: infall, re-acceleration, and decay. It is unlikely that Abell 1314 is in the re-acceleration phase where a cluster-scale, spherically uniform halo is expected to form. Our deep observations should have revealed such a halo, however, we only detect faint arms of emission at the centre of Abell 1314.

The central diffuse source, which likely has a steep spectrum since it is not detected by GMRT observations at 235 or 610 MHz, (an estimate of the spectral index in Sec. 4.3.2.1 gives $\alpha \sim -1.3$) is similar to the irregular large-scale emission recently discovered in Abell 1931 by Brüggen et al. (2018). In that paper, they report a remnant radio galaxy that is detected by LOFAR at 144 MHz. Another 144 MHz LOFAR observation of the galaxy group MaxBCG J199.31832+51.72503 showed an extended radio galaxy embedded in steep, remnant radio emission at the group's centre (Savini et al., 2018). We may be witnessing a similar phenomena in Abell 1314 where the arms of emission are old, fading remnant lobes of a previous activity cycle from the central BCG AGN. However, there are multiple galaxies at the cluster redshift that reside within this diffuse radio source, hence the radio emission could be a superposition of multiple remnant lobes. A question remains as to whether this diffuse source is simply fading AGN emission, or if this fossil emission has been partially re-accelerated, and therefore slightly re-brightened, by merger turbulence. Without detailed spectral index maps this will be impossible to untangle.

Still, this is yet another example that LOFAR is able to detect old, faded, and faint large-scale radio sources. This fossil radio emission proves that relativistic electrons are filling the inner part of the cluster volume. As LOFAR reveals more and more fossil radio emission from remnant AGN, we may begin to see a clear connection between these sources and ICM cluster-scale sources such as radio haloes (e.g. Wilber et al., 2018a; Brüggen et al., 2018).

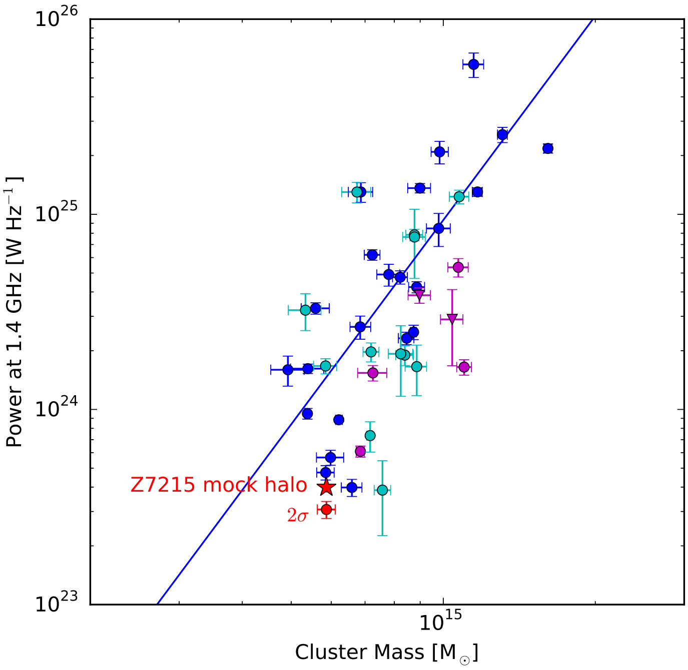

Figure 4.9: Sample of radio haloes plotted by their radio power at 1.4 GHz vs. their cluster mass (M_{500} – as determined from Planck observations). The sample of haloes and their correlation is reproduced from Martinez Aviles et al. (2016). Haloes with flux measured at 1.4 GHz are indicated by blue circles and their derived fit is shown as a blue line. Cyan circles represent haloes with flux measured at frequencies other than 1.4 GHz. Magenta circles represent ultra-steep haloes, and magenta triangles represent ultra-steep haloes with flux measured at frequencies other than 1.4 GHz. The red point shows the power computed from the emission detected in our LOFAR observation for Z7215. The red star indicates the power of our mock halo with a higher injected flux value. All halo powers include a k-correction with an averaged spectral index of $\alpha = -1.3$, as in Martinez Aviles et al. (2016).

IC 711

The extended radio emission produced by the galaxy IC 711 shows a spectral index that generally steepens from the head to the end of the tail (see Fig. 4.5), as is expected of typical head-tail radio galaxies. However, there is a portion of the tail, near the middle, that shows signs of flattening. This flattening likely occurs because the emission in this region is disturbed or compressed. We suggest that the disturbance induces re-acceleration, which causes the electrons to emit at slightly higher energies in this region. In fact, the flattening occurs where there is a concentration of thermal ICM emission, in the same plane of the cluster merger. This flattening is similar to the gentle re-energisation (GReET) phenomena reported by de Gasperin et al. (2017), where the spectral index of a wide-angle-tail (WAT) source is seen to increase where it is expected to decrease.

A small jump can be seen at the location of the radio tail of IC 711 from a radial X-ray surface brightness profile of the cluster. A discontinuity is also seen in the eastward direction (not shown), but there are no significant radio sources on this side of the cluster. It is possible that bulk motions in the ICM distort the tail, which flows perpendicular to the merger direction. The total shape of the tail has a slight arc that is concave with respect to the cluster centre. In the high-resolution image, we see thin filamentary structures in the northern emission of the tail, which appear to be sweeping from east to west. This filamentary emission is even more suggestive of disturbance, such that this sweeping effect may have been produced by turbulence and shocks traveling from the cluster centre to the outskirts. It is impossible to tell whether this northernmost emission has been re-accelerated, or compressed by a shock because there is no radio emission in this region present in our GMRT images and the *XMM-Newton* map is not sensitive enough to detect a jump in temperature or surface brightness in this region. The 240 MHz GMRT image produced by Sebastian et al. (2017) may be helpful to estimate a spectral index in this region, but such an estimate could be unreliable since their observing frequency is close to our LOFAR observing frequency.

4.4.3 Z7215

The power of the diffuse source at the cluster centre is below the $P - M$ correlation, but comparable to the powers of other radio haloes at a similar cluster mass (see Fig. 4.9). It is likely that this diffuse source, elongated in the E-W direction and coincident with the thermal X-ray emission of the cluster, is a radio halo. There are no compact sources seen in our high-resolution LOFAR image that reside within the cluster centre, indicating it is unlikely that the diffuse emission is of AGN origin. The flux density of the central diffuse source in Z7215 (contained within 2σ contours) is roughly equal to the flux density of the emission recovered after injecting a fake radio halo with a flux density of 26.3 mJy at 144 MHz.

Based on our findings, the radio halo in Z7215 is under-luminous. One reason for this could be that the halo is smaller than typical haloes fitting the correlation. Indeed the halo as seen by LOFAR appears shortened in the N-S direction, and we measure an effective radius $R_H = \sqrt{500\text{kpc} \times 250\text{kpc}} \approx 350$ kpc. Another possibility is that the halo is an USSRH. These sources are predicted (Cassano et al., 2010; Donnert et al., 2013) and observed to be typically under-luminous with respect to the correlation (see Fig. 4.9); USSRHs are thought to form in less massive and less energetic merger events or at the beginning or fading evolutionary phase of halo formation (Cassano et al., 2006; Brunetti et al., 2008; Donnert et al., 2013). Since the actual halo radius is smaller than the radius assumed for the upper limit computed by Venturi et al. (2008), the upper limit should be smaller and the resulting spectral index should be steeper. Deeper observations around 330 MHz could help to constrain the spectral index.

This cluster was also on the edge of our LoTSS observation pointing, which may have affected the amount of emission that was detected and recovered. Indeed, only 73% of the injected halo flux was recovered in our LOFAR image. Follow-up observations centred on this cluster are already planned and scheduled with LOFAR. Observations centred on the cluster may reveal more flux associated with the radio halo. Future LOFAR low band antenna observations may also be of interest in conjunction with the HBA observations so that the spectral index could be constrained. In conclusion we claim that this cluster is in its post-merging phase, where the system has begun to relax. The radio halo we discover is under-luminous with respect to the correlation.

4.5 Conclusions

In summary we find following results:

- We show that Abell 1319 is a multiple-component system and suggest that these three low-mass clusters, or galaxy groups, are about to merge. The LOFAR radio observations reveal active BCG galaxies at the centres of all three ICMs. There are no diffuse cluster-scale ICM radio sources present in this system, such as radio relics or radio haloes, which supports the notion that this system is pre-merging.

- Abell 1314 is a low-mass cluster that shows a highly disturbed thermal ICM. Irregularly shaped diffuse radio emission present at the cluster centre is likely to be remnant AGN lobe emission from previous activity cycles of the currently active BCG IC 712. We argue that this cluster is in a merging phase, although it is likely too low of mass to generate a detectable radio halo, even at a later evolutionary stage. The extended head-tail radio galaxy IC 711 shows signs of disturbance. A spectral index map reveals that the middle portion of the tail, where the X-ray brightness is highest along the tail, indicates possible local re-acceleration or compression. The northernmost part of the tail shows filamentary emission that appears to be sweeping westward, suggestive of disturbance.

- We discover a radio halo in the massive, merging cluster Z7215 and we argue that this cluster is in its post-merging phase. The halo has a non-spherical morphology with a major axis of about 1 Mpc and a minor axis of about 500 Mpc. The halo is dimmer than expected by the halo $P - M$ correlation but comparable to the powers of other haloes at similar cluster masses. We suggest that this could be a smaller halo or an ultra-steep spectrum halo. Future follow-ups will distinguish between these possibilities.

Using LOFAR observations to add more clusters to this sample, specifically adding more examples of clusters which are in various stages of merging, would help to strengthen our understanding of how merging mechanisms are related to ICM radio sources.

Acknowledgements

LOFAR, the Low Frequency Array designed and constructed by ASTRON, has facilities owned by various parties (each with their own funding sources), and that are collectively operated by the International LOFAR Telescope (ILT) foundation under a joint scientific policy. The LOFAR software and dedicated reduction packages on https://github.com/apmechev/GRID_LRT were deployed on the e-infrastructure by the LOFAR e-infragroup, consisting of J. B. R. Oonk (ASTRON & Leiden Observatory), A. P. Mechev (Leiden Observatory), and T. Shimwell (Leiden Observatory) with support from N. Danezi (SURFsara) and C. Schrijvers (SURFsara). The data used in work was in part processed on the Dutch national e-infrastructure with the support of SURF Cooperative through grant e-infra 160022 & 160152. We thank the staff of the GMRT who have made these observations possible. The GMRT is run by the National Centre for Radio Astrophysics of the Tata Institute of Fundamental Research. This research made use of the NASA/IPAC Extragalactic Database (NED), which is operated by the Jet Propulsion Laboratory, California Institute of Technology, under contract with the National Aeronautics and Space Administration. AB acknowledges support from the ERC-StG 714245 DRANOEL. RJvW and HJAR acknowledge support from the ERC Advanced Investigator program NewClusters 321271 and RJvW acknowledges the VIDI research program with project number 639.042.729, which is financed by the Netherlands Organisation for Scientific Research (NWO). HA acknowledges the support of NWO via a Veni grant. FdG is supported by the VENI research program with project number 639.041.542, which is financed by the Netherlands Organisation for Scientific Research (NWO).

References

Bernardi G., et al., 2016, MNRAS, 456, 1259

Böhringer H., et al., 2010, A&A, 514, A32

Bonafede A., et al., 2014, MNRAS, 444, L44

Bonafede A., et al., 2017, MNRAS, 470, 3465

Botteon A., et al., 2018, MNRAS, 478, 885

Brienza M., et al., 2017, A&A, 606, A98

Brüggen M., et al., 2018, MNRAS, 477, 3461

Brunetti G., Jones T. W., 2014, International Journal of Modern Physics D, 23, 1430007

Brunetti G., Setti G., Feretti L., Giovannini G., 2001, MNRAS, 320, 365

Brunetti G., Venturi T., Dallacasa D., Cassano R., Dolag K., Giacintucci S., Setti G., 2007, ApJ, 670, L5

Brunetti G., et al., 2008, Nature, 455, 944

Carilli C. L., Taylor G. B., 2002, ARA&A, 40, 319

Cassano R., 2010, A&A, 517, A10

Cassano R., Brunetti G., 2005, MNRAS, 357, 1313

Cassano R., Brunetti G., Setti G., 2006, MNRAS, 369, 1577

Cassano R., Brunetti G., Setti G., Govoni F., Dolag K., 2007, MNRAS, 378, 1565

Cassano R., Ettori S., Giacintucci S., Brunetti G., Markevitch M., Venturi T., Gitti M., 2010, ApJ, 721, L82

Cassano R., Brunetti G., Norris R. P., Röttgering H. J. A., Johnston-Hollitt M., Trasatti M., 2012, A&A, 548, A100

Cassano R., et al., 2013, ApJ, 777, 141

Cassano R., Brunetti G., Giocoli C., Ettori S., 2016, A&A, 593, A81

Cornwell T. J., Golap K., Bhatnagar S., 2005, in Shopbell P., Britton M., Ebert R., eds, Astronomical Society of the Pacific Conference Series Vol. 347, Astronomical Data Analysis Software and Systems XIV. p. 86

Cuciti V., Cassano R., Brunetti G., Dallacasa D., Kale R., Ettori S., Venturi T., 2015, A&A, 580, A97

Cuciti V., Brunetti G., van Weeren R., Bonafede A., Dallacasa D., Cassano R., Venturi T., Kale R., 2018, A&A, 609, A61

Dallacasa D., et al., 2009, ApJ, 699, 1288

Donnert J., Dolag K., Brunetti G., Cassano R., 2013, MNRAS, 429, 3564

Eckert D., Molendi S., Paltani S., 2011, A&A, 526, A79

Feretti L., Giovannini G., Govoni F., Murgia M., 2012, A&ARv, 20, 54

Giacintucci S., Venturi T., Cassano R., Dallacasa D., Brunetti G., 2009, ApJ, 704, L54

Giovannini G., Feretti L., Girardi M., Govoni F., Murgia M., Vacca V., Bagchi J., 2011, A&A, 530, L5

Golovich N., et al., 2018, preprint, (`arXiv:1806.10619`)

Hales S. E. G., Riley J. M., Waldram E. M., Warner P. J., Baldwin J. E., 2007, MNRAS, 382, 1639

Intema H. T., Jagannathan P., Mooley K. P., Frail D. A., 2017, A&A, 598, A78

Kale R., Venturi T., Giacintucci S., Dallacasa D., Cassano R., Brunetti G., Macario G., Athreya R., 2013, A&A, 557, A99

Kale R., et al., 2015, A&A, 579, A92

Kravtsov A. V., Borgani S., 2012, ARA&A, 50, 353

Martinez Aviles G., et al., 2016, A&A, 595, A116

McMullin J. P., Waters B., Schiebel D., Young W., Golap K., 2007, in Shaw R. A., Hill F., Bell D. J., eds, Astronomical Society of the Pacific Conference Series Vol. 376, Astronomical Data Analysis Software and Systems XVI. p. 127

Miley G., 1980, ARA&A, 18, 165

Mohr J. J., Mathiesen B., Evrard A. E., 1999, ApJ, 517, 627

Molendi S., Pizzolato F., 2001, ApJ, 560, 194

Murgia M., Govoni F., Markevitch M., Feretti L., Giovannini G., Taylor G. B., Carretti E., 2009, A&A, 499, 679

Murgia M., Govoni F., Feretti L., Giovannini G., 2010, A&A, 509, A86

Offringa A. R., et al., 2014, MNRAS, 444, 606

Petrosian V., 2001, ApJ, 557, 560

Piffaretti R., Arnaud M., Pratt G. W., Pointecouteau E., Melin J.-B., 2011, A&A, 534, A109

Planck Collaboration et al., 2014, A&A, 571, A29

Reichert A., Böhringer H., Fassbender R., Mühlegger M., 2011, A&A, 535, A4

Santos J. S., Rosati P., Tozzi P., Böhringer H., Ettori S., Bignamini A., 2008, A&A, 483, 35

Savini F., et al., 2018, MNRAS, 474, 5023

Savini F., Bonafede A., Brüggen M., et al. 2019, The LOFAR Two-metre Sky Survey - II. First Data Release, Manuscript accepted for publication in A&A

Scaife A. M. M., Heald G. H., 2012, MNRAS, 423, L30

Sebastian B., Lal D. V., Pramesh Rao A., 2017, AJ, 154, 169

Shimwell T. W., et al., 2016a, MNRAS, 459, 277

Shimwell T. W., et al., 2016b, MNRAS, 459, 277

Shimwell T. W., et al., 2017, A&A, 598, A104

Shimwell T. W., Tasse C., Hardcastle M. J., et al. 2019, A LOFAR study of non-merging massive galaxy clusters, Manuscript accepted for publication in A&A

Srivastava S., Singal A. K., 2016, preprint, (`arXiv:1610.07783`)

Vallee J. P., Wilson A. S., 1976, Nature, 259, 451

Venturi T., Giacintucci S., Brunetti G., Cassano R., Bardelli S., Dallacasa D., Setti G., 2007, A&A, 463, 937

Venturi T., Giacintucci S., Dallacasa D., Cassano R., Brunetti G., Bardelli S., Setti G., 2008, A&A, 484, 327

Vikhlinin A., Markevitch M., Murray S. S., Jones C., Forman W., Van Speybroeck L., 2005, ApJ, 628, 655

Webber J. C., 1974, PASP, 86, 223

Wilber A., et al., 2018a, MNRAS, 473, 3536

Wilber A., et al., 2018b, MNRAS, 476, 3415

Williams W. L., et al., 2016, MNRAS, 460, 2385

Xue Y.-J., Wu X.-P., 2000, ApJ, 538, 65

de Gasperin F., et al., 2017, Science Advances, 3, e1701634 de Gasperin F., Dijkema T. J., Drabent A., et al. 2019, Systematic effects in LOFAR data: a unified LOFAR-LBA and LOFAR-HBA calibration strategy for calibrator fields, Manuscript accepted for publication in A&A

van Haarlem M. P., et al., 2013, A&A, 556, A2

van Weeren R. J., et al., 2016, ApJS, 223, 2

van Weeren R. J., et al., 2017, Nature Astronomy, 1, 0005

5 Other Works

In the papers listed below, where I was a co-author, I helped in reducing, analyzing, or imaging LOw FRequency ARray (LOFAR) radio data and I contributed to the interpretation of the results. In this chapter, the important results of some of these co-authored works are described and the implications of those results are discussed in a broader context.

- T. W. Shimwell, C. Tasse, M. J. Hardcastle, and et al. The LOFAR Two-metre Sky Survey - II. First Data Release. Manuscript to be published in A&A, 2019.
- A. Botteon, T. W. Shimwell, A. Bonafede, and et al. The cluster chain Abell 781 as observed with LOFAR and XMM-Newton. Manuscript to be published in A&A, 2019.
- F. Savini, A. Bonafede, M. Brüggen, and et al. A LOFAR study of non-merging massive galaxy clusters. Manuscript to be published in A&A, 2019.
- A. O. Clarke, A. M. M. Scaife, R. J. van Weeren, and et al. Signatures from a merging galaxy cluster its AGN population: LOFAR observations of Abell 1682. Manuscript to be published in A&A, 2019.
- A. Bonafede, M. Brüggen, D. Rafferty, I. Zhuravleva, C. J. Riseley, R. J. van Weeren, J. S. Farnes, F. Vazza, F. Savini, A. Wilber, A. Botteon, G. Brunetti, R. Cassano, C. Ferrari, F. de Gasperin, E. Orrú, R. F. Pizzo, H. J. A. Röttgering, and T. W. Shimwell. LOFAR discovery of radio emission in MACS J0717.5+3745. MNRAS, 478:2927–2938, August 2018.
- F. Savini, A. Bonafede, M. Brüggen, R. van Weeren, G. Brunetti, H. Intema, A. Botteon, T. Shimwell, A. Wilber, D. Rafferty, S. Giacintucci, R. Cassano, V. Cuciti, F. de Gasperin, H. Röttgering, M. Hoeft, and G. White. First evidence of diffuse ultra-steep-spectrum radio emission surrounding the cool core of a cluster. MNRAS, 478:2234–2242, August 2018.
- A. Botteon, T. W. Shimwell, A. Bonafede, D. Dallacasa, G. Brunetti, S. Mandal, R. J. van Weeren, M. Brüggen, R. Cassano, F. de Gasperin, D. N. Hoang, M. Hoeft, H. J. A. Röttgering, F. Savini, G. J. White, A. Wilber, and T. Venturi. LOFAR discovery

of a double radio halo system in Abell 1758 and radio/X-ray study of the cluster pair. MNRAS, 478:885–898, July 2018.

- M. Brüggen, D. Rafferty, A. Bonafede, R. J. van Weeren, T. Shimwell, H. Intema, H. Röttgering, G. Brunetti, G. Di Gennaro, F. Savini, A. Wilber, S. O'Sullivan, T. A. Ensslin, F. De Gasperin, and M. Hoeft. Discovery of large-scale diffuse radio emission in low-mass galaxy cluster Abell 1931. MNRAS, 477:3461–3468, July 2018.
- F. Savini, A. Bonafede, M. Brüggen, A. Wilber, J. J. Harwood, M. Murgia, T. Shimwell, D. Rafferty, A. Shulevski, M. Brienza, M. J. Hardcastle, R. Morganti, H. Röttgering, A. O. Clarke, F. de Gasperin, R. van Weeren, P. N. Best, A. Botteon, G. Brunetti, and R. Cassano. Studying the late evolution of a radio-loud AGN in a galaxy group with LOFAR. MNRAS, 474:5023–5035, March 2018.

5.1 Remnant Radio Galaxies

In Chapter 4, a study of the low-mass, merging galaxy cluster Abell 1314 is presented. LOFAR has provided the lowest frequency radio images of Abell 1314 that are available. In these images, it is apparent that there is irregular diffuse emission with low surface brightness near the cluster center. This diffuse emission has not been detected by any other observations at higher frequencies. Because of its shape, size, and location, Wilber et al. (2019) suggest that this diffuse emission represents a remnant radio galaxy. This emission is likely the old, fading, fossil emission of a previous cycle of activity of the bright cluster galaxy (BCG) IC 712, which resides at the cluster center. This BCG is active again, as revealed by its radio-bright core, but it has probably exhibited intermittent cycles of activity during the cluster lifetime. Since this cluster appears to be highly disturbed, with an X-ray brightness distribution elongated from East-to-West, it is possible but still unclear whether this remnant emission has been affected by turbulence within the ICM. Still, this remnant represents evidence of fossil electrons filling the central volume of the ICM. Since the cluster has such a low-mass, the turbulence induced by the merger is likely not powerful enough to create a full-scale radio halo. It is interesting to speculate whether this source and others like could be precursors to radio halos and radio relics.

With LOFAR observations at 140 MHz, Brüggen et al. (2018) also found diffuse emission at the center of the galaxy cluster Abell 1931 which is most likely related to a remnant radio galaxy. With proposed follow-up observations at 325 MHz from the Giant Metrewave Radio Telescope (GMRT) and archival data from the Very Large Array (VLA), the authors found

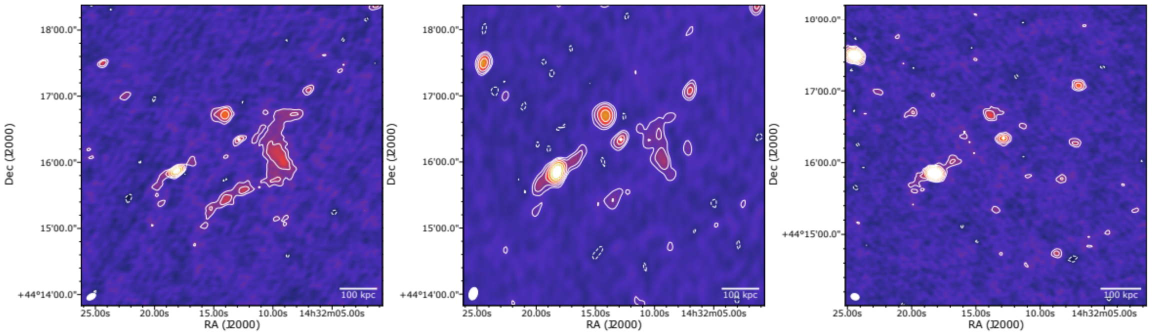

Figure 5.1: Abell 1931. Left: LOFAR HBA 120-168 MHz image. Contour levels are drawn at $[\pm3, 6, 12, 24] \times \sigma$ ($\sigma = 180\mu$Jy beam^{-1}) and the restoring beam of 5.0×8.7 arcsec is shown by the ellipse in the lower left corner. Middle: GMRT 325 MHz image. Contour levels are drawn at $[\pm3, 6, 12, 24] \times \sigma$ ($\sigma = 55\mu$Jy beam^{-1}); the restoring beam is 7.5×11.6 arcsec. Right: VLA 1-2 GHz B+C array image. Contour levels are drawn at $[\pm3, 6, 12, 24] \times \sigma$ ($\sigma = 18\mu$Jy beam^{-1}); the restoring beam is 5.2×7.0 arcsec. The cross marks the location of the BCG in Abell 1931. No emission from the extended LOFAR source is detected in the VLA image (Brüggen et al., 2018).

that this diffuse source has an ultra-steep spectrum ($\alpha = -2.86$) and is only detected at low frequencies. Other known remnant radio galaxies do not have such steep spectra. The suspected host is a BCG, and the activity likely ceased 200 Myr ago according to the distance of the remnant emission. To define the X-ray properties of the cluster, and determine whether the remnant emission has been shocked or re-accelerated, Brüggen et al. (2018) proposed a Chandra X-ray observation. From the X-ray luminosity and temperature, they suggested that the cluster has a low mass $< 3 \times 10^{14}$ M$_\odot$, which is consistent with the non-detection from the Planck satellite. Although the diffuse emission lies perpendicular to the presumed merger axis, its steep spectrum and low radio luminosity are uncharacteristic of gischt-type radio relics. Instead this emission is more similar to the candidate radio phoenix observed in Abell 2443. In Fig. 5.2 the power of the diffuse emission in Abell 1931 is compared to the powers of other phoenix-type relics from Nuza et al. (2017). The fossil emission in Abell 1931 has a lower power than all the phoenix-type relics in the sample; however, the X-ray luminosity of Abell 1931 is also lower than all the other clusters. This remnant is a particularly useful source for studying feedback processes and the late evolution of active galactic nuclei (AGN). If Abell 1931 is indeed a merging cluster, the absence of a gischt-type relic and radio halo may be related to the evolutionary phase or the overall energy budget of this system.

Similarly, Savini et al. (2018a) discovered extended, diffuse radio emission around an active BCG in the galaxy group MaxBCG J199.31832+51.72503 with LOFAR observations at 140 MHz. With follow-up GMRT observations at 610 MHz, the authors found that the extended emission exhibits a steep spectrum and that the core of the BCG also has a steep spectrum,

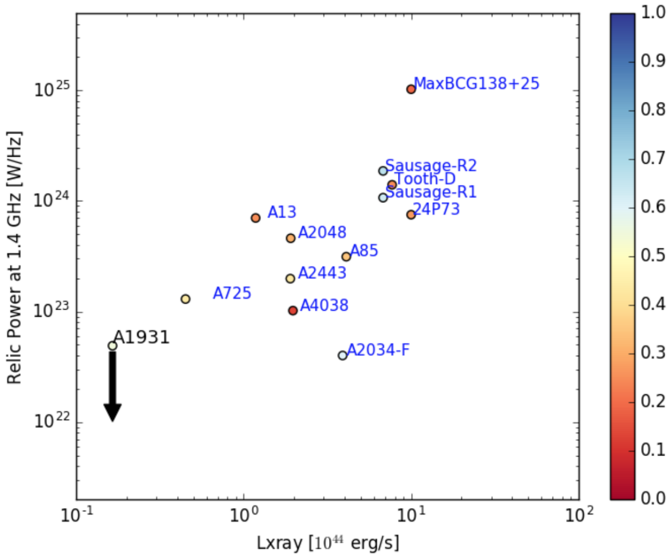

Figure 5.2: Radio power at 1.4 GHz of AGN/phoenix relics from Nuza et al. (2017) versus the X-ray luminosity of their host cluster in 10^44 erg s^{-1}. The colour of the points represents their largest linear scale in Mpc. The X-ray luminosity of the clusters 24P73 and MaxBCG 138+25 is not known (Brüggen et al., 2018).

indicating that the source is possibly evolved or at the end of its activity phase. The remnant emission extends up to 700 kpc into the group medium, therefore proving that BCGs can be particularly capable contributors of seed electrons. More discoveries of remnant sources at the centers of galaxy groups and galaxy clusters may reveal a clear connection between these sources and diffuse cluster sources, such as mini halos and giant halos. Furthermore, studying smaller systems such as galaxy groups and low-mass clusters, can help us to determine the origin and transport of cosmic-ray electrons in the context of cosmological structure growth.

All of these examples of detected fossil emission in galaxy clusters provide clear evidence for the theory of *AGN injection* whereby active radio galaxies supply the ICM with a population of mildly-relativistic seed electrons which are then re-accelerated to form radio halos or radio relics.

5.2 Complex Systems

By measuring the total density of baryonic matter in the Universe and comparing it to the density of luminous baryonic matter, it is apparent that up to 50% of the baryons in the

Universe remain undetected (Fukugita et al., 1998). It has been suggested that these baryons must reside within the filaments of the cosmic web which connect cluster nodes, the so-called warm-hot intergalactic medium (WHIM; Cen, 1999). The WHIM is difficult to observe because of its temperature range ($10^5 - 10^7$ K) and its moderate over-density of $(10 - 40)\,\rho_{\rm crit}$ (Davé et al., 2001). There have been various reports on the detection of the WHIM as part of the soft X-ray background and in emission and absorption lines in far ultraviolet and X-rays (e.g. Danforth & Shull, 2008; Tilton et al., 2012; Bonamente et al., 2017). It has been suggested that accretion shocks responsible for the formation of clusters may shock-heat and compress this intergalactic gas (Sunyaev & Zeldovich, 1972), making it potentially detectable via synchrotron emission.

Sensitive LOFAR observations may help us to detect faint filaments of radio emission which bridge groups and clusters together. Complex group networks are ideal targets for studying the evolution of cluster mergers and for potentially detecting the WHIM. Multiple component systems offer an opportunity to see the affects of complex merging geometries and how early or late diffuse radio sources begin to form within the ICM. Studying how the WHIM is related to the ICM is also important for understanding the transport and acceleration mechanisms of cosmic rays, and the nature of magnetic fields in the ICM (Vazza et al., 2017).

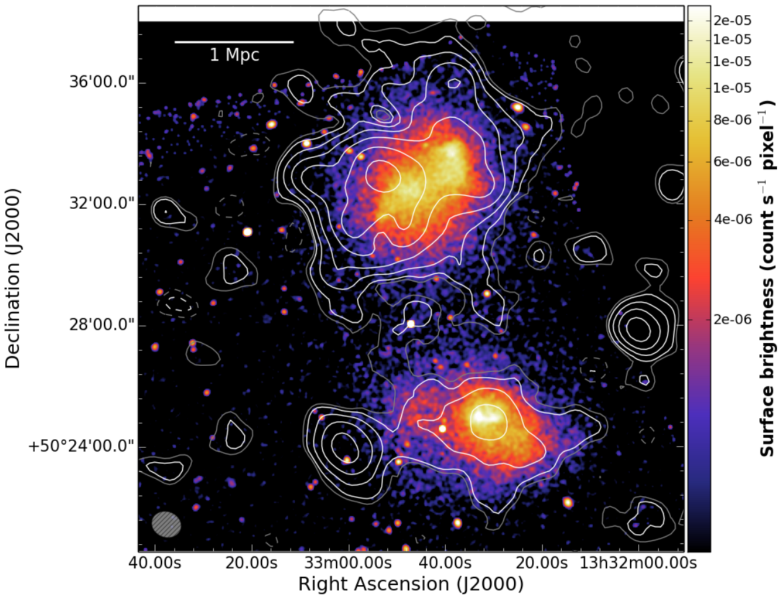

Figure 5.3: LOFAR radio contours with point sources subtracted of A1758 overlaid on the Chandra colour image of Fig. 2. The LOFAR white contours are spaced by a factor of 2 starting from 3σ, where $\sigma = 18\mu$Jy beam^{-1}. The negative, -3σ, contours are shown in dashed. Grey contours correspond to the $\pm 2\sigma$ level. The beam size is 60×51 arcsec and is shown in the bottom left corner (Botteon et al., 2018).

Botteon et al. (2018) discovered a double halo system in Abell 1758 where two clusters are merging in a N-S direction. The Northern halo was previously detected in the NVSS and WENSS surveys, and this was confirmed with GMRT and VLA observations. LOFAR recovers more halo emission in the North and also detects never-before-seen halo emission associated with A1758S. Two bright regions appear in the Northern halo, which may indicate areas that have been locally compressed or re-accelerated (such as in Shimwell et al., 2016 and de Gasperin et al., 2017). There is also a radio relic candidate, to the East of the Southern halo, but further data is needed to determine if there is a spectral index gradient towards the cluster centre, polarization of the emission, or a shock detection. Interestingly, there appears to be a bridge of radio emission connecting the two halos, hinting at an early interaction. This bridge of emission indicates that there are magnetic fields and cosmic-ray electrons outside of the intracluster media and that these two components are possibly facilitating cosmic ray transport. It is likely that a uniform magnetic field is also bridging these sub-clusters, and that perhaps this same field is amplified by turbulence near the ICM centers, leading to the brighter observed halo emission.

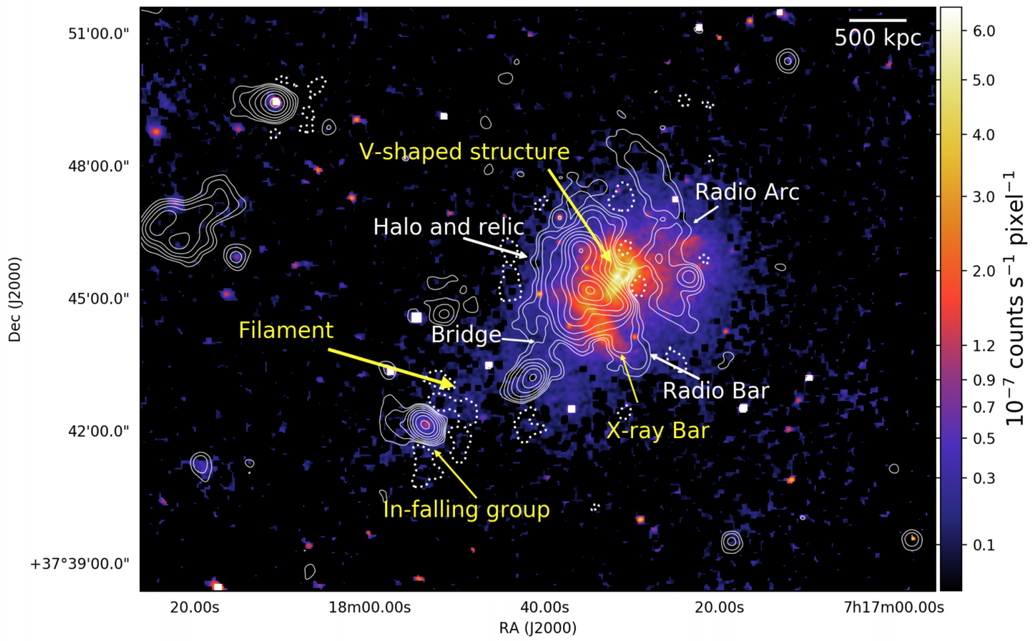

Figure 5.4: Color: X-ray emission from Chandra in the band 0.2 - 5 keV. Contours: radio emission from LOFAR at 147 MHz. The restoring beam is 19 arcsec × 18 arcsec and the rms noise (σ) is 160μJy beam^{-1}. Contours start at 4σ and are spaced by a factor 2. The contour at -4σ is dashed. The main components of the cluster emission in X-rays and radio are labelled in yellow and white, respectively. From Bonafede et al. (2018).

A joint X-ray-radio analysis of MACS J0717.5+3745 reveals a very complex system with four components. Bright X-ray features appear to have radio counterparts which are detected only at low frequencies (Bonafede et al., 2018). LOFAR observations reveal arc-shaped emission West of the known radio halo, emission coinciding with a bright X-ray bar, and additional emission Southeast of the halo bridging an infalling sub-group to the main group along an intergalactic filament. The halo emission is also more extended than in previous observations at higher frequencies. The spectral indices of the radio arc, radio bar, and radio bridge are steeper than $\alpha < -1.3$. Bonafede et al. (2018) suggest that the radio bridge is caused by the re-acceleration of electrons by shock waves that are injected along the filament during the cluster mass assembly. Here we see intergalactic structure in X-ray and radio that suggests the WHIM is detectable as it grows denser near cluster nodes of the cosmic web. This system reveals that complex systems can lead to diffuse emission that is not characteristic of radio relics and radio halos alone. As a result, future low-frequency observations of merging systems, like this one and others, may lead to a modernization for the taxonomy of cluster radio sources. It is also interesting to consider the connection between the thermal and non-thermal components of this system, outside of the intracluster media, which may indicate that hadronic collisions are playing a role in producing seed electrons that could then possibly be re-energized by accretion shocks.

References

Bonafede A., et al., 2018, MNRAS, 478, 2927

Bonamente M., Ahoranta J., Tilton E., Tempel E., Morandi A., 2017, MNRAS, 469, 3984

Botteon A., et al., 2018, MNRAS, 478, 885

Botteon A., Shimwell T. W., Bonafede A., et al. 2019, The cluster chain Abell 781 as observed with LOFAR and XMM-Newton, Manuscript accepted for publication in A&A

Brüggen M., et al., 2018, MNRAS, 477, 3461

Cen R., 1999, in Brumby S. P., ed., American Institute of Physics Conference Series Vol. 499, American Institute of Physics Conference Series. pp 58–67 (`arXiv:astro-ph/9908151`), doi:10.1063/1.1302220

Clarke A. O., Scaife A. M. M., van Weeren R. J., et al. 2019, Signatures from a merging galaxy cluster its AGN population: LOFAR observations of Abell 1682, Manuscript submitted for publication in A&A

Danforth C. W., Shull J. M., 2008, ApJ, 679, 194

Davé R., et al., 2001, ApJ, 552, 473

Fukugita M., Hogan C. J., Peebles P. J. E., 1998, ApJ, 503, 518

Nuza S. E., Gelszinnis J., Hoeft M., Yepes G., 2017, MNRAS, 470, 240

Savini F., et al., 2018a, MNRAS, 474, 5023

Savini F., et al., 2018b, MNRAS, 478, 2234

Savini F., Bonafede A., Brüggen M., et al. 2019, The LOFAR Two-metre Sky Survey - II. First Data Release, Manuscript accepted for publication in A&A

Shimwell T. W., et al., 2016, MNRAS, 459, 277

Shimwell T. W., Tasse C., Hardcastle M. J., et al. 2019, A LOFAR study of non-merging massive galaxy clusters, Manuscript accepted for publication in A&A

Sunyaev R. A., Zeldovich Y. B., 1972, A&A, 20, 189

Tilton E. M., Danforth C. W., Shull J. M., Ross T. L., 2012, ApJ, 759, 112

Vazza F., Brüggen M., Gheller C., Hackstein S., Wittor D., Hinz P. M., 2017, Classical and Quantum Gravity, 34, 234001

Wilber A., Brüggen M., Bonafede A., et al. 2019, Evolutionary phases of merging clusters as seen by LOFAR, Manuscript accepted for publication in A&A

de Gasperin F., et al., 2017, Science Advances

6 Conclusions

Cluster mergers are powerful drivers of turbulence and shocks, which can accelerate cosmic-ray electrons within the μG magnetic field of the intracluster medium (ICM) to generate Megaparsec (Mpc) sized radio structures. These diffuse cluster-scale sources, called radio halos and radio relics, have low surface brightness and exhibit a steep spectral index ($S \sim 1$ μJy arcsec^{-2} at 1.4 GHz and $\alpha < -1$; see Feretti et al., 2012 for a review), making them particularly difficult to detect. The LOw Frequency ARray (LOFAR; van Haarlem et al., 2013) offers unprecedented sensitivity for detecting the faintest, steepest-spectrum emission in distant galaxy clusters. This thesis demonstrates how LOFAR observations have been utilized to significantly contribute to the field on the origins of diffuse radio sources in merging clusters.

6.1 Motivation

The LOFAR Two-meter Sky Survey (LoTSS; Shimwell et al., 2017) offers us the unique opportunity to search for diffuse radio sources associated with galaxy clusters all across the Northern sky and up to high redshifts. Using the LOFAR instrument as a tool to probe the lowest-energy phenomena occurring in merging clusters, does our understanding of the physics of the ICM change? Referring to Sec. 1.5, I elaborate upon the motivation of this thesis:

1. **With sensitive, low-frequency observations do we find that radio halos and ultra-steep spectrum radio halos (USSRHs) are common in merging systems?** The turbulent re-acceleration model predicts that USSRHs should be more common, especially in lower-mass systems that experience more minor mergers (e.g. Cassano et al., 2006; Brunetti et al., 2008). Do we discover more USSRHs with LOFAR observations?

2. **Are radio relics the products of only the strongest merger shocks, or do minor-merger shocks also produce detectable radio relics?** Since most of the

known relics have been detected at higher frequencies, can LOFAR detect a population of smaller or fainter relics that are produced by more minor, or weaker, shocks? How well does the Mach number of a shock represent the particle acceleration efficiency from diffusive shock acceleration (DSA)?

3. **Is the emission from radio galaxies, bent-tails (BTs), and remnants susceptible to disturbance and re-acceleration by merger-induced turbulence and shocks in the ICM?** Do the same mechanisms that generate halos and relics affect the radio emission of active galactic nuclei (AGN) within the cluster environment? Does LOFAR detect more AGN phoenixes or gently re-energized tails (GReETs), where turbulence and shocks have led to re-brightening of faded lobe or tail emission?

4. **Do extended and remnant radio galaxies provide a large quantity of seed electrons for radio halos and relics?** With low-frequency observations, do we detect a larger quantity of remnant radio galaxies residing within the ICM? Do we also detect more extended emission from known AGN? Do these radio galaxies appear to be connected to any halos or relics?

5. **Can we determine the evolutionary phases of merging clusters based on radio observations?** If we probe the lowest-energy non-thermal activity of the ICM, can we relate the presence of diffuse radio sources directly to merging activity? Can the properties of these sources (i.e. how their brightness and spectral index change over their morphology) give us insight into the evolutionary status of a merging system? For example, are USSRHs mostly found in merging clusters that are in a progressed evolutionary stage? How soon after a merger are radio relics generated on the cluster outskirts?

6.2 Results

Here I summarize the important results from Chapters 2–5 by directly addressing the above motivational questions:

1. In Chapters 2 & 4, presenting the results of the papers Wilber et al. (2018a) and Wilber et al. (2019), respectively, we announced the discovery of two new radio halos found in the merging, massive clusters Abell 1132 and Z7215. Both of these clusters have nearly

the same mass as determined by the Sunyaev Zel'dovich (SZ) effect ($\sim 5.87 \times 10^{14} \mathrm{M}_{\odot}$ from Planck). In Fig. 6.1 the radio powers of the halos in Abell 1132 and Z7215 are compared to each other and to a sample of other halos, some of which were used to set the $P - M$ correlation from Cassano et al. (2013). The power of the halo in Abell 1132 is lower than that of the halo in Z7215, but both fall below the correlation and below the powers of the other halos in the sample. The halos in both clusters are also smaller than predicted by the $P - R_H$ correlation from Cassano et al. (2007) and exhibit a non-spherical morphology. The emission in Abell 1132 spans $\sim$ 650 kpc, while the halo in Z7215 is elongated with major axis twice as long as its minor axis.

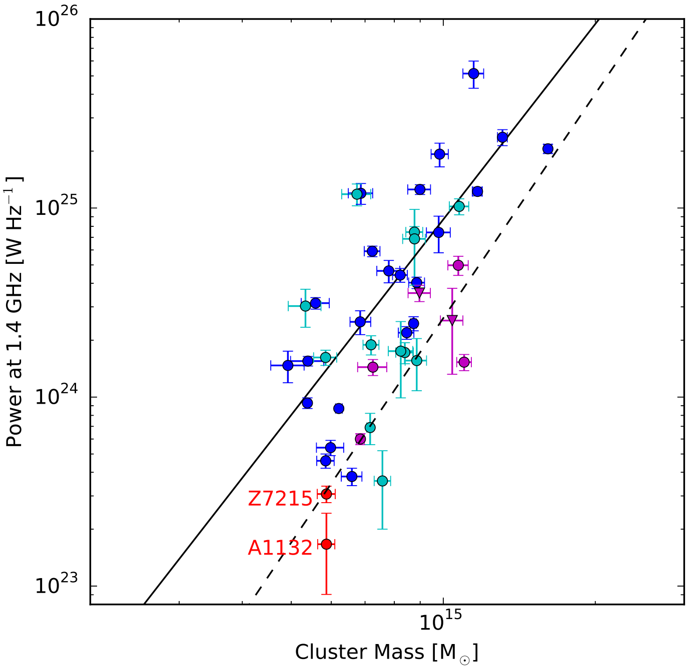

Figure 6.1: A sample of radio halos plotted by their radio power at 1.4 GHz versus their cluster mass (M_{500} – as determined from Planck observations). The sample of halos and their correlation is reproduced from Martinez Aviles et al. (2016). Halos with flux measured at 1.4 GHz are marked by blue circles and their derived fit is shown as a black line. Cyan circles represent halos with flux measured at frequencies other than 1.4 GHz. Magenta circles represent ultra-steep halos, and magenta triangles represent ultra-steep halos with flux measured at frequencies other than 1.4 GHz. The halos in Abell 1132 and Z7215 are marked by the red circles, and both fall below the correlation line as well as below all other halos in this sample. The dashed black line represents the best fit for all USSRHs and candidates.

The halo discovered in Abell 1132 is also a USSRH, with a spectral index of $\alpha = -1.75 \pm 0.19$ where $S \propto \nu^{\alpha}$. Wilber et al. (2019) re-processed 610 MHz GMRT data to determine an estimate of the spectral index for the halo in Z7215, but found that only an upper limit could be placed ($\alpha < -1.3$). Therefore, the halo in Z7215 is only a

USSRH candidate and further observations are necessary to approximate the spectral index of the halo emission. In Fig. 6.1, the best fitting correlation set at 1.4 GHz by Cassano et al. (2013) is given by a solid black line. If only USSRHs are considered, including Abell 1132 as a confirmed USSRH and Z7215 as a candidate, the best fit is given by the dashed black line. Cassano et al. (2006) showed that the expected number of radio halos to be detected at 150 MHz is a factor of 10 larger than the number expected at 1.4 GHz, and that most radio halos should have flux densities of a few mJy. Of the five merging clusters I have studied using LoTSS observations, two have clear confirmations for newly-detected radio halos with flux densities of 20.2 ± 2.0 mJy for the halo in Z7215 ($z \sim 0.30$) and 178 ± 27 mJy for the halo in Abell 1132 ($z \sim 0.14$) at 144 MHz. This pilot study provides an optimistic outlook for meeting the prediction that low-frequency observations will reveal ten times as many radio halos as were discovered at 1.4 GHz. Given that LoTSS will cover more than 1,000 massive clusters, it is not unlikely that we will discover > 100 new radio halos in the Northern sky. As more halos are detected at low-frequency, further statistical studies and re-assessment of correlations will be necessary. These discoveries will also help us to better understand the efficiency of turbulent re-acceleration and how radio halos are related to cluster dynamics and evolution.

2. Korngut et al. (2011) reported a detection of a shock in the massive cluster MACS J0744.9+3927 ($M_{500} = (11.8 \pm 2.8) \times 10^{14} M_{\odot}$) where a Bullet-type merger is presumed to have taken place. They found a decrement in SZ maps, indicating a shocked region approximately 200 kpc in length, and this was confirmed by coincident brightness and temperature discontinuities in X-ray observations of the cluster. The Mach number of the shock was estimated to be $\mathcal{M} = 1.0 - 2.9$. The shock sits near the cluster center, toward the West of the brightest central galaxy (BCG); however, as presented in Chapter 3, Wilber et al. (2018b) did not detect any radio emission coincident with the SZ-decrement. Only an upper limit on the radio emission could be placed, but this radio power limit was found to be much lower than the radio power of other relics. The detected shock is powerful enough to re-accelerate electrons, but there is no observed relic or re-brightening of AGN emission. Given the acceleration efficiency of a shock with this Mach number, we found that acceleration from the thermal pool would not produce detectable radio emission. But it is very peculiar that within the vicinity of a radio-loud AGN, there is still no re-brightening of fossil plasma. From our non-detection with sensitive low-frequency observations, we suggested that it may be too early to detect a relic generated by this shock since it sits close to the cluster center, and that a relic may form later as the shock travels outward. We also speculated that the shock in MACS J0744.9+3927 might not be caused by the merger, but instead caused by the AGN of the BCG, a so-called "AGN bubble". Nevertheless, with a Mach number comparable

to the Mach numbers of giant radio relics like the Toothbrush and Sausage relic, it is interesting that there is no observed synchrotron emission which would indicate that DSA is occurring at the shock front. Unless the Mach numbers inferred for other relics are completely off, this raises important questions. If the Mach number alone cannot determine the efficiency of shock acceleration, then what other factors play a role in the production of radio relics? Future investigations must address the role of magnetic fields at the shock front (e.g. Wittor et al., 2017), the geometry of the shocks (e.g. Golovich et al., 2018), or the existence of pre-existing CRe.

3. In Abell 1132 and in Abell 1314, giant head-tail radio galaxies are seen to be interacting with the intracluster medium. In both of these extended galaxies, we have observed disturbances in the emission. The giant radio galaxy (GRG) in Abell 1132 has a very collimated appearance up until about 1 Mpc. At this distance the emission in the tail appears to break and become diffuse. A re-brightened portion is seen at 1.3 Mpc, detached from the collimated jet emission. It is very possible that merger turbulence has disrupted the continuity of the tail emission after the radio galaxy traveled through the cluster. Since the emission at 1.3 Mpc is still glowing, it is also highly likely that it has been re-accelerated or gently re-energized. A similar phenomenon is seen in IC 711, where we have confirmed a flattening of the spectral index in the middle portion of the tail. Again, this indicates some form of re-acceleration or gentle re-energization. The region of flattening is also coincident with a substructure of the ICM, possibly alluding to compression along the merging axis. The emission toward the very end of IC 711's tail appears to be sweeping Westward, and high-resolution LOFAR maps from Wilber et al. (2019) show filaments of emission as well. Although a spectral index could not be determined in this region – since the emission was not detected at higher frequencies – we suggested that it has been disturbed by merger mechanisms, possibly a shock, because the trajectory of the host galaxy cannot explain its morphology. These results show plausible evidence that merger-induced turbulence and shocks can affect AGN emission, especially in extended radio galaxies with emission that spans the inner cluster volume.

4. We have discovered more extended emission associated with the known radio galaxies in both Abell 1132 and Abell 1314. In previous observations at higher frequencies, the head-tail radio galaxies in these two clusters were only partially detected. LOFAR observations at 144 MHz have revealed more extended and diffuse tail emission. The HT in Abell 1132 extends more than 1 Mpc through the Southern region of the cluster. The HT in Abell 1314 extends up to 800 kpc in the Western region of its cluster. The discovery of this extended emission may have a large impact on the luminosity function

of AGN at low frequencies. Remnant, fossil emission is also seen at the center of Abell 1314, which has only been detected by LOFAR and not at any higher frequencies. Abell 1314 is a unique example because although fossil emission can be seen at the cluster center, a full size radio halo has not been generated likely because the cluster is of very low-mass and the merger-induced turbulence is not efficient enough to produce one. As discussed in Chapter 5, LOFAR observations have revealed an abundant amount of low-energy fossil plasma residing throughout the ICM of several clusters (Wilber et al., 2019; Savini et al., 2018; Brüggen et al., 2018). This fossil emission was once produced by cluster AGN, but now exists as a reservoir of mildly-relativistic electrons for halo and relic generation. Indeed, the diffuse and extended emission in the tail of the GRG in Abell 1132 appears to be connected to the diffuse emission of the central halo. The HT in Abell 1314 is also supplying the cluster outskirts with fossil plasma, some of which may have already been shocked and re-brightened. These results lend further support to the hypothesis that radio AGN can supply the ICM with a sufficient population of mildly-relativistic electrons that may be the seed source powering halos and relics.

5. In Chapter 4, presenting Wilber et al. (2019), we carried out a trial study to hypothesize the evolutionary phases of three separate merging clusters based on LOFAR observations. This study targeted clusters of lower-mass to determine if diffuse radio emission was detectable in the ICM. Only one of the three clusters showed merger-related diffuse emission. We suggested that Abell 1314 was of such a low mass that the energy budget in the merger would not be sufficient enough to generate a cluster-wide radio halo, even though the cluster ICM appears to be highly disturbed in X-ray observations. We discovered that Abell 1319 consists of three separate ICM components that appear to be in a pre-merging state. We did not detect any radio halos or radio relics associated with this system, although it is possible that the gravitational infall of these components could already be generating turbulence or shocks in the system. We claim that the cluster Z7215 is in a post-merging phase, but as I addressed in Question 1. it is interesting that the power of the halo detected in Z7215 is brighter and the spectral index possibly flatter than that of the halo in Abell 1132, which has the same cluster mass. While it is still likely that Z7215 is in a post-merging phase, Abell 1132 might be even further evolved. This would provide evidence that USSRHs may be a transient phenomena, occurring at very late evolutionary stages of mergers. It is also interesting to consider the evolutionary stage of the Bullet-type merger of MACS J0744.9+3927. Since the shock has not yet traveled to the cluster outskirts, it may be the case that this a merger in its early stage.

6.3 Unanswered Questions

Relating large samples of radio halos to their cluster mass and their cluster X-ray luminosity has been mainly done at higher frequencies. The halos we have discovered in Abell 1132 and Z7215 do not fit the correlation set at 1.4 GHz. We still do not know if these fainter, smaller halos are outliers from the bulk, or if they imply a new trend. Measuring the powers of known as well as new radio halos at lower-frequencies may change current correlations. Lower-frequency observations may also reveal a larger population of halos connected to lower-mass systems and minor-merger events. For the two halos we have discovered with LoTSS, the clusters have the same mass, but the halos have different powers. Could this be linked to the age of the merger event? Both are post-merger, but perhaps the Abell 1132 merger is further evolved and the halo has suffered further energy loss compared to the one in Z7215. This poses further questions regarding the transient properties of radio halos (see e.g. Donnert et al., 2013). As we detect more USSRHs, we may also be able to more accurately relate their spectra to the evolutionary phase of the cluster. Alternatively, we may find that they are mostly found in systems with less turbulent energy or in lower-mass systems. To answer these questions the next step is to use low-frequency observations to do statistical studies on a large sample of low-mass clusters.

The HT radio galaxies in Abell 1132 and 1314 both show signs of disturbance, but it is still unknown whether this is caused by merger-induced turbulence, or if it is simply caused by the turbulent motions from the activity of the AGN. We were not able to confirm a shock at the location of Westward-sweeping filamentary emission in the tail of IC 711. Ironically, where we do have a confirmed shock, in MACS J0744.9+3927, there is no re-brightening of fossil emission even though it exists near a radio-loud AGN. An important unanswered question is how bright radio relics can exist so far from the cluster center, where there should be fewer seed electrons and weaker magnetic fields. It seems contradictory that a shock would not generate a relic closer to the cluster center, where there are presumably more seed electrons and stronger magnetic fields. Of all the five merging clusters I have studied, two of which might be considered as matured mergers, I did not detect any sources characteristic of radio relics. This implies that the connection between radio relics, cluster mass, and merger evolution must be further studied.

Sensitive low-frequency observations also give us the chance to detect intergalactic filaments as part of the warm-hot intergalactic medium (WHIM). Discovering radio sources associated with the WHIM may help us to explain the origin of ICM magnetic fields and the transport of cosmic-rays between clusters and galaxy groups. It also tells us about the shock acceleration efficiencies at higher Mach numbers since the accretion shocks around filaments have $M > 10$.

We might find more radio arcs, radio bridges, and radio filaments in between clusters, such as those discussed in Chapter 5. If so, it will prompt us to redefine and re-analyze our current taxonomies for cluster sources and perhaps warrant new theories and simulations on cosmic structure growth.

6.4 The Future of Surveys

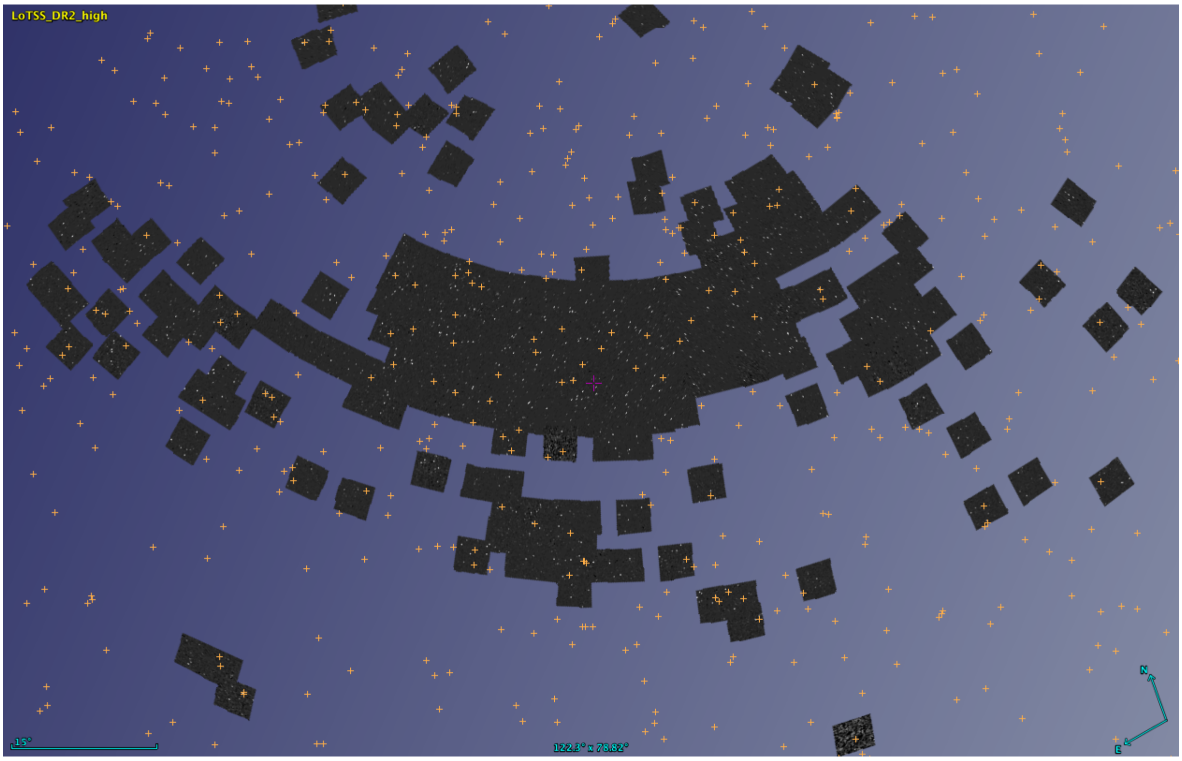

Figure 6.2: Using Aladin, we can check the progress of LoTSS and see radio sources in high-resolution. Clusters from the Planck catalogue are represented by yellow crosses. Once the survey is complete, it is likely that we will discover hundreds of new diffuse radio sources.

The first data release of LoTSS marked a groundbreaking accomplishment in radio survey science at low frequencies (Shimwell et al., 2019). Rapid and significant improvements in calibration and imaging algorithms have led to a second data release where survey images reach a resolution of ~ 5 arcsec and depth of 100 μJy beam^{-1} (see https://lofar-surveys.org and Tasse et al., 2018). In Fig. 6.2, LoTSS images have been mosaicked together over a large portion of the sky, and hundreds of thousands of sources are visible. In Fig. 6.3, we zoom into a portion of this sky, containing the cluster Abell 1703. In this small region we can see many different radio sources: the centrally located remnant in the galaxy group MaxBCG J199.31832+51.72503 (Savini et al., 2018), possible radio halo emission in Abell 1703, and large-scale, faint emission in the North, likely associated with a remnant radio galaxy. These sources will be further studied in a forthcoming paper.

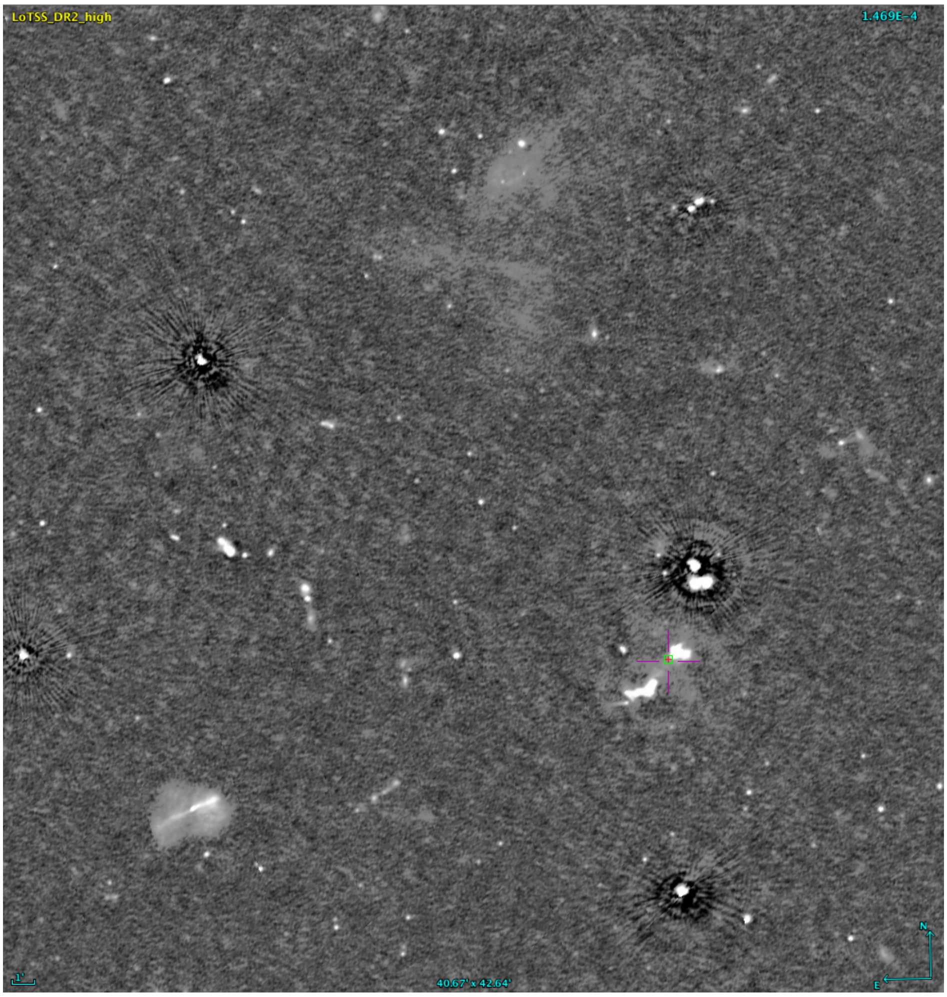

Figure 6.3: Zooming in on a region in LoTSS we see many interesting radio sources. Abell 1703 is marked by a magenta cross.

The LoTSS survey is only about 25% complete as of October 2018. As the coverage of LoTSS expands, large statistical studies on galaxy clusters will be possible. Selecting clusters based on their mass and dynamics, and comparing the types of detected radio sources found in these clusters will help us to better understand the physics and effects of cluster formation and evolution. Surely there will also be new, unclassified sources to discover. Radio surveys of galaxy clusters at low-frequencies may call for an updated taxonomy for diffuse radio emission.

As further LoTSS pointings are observed, processed, and imaged, radio astronomers will face the increasing challenge of data abundance. Millions of sources have already been detected by LoTSS, and after the initial problem of automating calibration and imaging, the more significant problem will be how to automatically detect and classify the radio sources in the survey images. Machine learning is already being used to investigate methods for automated radio galaxy classification (e.g. Lukic et al., 2018; Alger et al., 2018).

References

Alger M. J., et al., 2018, MNRAS, 478, 5547

Brüggen M., et al., 2018, MNRAS, 477, 3461

Brunetti G., et al., 2008, Nature, 455, 944

Cassano R., Brunetti G., Setti G., 2006, MNRAS, 369, 1577

Cassano R., Brunetti G., Setti G., Govoni F., Dolag K., 2007, MNRAS, 378, 1565

Cassano R., et al., 2013, ApJ, 777, 141

Donnert J., Dolag K., Brunetti G., Cassano R., 2013, MNRAS, 429, 3564

Feretti L., Giovannini G., Govoni F., Murgia M., 2012, The Astronomy and Astrophysics Review, 20, 1

Golovich N., et al., 2018, preprint, (`arXiv:1806.10619`)

Korngut P. M., et al., 2011, ApJ, 734, 10

Lukic V., Brüggen M., Banfield J. K., Wong O. I., Rudnick L., Norris R. P., Simmons B., 2018, MNRAS, 476, 246

Martinez Aviles G., et al., 2016, A&A, 595, A116

Savini F., et al., 2018, MNRAS, 474, 5023

Shimwell T. W., et al., 2017, A&A, 598, A104

Shimwell T. W., Tasse C., Hardcastle M. J., et al. 2019, A LOFAR study of non-merging massive galaxy clusters, Manuscript accepted for publication in A&A

Tasse C., et al., 2018, A&A, 611, A87

Wilber A., et al., 2018a, MNRAS, 473, 3536

Wilber A., et al., 2018b, MNRAS, 476, 3415

Wilber A., Brüggen M., Bonafede A., et al. 2019, Evolutionary phases of merging clusters as seen by LOFAR, Manuscript accepted for publication in A&A

Wittor D., Vazza F., Brüggen M., 2017, MNRAS, 464, 4448

van Haarlem M. P., et al., 2013, A&A, 556, A2

A Appendix

A.1 Radiative Processes

Before diving into astrophysical phenomena, it is important to discuss the basic physical interactions of the particles which produce photons of various wavelengths (energies). Once we have an understanding of these particle and field interactions we can then assume specifics about the astrophysical environments producing the photons in question. In all honesty, these interactions are best described and understood using quantum electrodynamics, but the processes relevant to the work of this thesis can be approximated with a more classical approach.

There are two types of radiation, thermal and non-thermal. Thermal radiation is emitted based on the temperature of the emitting body. Blackbody radiation follows a Planck distribution. A type of thermal radiation is Bremsstrahlung, briefly explained in the next section. Non-thermal radiation involves interactions between cosmic rays and magnetic fields.

A.1.1 Bremsstrahlung Radiation

Bremsstrahlung radiation or “Braking” radiation occurs predominately when a free electron is deflected by an ion. This kind of radiation happens in the medium of a hot, ionized plasma. Since the electron is much less massive than an ion, it accelerates, or receives a deflection in its path, from the ion. For a population of emitting electrons, the total emissivity goes as $\epsilon_{\rm eff} \propto n_e \, n_{\rm ion} \, T^{1/2}$, where n_e and $n_{\rm ion}$ are the electron and ion number densities, respectively, and T is the temperature of the plasma. Bremsstrahlung produces X-ray photons in the very hot plasma of the intracluster medium. Galaxy clusters are the most luminous X-ray sources in the Universe with luminosities of $L_X \sim 10^{44}$ erg s^{-1}. X-ray observations from satellites such as the Chandra X-ray observatory and XMM-Newton can be used to measure the temperature and mass of clusters.

A.1.2 Synchrotron Radiation

Synchrotron radiation, or synchrotron emission, is a form of non-thermal cosmic-ray radiation, and occurs when a relativistic electron is accelerated by a magnetic field[1]. A single electron with a Lorentz factor $\gamma = (1 - \frac{v^2}{c^2})^{-1/2}$ is accelerated perpendicular to its velocity, v, by a magnetic field, B, inducing helical motion at a constant velocity along the direction of a magnetic field line. During this circular motion, photons with energy dependent on γ, B, and θ, the angle of pitch between the vectors $\vec{v}$ and $\vec{B}$, are emitted. For example, a given photon with energy of 100 MHz (in the low-frequency radio regime), can be produced by an electron with a Lorentz factor of $\gamma = 5000$ accelerated by a magnetic field with strength $B = 1\mu G$ (Govoni & Feretti, 2004). The photons are emitted as a beam in the shape of a narrow cone following the helical trajectory of the electron (see Fig. A.1). This produces a lighthouse effect for the observer who will receive pulses of light.

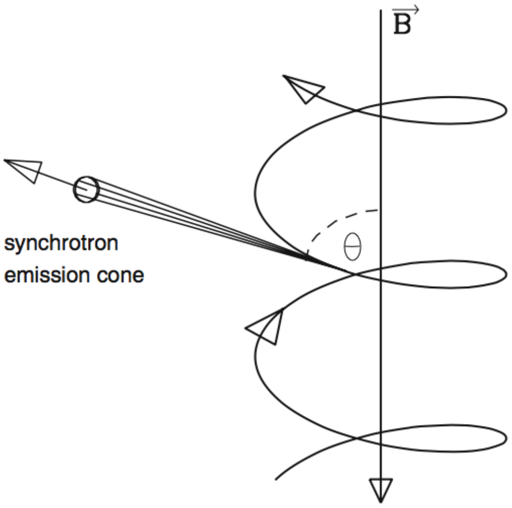

Figure A.1: The emitted cone of light from a spiralling electron in a magnetic field, adapted from Beckmann & Shrader (2013).

The frequency of the pulses observed is dependent on the Larmor frequency $\omega = \frac{eB}{\gamma mc}$ which describes the angular frequency, or gyrofrequency, of electron's circular motion. For highly relativistic electrons, $\gamma \gg 1$, the gyrofrequency increases and the emitted light is beamed so that an observer within line of sight will see a spectrum as illustrated in Fig. A.2 where the y-axis represents the total power emitted and the x-axis represents the photon freqeuncy (Beckmann & Shrader, 2013). The spectrum in Fig. A.2 shows that a peak of power output is reached at a single frequency $\nu = 0.29\nu_c$, where ν_c is the critical frequency $\nu_c = \frac{3}{4\pi}\gamma^3\omega sin(\theta)$ (Rybicki & Lightman, 1979).

---

[1] Relativistic protons can be accelerated by magnetic fields and emit via synchrotron too, but since the emitted power is proportional to m^{-2} the emission from protons, or ions, is often negligible.

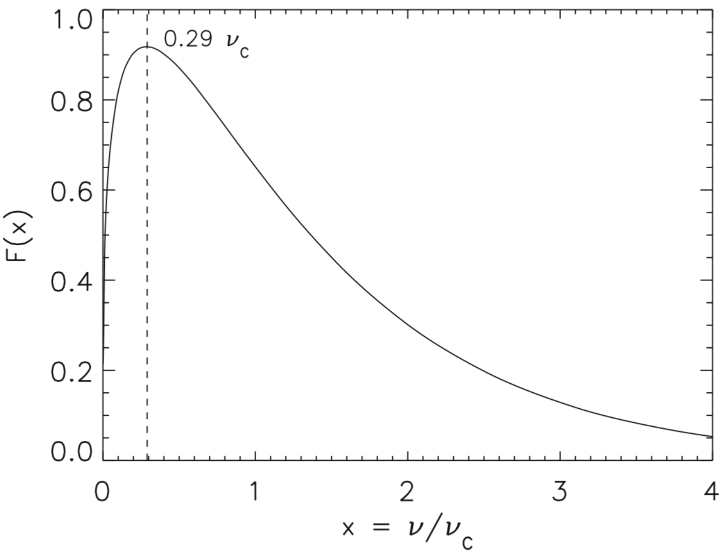

Figure A.2: The spectrum of a single electron, peaking at 0.29 the critical frequency, where $F(x)$ is the total emitted power and x is a function of frequency of the emitted photons (Beckmann & Shrader, 2013).

A population of relativistic electrons in a plasma medium then produce a spectra which is a sum of all the individual spectra from all electrons emitting in line of sight. A large population of electrons emitting over a large region are likely to vary in Lorentz factor, pitch angle, and reside in magnetic fields of varying strength, so the spectra of a radio source ranges in frequency and is directly correlated to the electron energy distribution (Rybicki & Lightman, 1979). The fall off of the intensity at higher frequency has to do with the shorter lifetimes of electrons emitting photons at higher energies (e.g. Carilli & Barthel, 1996). Then the spectral index α (the slope of the spectrum as approximated by a power-law where $S \propto \nu^{-\alpha}$) can indicate the age of the emission. A flatter spectrum indicates electrons emitting with higher energy, and a steep spectrum means older emission because the higher energy emission suffers energy loss more quickly. The lifetime of the emitting electron is proportional to the energy divided by the rate of energy loss by Inverse Compton, which goes as E^2. Therefore, the synchrotron lifetime, or synchrotron loss, goes as $1/E$. See Sec. 1.3.1.2 for a derivation of the synchrotron spectrum.

A.1.3 Inverse Compton Scattering

In a plasma containing electrons and photons, a low-energy electron can receive energy and be excited from a high-energy photon. This is called Compton scattering. Inversely, a photon can be up-scattered to a higher energy when it encounters and higher-energy electron, called

Inverse Compton scattering. The frequency of the scattered wave ν_{out} is related to that of the incident wave ν_{in} as:

$$\nu_{\text{out}} = \frac{4}{3}\gamma^2 \nu_{\text{in}}.$$

Inverse Compton scattering can occur to low-energy photons that pass through gas clouds filled with "hot" electrons, and therefore, the emissivity then only depends on the number density of electrons, not ions, so $\epsilon_{\text{eff}} \propto n_e$.

The Cosmic Microwave Background exists throughout all the cosmos as an echo of the Big Bang, representing the first radiation to escape after the Universe transitioned from opaque to transparent at the epcoh of recombination and photon decoupling. The expansion of space over the last 14 billion years has caused the wavelength of these photons to increase, and their energy to decrease. They are now radiating at microwave frequencies, corresponding to a temperature $T_{\text{CMB}} \approx 2.725$ K. CMB photons exist everywhere (there are about 400 per cm^3 of space), and we can measure the CMB blackbody spectrum with satellites such as Planck. CMB photons suffer Inverse Compton scattering in the region of the hot plasma of the intracluster medium (ICM).

The Sunyaev-Zel'dovich (SZ) effect occurs when the blackbody spectrum of the Cosmic Microwave Background (CMB) is changed due to the presence of a hot plasma (such as the ICM), causing a perceived change in brightness in the CMB radiation at that location. This appears as a decrement below ~ 220 GHz, and as an increment above this radio frequency. The SZ effect is valuable for measuring properties of galaxy clusters. The mass and merging status of a galaxy cluster can be inferred from this thermal SZ effect. The Planck satellite has already detected over 3,000 clusters via the SZ effect (Planck Collaboration et al., 2014, 2016).

Cosmological dimming affects all sources and goes as (Tolman, 1934)

$$S_o = \frac{S_i}{(z+1)^4} \tag{A.1}$$

where S_o is the observed brightness, S_i is the intrinsic brightness, and z is the redshift of the source. However, the Sunyaev-Zel'dovich effect from a cluster is independent of redshift and does not suffer this $(1+z)^{-4}$ dimming. This is because the effect is a fractional change in the brightness of the CMB and the CMB's energy density increases as $(1+z)^4$, cancelling out the comological fading, so even the highest redshift clusters can be detected via the SZ effect. This effect is also proportional to the line-of-sight integral of the plasma pressure and therefore, shocks in the intracluster medium can appear as substructures in the SZ signal of a cluster.

References

Beckmann V., Shrader C., 2013, Active Galactic Nuclei. John Wiley & Sons

Carilli C., Barthel P., 1996, The Astronomy and Astrophysics Review, 7, 1

Govoni F., Feretti L., 2004, International Journal of Modern Physics D, 13, 1549

Planck Collaboration et al., 2014, A&A, 571, A29

Planck Collaboration et al., 2016, A&A, 594, A13

Rybicki G. B., Lightman A. P., 1979, Radiative processes in astrophysics

Tolman R. C., 1934, Relativity, Thermodynamics, and Cosmology

Acknowledgements

I want to express my deepest gratitude to Marcus, my Doktorvater, without whom none of this would have been possible. Thank you, Marcus, for giving me this opportunity, for inviting me to do research with you in Germany, for believing in me, and for fighting for me. You have always been there for me, and your encouragement has always pushed me in the right direction, even at the most difficult of times. You have instilled a great passion in me, which has led to my desire to continue in this field. I cannot thank you enough for your unparalleled mentorship in these last three years. I could not have asked for a better PhD advisor.

Annalisa, I owe much of my gratitude to you, too. You were there from the very beginning and patiently suffered my technical clumsiness with your unwavering grace. Thank you for teaching me, listening to me, and taking your time to help me blossom into an independent researcher. You have been a personal role model and I will continue to be inspired by you in the years to come.

Federica, detective Rust, Italian beauty, foosh, best friend, I love you. Thank you for E-V-E-R-Y-T-H-I-N-G. There is no way I could have done this without you. You have been by my side through it all, and I needed you every bit of the way. Thank you for being an a-mazing friend, and for loving me, and for helping me to grow. From the mountain peaks in Bavaria to the beach of the Adriatic sea, from the windy Dutch coast to the cozy kitchen of Zur Schanze, our memories are unforgettable. I am so proud of you. We did it!

To all my co-authors, co-researchers, co-workers, I thank you for your insights, your efforts, your guidance, explanations, patience, and kindness. You are the reason I love the LOFAR group and the reason I want to stay involved in the LOFAR collaboration.

Kery, you have been a phenomenal friend to me – we really know how to have fun. Thank you for keeping me wild. I love you. Thank you, Jean, for our beautiful adventures, for your emotional support and guidance, and for your sincere love – it made all the difference. Thank you to Nina for helping me repair my relationship with myself. Thank you to my Italian

family for feeding me and teaching me how to cook the most delicious food I have ever tasted. Thank you Paola, Enza, Giovanni, Francesco, Alex, and all the beautiful people I encountered in this journey.

To my family back home, I love you all so much, and I have missed you greatly during the time we have been apart in the last three years. Thank you, Mom, for giving me a warm home to return to, filled with peace and love, and my favorite doggos. To my sisters, Rigel and Zuria, I love you with all my heart. Zuria, little foosh, thank you for being my best friend and a fire meme dealer. I am so glad I got to share Hamburg with you. To my niece Aislinn, and my unborn niece, I love you both. Thank you, Dad, for opening my eyes and my heart to the wonders of our Universe. Thank you for inspiring me and thank you for telling me how much you love me and how proud you are of me every time we speak. I would not be the person (or scientist) I am without your influence. You have always been my world.

To Jefe, you have supported me through it all with nothing but absolute compassion and love. You have helped me to grow and to discover and to live to the fullest. I am so lucky to have you. You truly are the man of the century and I love you with all my heart.